Plasmonic Surface Modifications with Hard-Core/Soft-Shell Nanoparticles

---

DISSERTATION

zur Erlangung des akademischen Grades eines Doktors der Naturwissenschaften (Dr. rer. nat.) an der Bayreuther Graduiertenschule für Mathematik und Naturwissenschaften der Universität Bayreuth

Vorgelegt von

Mareen Beata Müller

geboren in Löbau

Bayreuth, 2015

Die vorliegende Abreit wurde in der Zeit von November 2011 bis April 2015 am Lehrstuhl für Physikalische Chemie II unter der Betreuung von Herrn Prof. Dr. Andreas Fery an der Universität Bayreuth angefertigt.

Vollständiger Abdruck der von der Bayreuther Graduiertenschule für Mathematik und Naturwissenschaften (BayNAT) der Universität Bayreuth genehmigten Dissertation zur Erlangung des akademischen Grades eines Doktors der Naturwissenschaften (Dr. rer. nat.).

Dissertation eingereicht am: 15.04.2015

Zulassung durch das Leitungsgremium: 28.04.2015

Wissenschaftliches Kolloquium: 21.09.2015

Amtierender Direktor: Prof. Dr. Franz X. Schmid

Prüfungsausschuss:

Prof. Dr. Andreas Fery	(Erstgutachter)
JProf. Dr. Markus Retsch	(Zweitgutachter)
Prof. Fr. Rhett Kempe	(Vorsitz)
Prof. Dr. Mukundan Thelakkat	

Meiner Familie und Samuel

"*Und bist du nicht willig, so brauch ich Geduld*"

Peter Kruse, dt. Psychologe

CONTENTS

LIST OF PUBLICATION

1. **Müller, M. B.**; Karg, M.; Fortini, A.; Hellweg, T.; Fery, A. Wrinkle-assisted linear assembly of hard-core/soft-shell particles: impact of the soft shell on the local structure. *Nanoscale* **2012**, 4, 2491-2499

2. **Müller, M. B.**; Tebbe, M.; Andreeva, D. V.; Karg, M.; Alvarez Puebla, R. A.; Pazos Perez, N.; Fery, A. Large-Area Organization of PNIPAM-Coated Nanostars as SERS Platforms for Polycyclic Aromatic Hydrocarbons Sensing in Gas Phase. *Langmuir* **2012**, 28, 9168-9173

3. Hanske, C.; **Müller, M. B.**; Bieber, V.; Tebbe, M.; Jessl, S.; Wittemann, A.; Fery, A. The Role of Substrate Wettability in Nanoparticle Transfer from Wrinkled Elastomers: Fundamentals and Application toward Hierarchical Patterning. *Langmuir* **2012**, 28, 16745-16750

4. **Müller, M. B.**; Kuttner, C.; König, T. A. F.; Tsukruk, V. V.; Förster, S.; Karg, M.; Fery, A. Plasmonic Library Based on Substrate-Supported Gradiential Plasmonic Arrays. *Acs Nano* **2014**, 8, 9410-9421

5. Tebbe M.; Mayer M.; Glatz B. A.; Hanske C.; Probst P. T.; **Müller M. B.**; Karg M.; Chanana M.; König T. A. F.; Kuttner C. and Fery A., Optically Anisotropic Substrates via Wrinkle-Assisted Convective Assembly of Gold Nanorods on Macroscopic Areas. *Faraday Discussions* **2014**

LIST OF ABBREVIATIONS AND SYMBOLS

A	amplitude
α	polarizability
α_R	Raman polarizability
AFM	atomic force microscopy
BA	butenylamine
BIS	*N*-methylenebisacrylamide
BT	benzenethiol
CA	confinement assembly
CTAB	cetyltrimethylammonium bromide
DF	dark field
D_h	hydrodynamic radius
DLS	dynamic light scattering
DMF	*N*,*N*-dimethylformamide
E	elastic modulus
ε	strain
$\boldsymbol{E}_0$	external electric field
ε_c	critical strain
EF	Raman enhancement factor
$\boldsymbol{E}_{near}$	electric near field
ϵ_0	dielectric constant of the vacuum
ϵ_d	dielectric constant of the medium
ϵ_m	dielectric constant of the metal
γ	electron collision frequency in the crystal lattice
h	height
ITO	indium tin oxide
k	wave vector

λ	wavelength
LCST	lower critical solution temperature
λ_{max}	wavelength of the LSPR position
LSPR	localized surface plasmon resonance
$LSPR_{max}$	maximum of the LSPR position
μCP	micro contact printing
MC	Monte Carlo simulation
MPS	methacryloxypropyltrimethoxysilane
n	refractive index
$\bar{n}$	average refractive index
NIPAM	*N*-isopropylacrylamide
NP	nanoparticle
NS	nanostars
ν	Poisson ratio
ω	frequency
ω_{em}	emitted frequency
ω_{inc}	incoming frequency
OMeTAD	N2,N2,N2′,N2′,N7,N7,N7′,N7′-octakis(4-methoxyphenyl)-9,9′-spirobi[9H-fluorene]-2,2′,7,7′-tetramine
ω_p	plasma frequency
p	dipole moment
PAA	poly(acrylic acid)
PDMS	poly(dimethylesiloxane)
π	number Pi
PMMA	poly(methyl methacrylate)
PNIPAM	poly(*N*-isopropylacrylamide)
PS	polystyrene
PVP	poly(vinylpyrrolidone)
r	radius

rcf	relative centrifugation force
rpm	rounds per minute
SA	self-assembly
σ_{abs}	absorbtion cross section
SEM	scanning electron microscopy
SERS	surface enhanced Raman spectroscopy
σ_{ext}	extinction cross section
SL	soft lithography
SR	spin-release
σ_{sact}	scattering cross section
TASA	template assisted self-assembly
TEM	transmission electron spectroscopy
US	ultra sound
UV-Vis	ultra-violet visible spectroscopy
v_{radi}	centrifugal spin velocity
v_{spin}	rotational spin velocity
VPT	volume phase transition
VPTT	volume phase transition temperatur
WAA	wrinkle-assisted assembly

1 Introduction

The interaction of light with matter makes our life vivid and colorful. Natural dyes show an almost endless range of hues. The interplay between absorption, transmission, and scattering of light causes the variety of colors of flowers. Diffraction of light also leads to impressive colors, completely without dyes. Prominent examples of such dye less colors are the feathers of the birds of paradise or the iridescent colors in precious stones like the opal. The mankind was impressed by this colors ever since and tried to reproduce them. Besides textiles, furniture and buildings also glass was dyed from the ancient times on. The color of glass can be fabricated by adding metal ions to a glass melt, for example, copper oxide to get a blue hue.[1] Next to the ion staining also adding colloids can deliver coloring. An example for colloidal staining is the red color of the middle-aged vitros. Adding gold to the glass melt leads to an intense red. The origin of the red lies in the dispersion of gold nanoparticles in the glass.

Nowadays this colloidal gold or silver is in the focus of the scientist, in particular because of its optical and electrical properties. These noble metal nanoparticles are called plasmonic particles and show special features when exposed to light. The incoming electromagnetic wave of light interacts with the surface electrons of the metallic particles. A wave with the resonance frequency causes a dipole oscillation of the surface electrons of the colloid. This resonance is called localized surface plasmon resonance (LSPR). The LSPR of gold and silver colloids is in the ultra-violet and visible range of the electromagnetic spectrum and can be detected by conventional UV-Vis extinction spectroscopy. The LSPR position, the line shape, and intensity are dependent on various factors, for instance: size and composition of the colloid, shape, material, and particle environment.[2-5] This dependency makes these particles interesting for fundamental studies but also for various applications, such as refractive index sensing,[6, 7] calorimetric glucose detection,[8] surface enhanced Raman spectroscopy,[9, 10] wave guiding,[11] or light harvesting in photovoltaic devices.[12] However, tailoring the size, shape and composition of the metal colloids is crucial for use-oriented devices. There are many synthesis roots for plasmonic particles, which allow the fine-tuning of the desired resonance.[13-21] Such plasmonic building blocks are promising candidates for bottom up surface modifications with new optical functionalities.

Various ways and techniques for surface structuring with nanoparticles have been reported in literature. The approaches can be divided into three main methods: lithography, template assisted self-assembly techniques, and self-assembly. Among these techniques the simplest way to arrange colloids is the self-assembly into hexagonal close packed layers, for example by spin coating. In the case, when more complex structures are of interest particles can be deposited into grooves of lithographically produced silicon masters[22] or printed onto substrates with the aid of template assistance.[23] Such template assisted self-assembly approaches often use replica molds of silicon masters. In addition, wrinkled assisted self-assembly[24] is fully lithography free, where wrinkled elastomer substrates are used to arrange colloids into grid like pattern.

A huge variety of colloidal building blocks have been used for surface modifications: *e.g.* bare spherical gold[25] or silver particles,[26] metal-metal[27] or metal-dielectric core/shell colloids,[28] cubes[29], and rods.[30] Particles with well-defined LSPRs in bulk could change their optical properties, due to alterations in the particle environment, for example refractive index changes, particle aggregation, drying effects, or redox processes.

An alternative access route to tailored plasmonics is post-modification of pre-assembled colloids. Therefore, the precise control over the inter particle spacing or the patterning of the surface is essential. The named parameters are important, because plasmon coupling effects occur between gold or silver colloids, consequently the LSPR frequency changes. Additionally the position stability during the wet chemical post-treatment has to be guaranteed.

The main goal of this thesis was the template assisted surface modification with hard-core/soft-shell colloidal building blocks with respect to gain plasmonic functionalities. Two access routes were presented within this work: on the one hand, the plasmonic properties are controlled over the assembly process on the other hand over post-modification of patterned surfaces. The chosen colloids for that purpose were hybrid particles consisting of hard silver, gold or silica cores and a soft polymer shell, namely poly(*N*-isopropylacrylamid) (PNIPAM). The optical properties were distributed by the noble metal core. The PNIPAM micro gel showed thermo responsiveness and further functions, which were essential for the success of this thesis. In particular, five properties of the PNIPAM shell were of importance:

- The soft, hence deformable character of the shell that allowed surface pattering inaccessible with hard nanoparticles.
- The polymer shell stabilized the inorganic cores and allowed to work with high particle concentrations.
- Further PNIPAM served as a spacer to control the inter core distance.
- It immobilized the particles on the surface during wet chemical treatment.
- Its permeability allowed the post-modification.

The first part of this thesis addressed the soft character of PNIPAM, with focus on the wrinkled assisted assembly process of such hybrid particles, which were arranged into grid like structures. Silica-PNIPAM as well as Ag-PNIPAM particles were used. The attention was drawn to the soft shell and on the resulting surface structuring. Novel symmetries could be gained by using hard-core/soft-shell particles compared to hard colloidal spheres. We discovered a significant decrease in the inter particle distance, which is indeed caused by the presence of the shell. This was confirmed by Monte Carlo simulations. Additionally we showed that the compression of shell during the confinement assembly was sufficient to bring the Ag surface into plasmonic coupling distance. Moreover, the anisotropy of structuring was also found in the optical properties. This was shown by polarization dependent extinction spectroscopy.

Thereafter we presented the large area organization of PNIPAM coated gold stars in linear assemblies. We presented the seed mediated preparation of the gold stars, based on the overgrowth of spherical Au-PNIPAM particles. The linear assemblies were also fabricated with the help of wrinkle assistance. The particle solution as well as the assemblies on glass were characterized optically *via* UV-Vis extinction spectroscopy. Such gold nanostars were suitable for surface enhanced Raman spectroscopy (SERS). The SERS efficiency was tested of the PNIPAM-stars lines, the stars randomly deposited and compared with films of the initially spherical Au-PNIPAM particles. Further, we demonstrated that gas phase sensing with PNIPAM-stars is possible. The air pollutant pyrene was detected, because it was trapped in the PNIPAM-shell, close to the gold-surface where a high SERS enhancement took place.

The idea of seed mediated overgrowth of spherical Au-PNIPAM particles was adapted to immobilized nanoparticle films in the next step. The goal was to create a chip based plasmonic library with a distinct gradient in gold core sizes. This gradient was produced

by coating a hexagonal monolayer onto glass with subsequent overgrowth. The shell guaranteed the spatial separation of the cores to avoid plasmon coupling. Additionally, position stability was ensured, due to physical linkage to the substrate. Further, the shell gave control over the overgrowth process, because of diffusion limitation. The gradient in diameter ranged from 10 to 60 nm and was achieved by using a dip-coater. The particle coated glass slide was fully immersed in a gold growth solution. The exposure in the growth solution determined the reaction time and hence the core dimensions. The uniaxial gradient was fabricated by withdrawing the macroscopic glass slide. Thus, we were able to investigate the core size as a function of time. This relation allowed core size predictions and an accurate adjustment of the core dimensions. During the overgrowth neither secondary nucleation, nor Ostwald ripening was observed. The continuous gradient in size follows a continuous gradient in optical properties, which was visible with the naked eye. The glass slide showed a color gradient from nearly transparent to deep purple. This color gradient has its origin in the different LSPR frequencies. This was quantified by UV-Vis extinction spectroscopy and the size dependent LSRP spectra were compared with theoretical predictions from Mie theory.

The successful realization of plasmonic libraries with precise control over size and optic response demonstrated the potential of this concept. Nevertheless, there are cases where a precise characterization on the single particle level is necessary. Therefore, conventional UV-Vis spectroscopy is not suitable, due to the averaging measurements. Plasmonic properties of single colloids can be characterized by dark field spectroscopy.
Thereupon, we developed the method of plasmonic libraries further and showed by a proof of principle that this concept can be brought to the single particle level. Therefore, the glass slides were structured with Ag- or Au-PNIPAM colloids using template-assisted assembly. The templates were fabricated *via* replica molding of silicon masters with an elastomer. The particles were spin coated in the resulting grooves of the elastomer and deposited to glass slides with a wet transfer step. The inter particle spacing was 15 µm and could be adjusted over the master geometry. This pattern was well suitable for single particle dark field spectroscopy. We investigated the surface with AFM and compared the same area with dark field microscopy images. We showed for the first time dark field spectra of silver-core/PNIPAM-shell particles.
Such substrates are a cost efficient basis for further post-modifications and could be successfully used for combinatorial investigations, monitoring of catalytic processes,

creating libraries, and establishing standards. Not only gradients in core size but also in shape (stars, rods) and composition (gold-core/silver-shell) could be reached by combining PNIPAM-core/shell-particles with wet-chemical post-modification. This concept could also be expanded to linear assemblies of Au- or Ag-PNIPAM. A small coupling effect could be enhanced by gradiential post-modification and investigated with respect to core diameter.

References

1. W. Vogel, in *Glaschemie*, Springer Berlin Heidelberg, 1992, ch. 9, pp. 251-318.
2. S. Link and M. A. El-Sayed, *Journal of Physical Chemistry B*, 1999, **103**, 4212-4217.
3. X. Lu, M. Rycenga, S. E. Skrabalak, B. Wiley and Y. Xia, *Annual Review of Physical Chemistry*, 2009, **60**, 167-192.
4. L. M. Liz-Marzán, M. Giersig and P. Mulvaney, *Langmuir*, 1996, **12**, 4329-4335.
5. P. K. Jain and M. A. El-Sayed, *Chemical Physics Letters*, 2010, **487**, 153-164.
6. C.-J. Heo, H. C. Jeon, S. Y. Lee, S. G. Jang, S. Cho, Y. Choi and S.-M. Yang, *Journal of Materials Chemistry*, 2012, **22**, 13903-13907.
7. J. Zhao, A. Das, X. Zhang, G. C. Schatz, S. G. Sligar and R. P. Van Duyne, *Journal of the American Chemical Society*, 2006, **128**, 11004-11005.
8. H. Jang and D.-H. Min, *RSC Advances*, 2015.
9. R. Mukhopadhyay, *Analytical Chemistry*, 2007, **79**, 3265-3270.
10. D. Cialla, A. März, R. Böhme, F. Theil, K. Weber, M. Schmitt and J. Popp, *Anal. Bioanal. Chem.*, 2012, **403**, 27-54.
11. S. Lal, S. Link and N. J. Halas, *Nat Photon*, 2007, **1**, 641-648.
12. M. Karg, T. A. F. König, M. Retsch, C. Stelling, P. M. Reichstein, T. Honold, M. Thelakkat and A. Fery, *Materials Today*, 2014.
13. M. Grzelczak, A. Sánchez-Iglesias, B. Rodríguez-González, R. Alvarez-Puebla, J. Pérez-Juste and L. M. Liz-Marzán, *Advanced Functional Materials*, 2008, **18**, 3780-3786.
14. T. K. Sau and A. L. Rogach, *Advanced Materials*, 2010, **22**, 1781-1804.
15. R. Sardar, A. M. Funston, P. Mulvaney and R. W. Murray, *Langmuir*, 2009, **25**, 13840-13851.
16. B. V. Enustun and J. Turkevich, *Journal of the American Chemical Society*, 1963, **85**, 3317-&.
17. N. R. Jana, L. Gearheart and C. J. Murphy, *Langmuir*, 2001, **17**, 6782-6786.
18. M. Brust, M. Walker, D. Bethell, D. J. Schiffrin and R. Whyman, *Journal of the Chemical Society-Chemical Communications*, 1994, 801-802.
19. N. G. Bastus, J. Comenge and V. Puntes, *Langmuir*, 2011, **27**, 11098-11105.
20. J. Becker, O. Schubert and C. Sonnichsen, *Nano Letters*, 2007, **7**, 1664-1669.
21. C. Bullen, P. Zijlstra, E. Bakker, M. Gu and C. Raston, *Crystal Growth & Design*, 2011, **11**, 3375-3380.
22. T. Kraus, L. Malaquin, H. Schmid, W. Riess, N. D. Spencer and H. Wolf, *Nat Nano*, 2007, **2**, 570-576.
23. C. Hanske, M. B. Mueller, V. Bieber, M. Tebbe, S. Jessl, A. Wittemann and A. Fery, *Langmuir*, 2012, **28**, 16745-16750.
24. C. Lu, H. Möhwald and A. Fery, *Soft Matter*, 2007, **3**, 1530-1536.

25. C. Hanske, M. Tebbe, C. Kuttner, V. Bieber, V. V. Tsukruk, M. Chanana, T. A. F. König and A. Fery, *Nano Letters*, 2014, **14**, 6863-6871.
26. M. Müller, M. Karg, A. Fortini, T. Hellweg and A. Fery, *Nanoscale*, 2012, **4**, 2491-2499.
27. K. Sugawa, Y. Tanoue, T. Ube, S. Yanagida, T. Yamamuro, Y. Kusaka, H. Ushijima and T. Akiyama, *Photochemical & Photobiological Sciences*, 2014, **13**, 82-91.
28. M. Müller, M. Tebbe, D. V. Andreeva, M. Karg, R. A. Alvarez Puebla, N. Pazos Perez and A. Fery, *Langmuir*, 2012, **28**, 9168-9173.
29. L. J. Sherry, S.-H. Chang, G. C. Schatz, R. P. Van Duyne, B. J. Wiley and Y. Xia, *Nano Letters*, 2005, **5**, 2034-2038.
30. M. Tebbe, M. Mayer, B. A. Glatz, C. Hanske, P. T. Probst, M. B. Müller, M. Karg, M. Chanana, T. König, C. Kuttner and A. Fery, *Faraday Discussions*, 2014.

2 OVERVIEW OF THIS THESIS

This Chapter will provide a general overview of the thesis. First, an introduction to the theoretical background and a brief review of the status of the field will be given in Chapter 3. The Chapter 4 to 6 present the published results of this thesis. Chapter 7 gives an outlook in the form of a manuscript, which is prepared for future publication. My entire scientific attempts target the template assisted and controlled surface modification with hard-core/soft-shell plasmonic building blocks to achieve optical functionalities.

2.1 Outline and Synopsis

The main scope of my work was the creation of functional surfaces with hard-core/soft-shell plasmonic colloidal building blocks in respect to optical surface functionalization. With the focus on:

- bottom up surface modification using self-assembly and template assisted self-assembly techniques
- introducing optical functionalities *via* plasmonic nanoparticles
- tailoring the optical properties *via* the deposition or using post-modification

The colloid types, which were used in this framework, were hard-core/soft-shell colloids. An advantage of such hybrid particles is the plurality in functionalities. The optical properties were introduced by the usage of either silver or gold nanoparticles as core material encapsulated in a micro gel. Silver and gold show a so-called "localized surface plasmon resonance" (LSPR). This resonance lies for both noble metals in the ultra violet and/or in the visible range of the electromagnetic spectrum. This resonance is also present if such particles are deposited on surfaces. This makes them interesting for sensing applications, for instance surface enhanced Raman spectroscopy (SERS) and refractive index sensing or other applications like wave guiding, light harvesting in photovoltaic or monitoring catalysis. The soft polymeric poly(*N*-isopropylacrylamide) shell contributed a multitude of other advantages. First, the shell prevents the plasmonic cores from aggregation, which made it possible to work with highly concentrated dispersions important for large-scale coatings. Second, the micro gel is stimuli

responsive to changes in temperature, pH, or ionic strength. Additionally it acts as a spacer for the plasmonic cores to keep their individual optical properties. The shell is also soft and deformable which allowed surface modifications inaccessible for hard sphere systems. Also important was the permeability of the gel network, which allowed a chemical post-modification of the core. These hybrid particles provided a manifold tool kit for functional surface modifications. This thesis will demonstrate how glass surfaces can be altered with these colloidal building blocks for a variety of purposes.

The wrinkle-assisted assembly for Ag-PNIPAM is introduced in **Chapter 4**. We assembled the core-shell particles in lines and discussed the influence of the shell on the structuring. We showed, that anisotropy was not only found, due to the linear alignment within the wrinkles, but also on a smaller length scale within the particle lines. The Ag-cores were not closed packed like in a system of hard spheres, because this was prevented by the shell. This linearity of the structure and the deformability of the shell caused also changes in optical properties, as we were able to detect with polarization depended UV-Vis spectroscopy. The quality of these grid like patterns was good, even on the cm scale, which we proved with laser diffraction experiments.

Chapter 5 demonstrates how this wrinkle-assisted assembly technique could be adapted to gold-star/poly-*N*-isopropylacrylamide particles, which were promising candidates for "surface enhanced Raman spectroscopy" substrates. The wrinkle-assisted assembly enabled the controlled deposition, which was important for SERS evaluation. The stars were fabricated by changing the core size and shape of spherical Au-PNIPAM using a seed mediated synthesis route in bulk, possible due to the permeability of the micro gel. The shell acted again as spacer to prevent undesired touching of plasmonic particles. Further, the SERS efficiency of the PNIPAM-stars was presented. Moreover, the sensing potential of the SERS active gold stars encapsulated in the adhesive PNIPAM shell was demonstrated.

We developed the idea of particle post-modification further in **Chapter 6**. Although the post-modification was applied to particle films already assembled on the substrate. For this study we spin coated the gold-PNIPAM particles and achieved a monolayer in hexagonal arrangement. The post-modification was performed *via* dip coating which enabled the fabrication of a plasmonic gradient. This offered access to plasmonic screening substrates and plasmonic libraries. These plasmonic gradients could only be

establish, if the plasmonic cores were well and regular separated from each other - realized through the PNIPAM shell. Furthermore, the shell provided the necessary adhesion during the core enlargement.

The idea of plasmonic screening substrates was picked up in **Chapter 7**, but with focus on single particle spectroscopy. It was shown that the transfer of gold and silver core/shell colloids was also possible with elastomer templates molded from a silicon master. This setup offered the opportunity of micrometer inter particle spacing. This was in particular necessary for single particle dark field spectroscopy. The shell itself enlarged the net particle size, which facilitated the deposition in the elastomer templates. The shell did not hinder the detection of single particle spectra and would provide the position stability for further post-modification treatments as shown in **Chapter 6**.

2.2 Content of the Individual Chapters

2.2.1 *Hard-core/soft-shell and their impact on surface modification*

Chapter 4 addresses the wrinkle-assisted assembly of core-shell particles and the influence of the soft shell on the particle assembly. Surface structuring with plasmonic hybrid particles was the central point of this thesis. A lithography free approach was realized by advancement of the wrinkle-assisted confinement assembly (CA) to the so-called spin-release (SR). CA was performed by drying a polystyrene dispersion under confined conditions between a flat and a wrinkled substrate.[1] In contrast to this technique the particles were pre-assembled in the SR approach into the grooves of the wrinkles (Scheme 2-1a) and transferred with the help of capillary forces to a wetted glass slide (b). This pre-alignment was necessary, to gain a uniform surface patterning using the hard-core/soft-shell particles. After drying, the wrinkle could be removed and the particles were deposited on the target substrate (c).

Scheme 2-1 Depiction of the spin-release process. The particle suspension is put on top of the wrinkles (a) and excessive particles are removed by spin coating. The particles remaining in the cavities of the substrate are brought into contact with a wetted glass slide (b). After drying, the wrinkled PDMS stripe is pealed of and the particles are transferred to the glass (c). (Taken from Chapter 5)

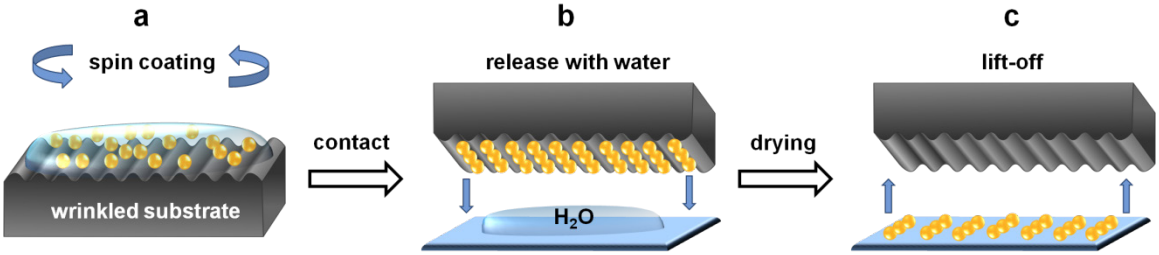

Inorganic-core/soft-poly(*N*-isopropylacrylamide) particles were used for the anisotropic patterning. First studies were made with silicon core particles. They were utilized as a model system to investigate the influence of the shell and reaction parameters to the assembly process. The dependency of the core size and the wavelength was discussed in the means of achievable geometries, ranging from single lines, over zigzag lines to pyramidal structures. The soft shell played an important role in the assembly process. It facilitated the same deposition geometry independent of the core size or the core material. Furthermore, the shell enabled the formation of structures, which were hexagonal, but non closed packed with angles deviating from 60°, regarding the core positions. This was reproduced by Monte-Carlo simulations. The calculations could reconstruct the assemblies, but only if a soft repulsive shell potential was added to the hard sphere potential of the cores. Otherwise the particles were arranged like hard spheres as in Ref. 1, thus in a hexagonal closed packed pattern (see Figure 2-1).

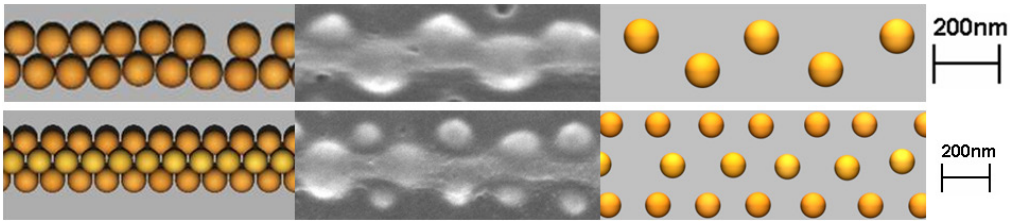

Figure 2-1 Comparison of the local structure from a SEM image of a Ag-PNIPAM sample (middle) and Monte Carlo (MC) simulations (left and right). On the left hand side, the simulations are performed for hard spheres. The particles are arranged in a hexagonal closed packing (with some defects). On the right hand side are the results for MC-simulation presented, modeled with an additional soft potential. The cores are separated from each other and the inter particle angle is distorted and deviates from 60°. The shell is not drawn for the sake of clarity. (Taken from Chapter 4)

The presence of the shell prevented the cores from touching but the deformability of the shell led to smaller inter core distances than expected for just touching shells. This made this system interesting for plasmonic applications. To verify this fact Ag-PNIPAM colloids were successfully deposited *via* the spin-release. Polarized UV-Vis absorbance

spectroscopy proofed that the anisotropy of the patterning was also visible in the optical properties. It was further demonstrated that the shell compression during the assembly was sufficient to reveal a small plasmonic coupling effect.

2.2.2 *Application of PNIPAM core/shell particles - SERS platform for gas phase sensors*

In Chapter 5 the fabrication of a new platform for gas phase sensing is presented. The sensors were PNIPAM coated nanostars (NS) substrates and the sensing method was surface enhanced Raman spectroscopy (SERS). At first, the synthesis of the gold star-core/PNIPAM-shell particles was demonstrated and is depicted in Scheme 2-2. The spherical gold-PNIPAM hybrid particles (a) were used as seeds for the post-modification into gold stars. These precursor particles were added to a solution of poly(vinylpyrrolidone) (PVP) and *N*,*N*-dimethylformamide (DMF) (b). The PVP is allowed to diffuse trough the loose PNIPAM network overnight. After washing, a gold salt solution was added (c) and the stars started to grow as indicated by a color change of the solution from slight pink to blue (d).

Scheme 2-2 Synthesis of gold star-core/PNIPAM-shell particles. Spherical gold-core/PNIPAM-shell particles are used as seeds (a). The seed particles are dispersed in ethanol. This colloid dispersion is added to a solution containing PVP in DMF and kept overnight (b). After washing, the gold salt solution is added (c) and the stars start to grow within 20 min.

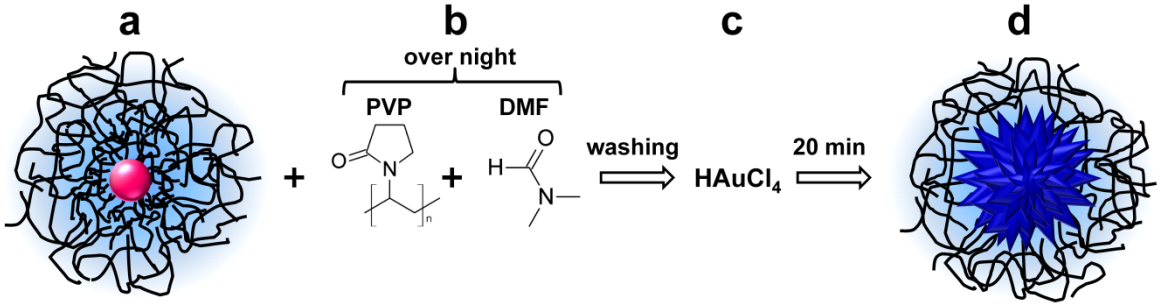

The color change confirmed not only the geometrical metamorphosis but also the appearance of plasmon coupling between the spikes of the stars. The near field enhancement due to the spikes and the hot spots caused by plasmon coupling could be used for SERS sensing. The hybrid particles were deposited to a substrate *via* spin-release. This ensured a large and homogeneous coverage in linear assemblies. The shell acted as spacer between the single particles to avoid additional inter particle coupling and prevented direct touching, which would deactivate the hot spots. Raman mapping of benzenethiol (BT) with NS-PNIPAM lines, randomly deposited NS-PNIPAM and spherical Au-PNIPAM particles revealed that the Raman intensity of the line patterning

was slightly lower than for the randomly deposited NS. Nevertheless the line pattern showed less intensity fluctuation and remained constant over the whole range. The spherical particles showed nearly no Raman intensity. The shell had not only the role of a spacer during the assembly, but trapped also molecules out of the gas phase. This was verified by detecting the air pollutant pyrene. A comparison between PNIPAM coated NS and bare NS is presented in Figure 2-2. The vibrational SERS pattern of the pyrene was only detected if the experiment was performed with NS-PNIPAM particles. Bare nanostars were unsuitable, because the analyte could not bind at the surface of the stars, which was essential for SERS detection.

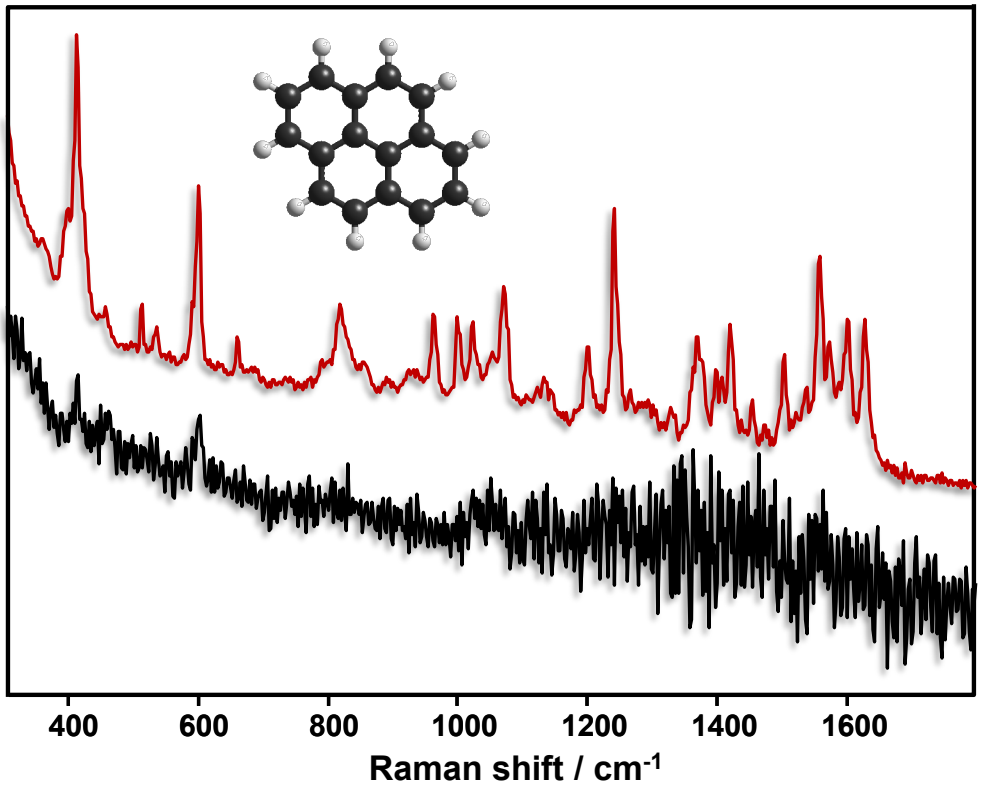

Figure 2-2 Comparison of the SERS sensitivity between PNIPAM coated NS (red line) and uncoated NS (black line) to detect the air pollutant pyrene. Just the PNIPAM coated NS deliver a usable SERS spectra. (Taken from Chapter 5)

2.2.3 *Plasmonic gradient materials*

The focus of Chapter 6 was on post-modification of structured surfaces to change the optical properties. The focus lied in particular on the creation of a plasmonic gradient, useful for the fabrication of screening substrates or libraries. In this work, a monolayer of gold-core/PNIPAM-shell particles was assembled onto microscopy slides using spin coating. The large shell (diameter = 250 nm) acted as spacer like in Chapter 4 and 5 and

ensured an equidistant spatial separation between the small plasmonic cores (diameter = 15 nm) (see Figure 2-3a).

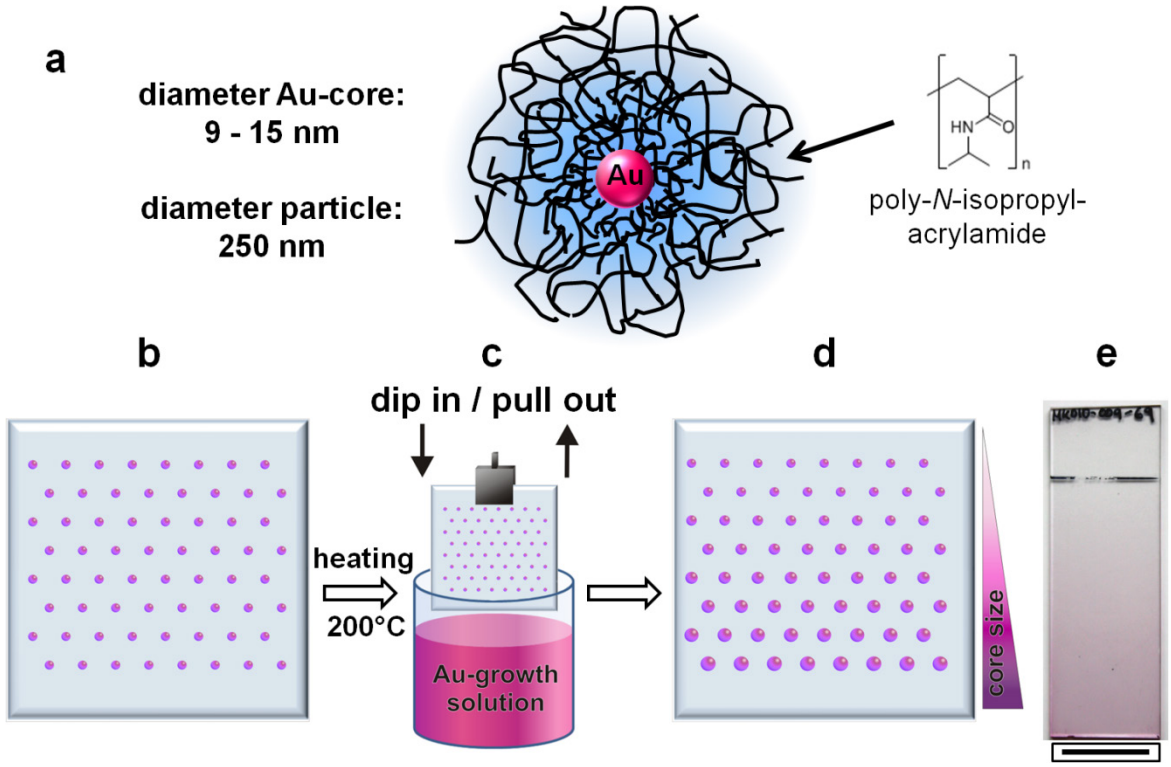

Figure 2-3 (a) depicts the hybrid particle (not drawn to scale), consisting of a gold core encapsulated in a permeable PNIPAM micro gel shell. (b) to (d) present the growth procedure, whereas the shell is not drawn for the sake of clarity: a monolayer of hexagonal packed particles (b) is heated to 200 °C for particle immobilization. The slide is dipped into a gold growth solution containing gold-salt, surfactant, and reducing agent (c). Pulling the substrate out lead to the gradient in core size (d). The digital camera image in (e) shows that the change in size can be seen with the naked eye, due to a color change from nearly transparent to deep purple. The scale bar is 2 cm.

The permeable network of the shell allowed further the post-treatment for the enlargement of the cores. This was already shown in Chapter 5 and in Ref. 2, but compared to this approaches, the post-treatment was performed on substrate and is depicted in Figure 2-3b to d. The glass slide (b) was placed in a gold growth solution, containing gold salt, reducing agent, and surfactant. A thermal treatment prior to the growth procedure guaranteed the immobilization of the particles. The size modification was performed *via* dip coating (c). The substrate was fully immersed in the growth solution and pulled out immediately. Due to the different exposure times a size gradient from small at the top (diameter = 9-15 nm) to large (diameter = 56 nm) at the bottom was achieved (d). It was also found that the growth process was diffusions limited, as a result of the PNIPAM shell. The modified substrate showed a color gradient from nearly transparent at the top to deep purple at the bottom, visible with the naked eye as illustrated in Figure 2-3e.

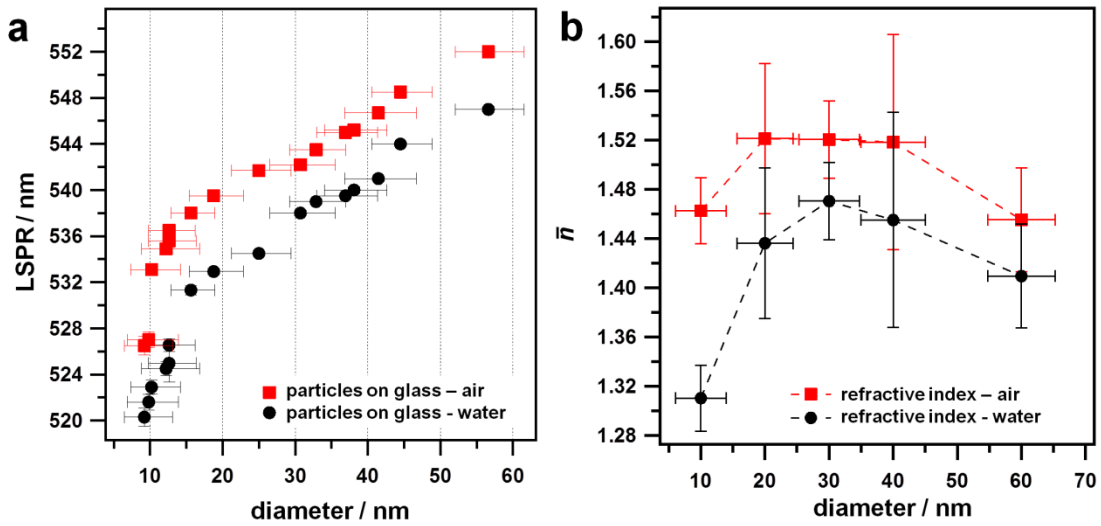

Figure 2-4 Optical characterization of the plasmonic gradient substrates. (a) shows the experimental results of the LSPR position dependent on the core size measured by UV-Vis extinction spectroscopy. The measurements are performed under air (red squares) and in water (black circles). (Taken from Chapter 7). (b) shows the apparent surrounding refractive index as expected from the experimental LSPR positions observed against air (red squares) and in water (black circles). (Taken from Chapter 7)

Position dependent UV-Vis extinction spectroscopy is presented in Figure 2-4a. The measurements under air verified an overall LSPR shift of 26 nm. The influence of the refractive index n was investigated, by UV-Vis measurements in water. The inter play between shell, surrounding medium, and core size led to an unexpected trend for the LSPR shift, which is explained by calculating an average surrounding refractive index $\bar{n}$. As shown in Figure 2-4b n changes for different core sizes. We compared our findings also with calculations from Mie theory.

2.2.4 *Plasmon-core/PNIPAM-shell particles - spectroscopy on the single particle level*

We showed in Chapter 6 how post-modification of core-PNIPAM shell particles can be used to generate a continuous gradient in core size and correspondingly in plasmonic properties. The scope of Chapter 7 was the evolution from assembly studies to single particle characterization *via* dark field scattering spectroscopy. For this spectroscopy technique, the particles have to be separated from each other over a distance of multiple micrometers. This was achieved by template assisted self-assembly. The templates were elastomer replica molds of silicon masters. The inter-pillar spacing of the masters was 15 µm. In this way, templates with holes were created into which the particles were deposited with the help of spin coating. The transfer from PDMS to glass was performed according to Chapter 4 using a wet transfer step. The structure of the PDMS master was

accurately reproduced on glass by the deposited colloids (see Figure 2-5a and b). Ag-PNIPAM as well as Au-PNIPAM particles were used. The dark field spectroscopic analysis (d) for the single Ag-PNIPAM particle matched well the UV-Vis measurements of assemblies and proved that the shell did not hinder the scattering signal of the particles. The particles of the dark field analysis were also compared with atomic force microscopy (AFM) height images on the same spot, which allowed an allocation between spectra and particle (c and d).

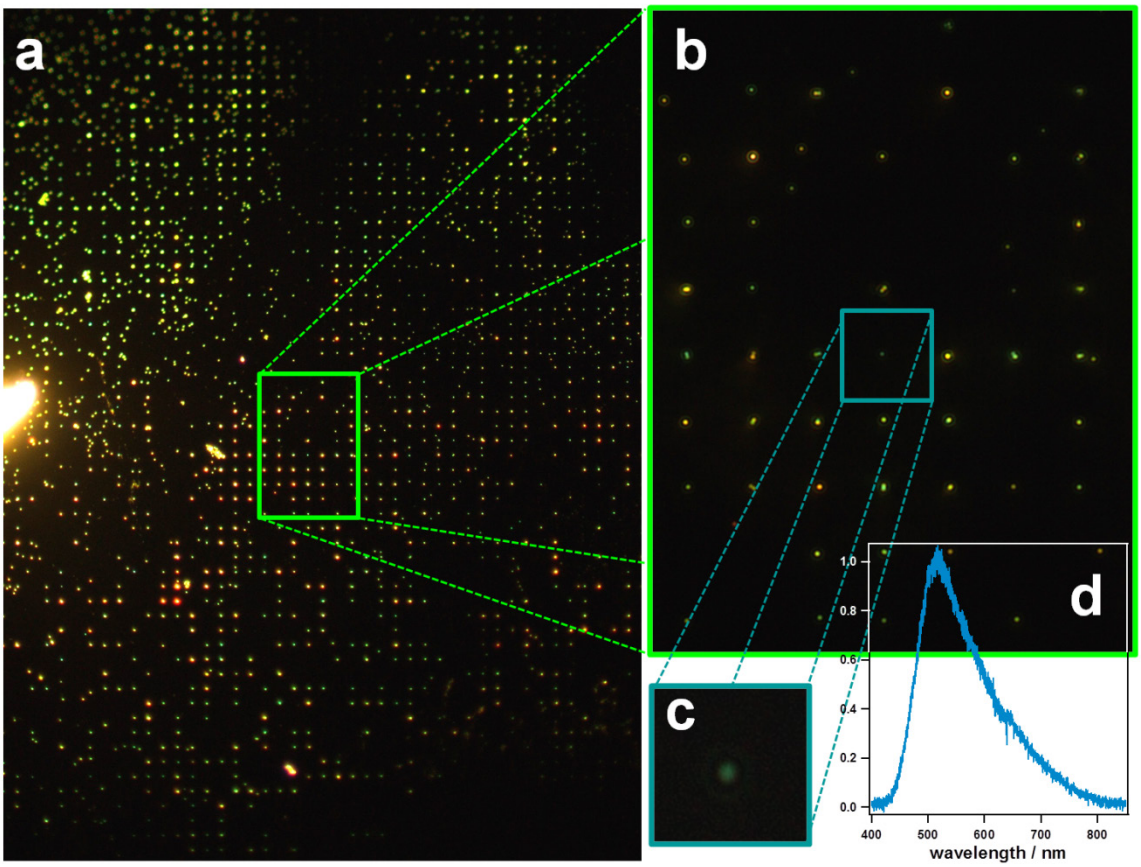

Figure 2-5 Transmission dark field microscopy images of Ag-PNIPAM particles on glass. (a) shows a representative image with 10x magnification. (b) shows the framed area with a 40x magnification. A single Ag-PNIPAM particle is presented in (c) and is the digital zoom of the framed area in (b). The corresponding scattering spectrum of this particle is presented in (d).

2.3 Individual Contributions to the Presented Publications

The results and findings presented in this thesis are the result of collaborations with other scientist and have been published as indicated. In the following, the contributions of each coworker are specified. The asterisks denote the corresponding author.

 This work was published in *Nanoscale* (**2012**, 4, 2491-2499) under the title :

> **Wrinkle-assisted linear assembly of hard-core/soft-shell particles: impact of the soft shell on the local structure**
> by Mareen B. Müller, Matthias Karg, Andrea Fortini, Thomas Hellweg and Andreas Fery*

I carried out all the experiments, except of the particle synthesis, I performed all SEM and AFM measurements, evaluated the data and wrote the publication. Matthias Karg synthesized the nanoparticles, built the laser pointer setup for the diffraction measurements, wrote parts of the manuscript, and was involved in scientific discussions. Andrea Fortini conducted the Monte-Carlo simulations and wrote parts of the manuscript. Thomas Hellweg corrected the manuscript and was involved in scientific discussions. Andreas Fery supervised the project and corrected the manuscript.

 This work was published in *Langmuir* (**2012**, 28, 9168-9173) under the title:

> **Large-Area Organization of PNIPAM-Coated Nanostars as SERS Platforms for Polycyclic Aromatic Hydrocarbons Sensing in Gas Phase**
> by Mareen B. Müller, Moritz Tebbe, Daria V. Andreeva, Matthias Karg, Ramon A. Alvarez Puebla, Nicolas Pazos Perez and Andreas Fery*

I carried out the sample preparation, analyzed the morphological structure with AFM, did some of the SEM measurements and parts of the data evaluation. I was also involved in the optical characterization and wrote parts of the manuscript. Moritz Tebbe and Daria V. Andreeva were involved in scientific discussions. Matthias Karg synthesized the seed particles, wrote parts of the manuscript, and was involved in scientific discussions. Ramon A. Alvarez Puebla did parts of the SERS characterization, was involved in scientific discussions, and corrected the manuscript. Nicolas Pazos Perez synthesized the star shaped nanoparticles, performed the SERS measurements, and did some of the SEM measurements. Andreas Fery supervised the project and corrected the manuscript.

 This work was published in *ACS Nano* (**2014**, 8, 9410-9421) under the title:

> **Plasmonic Library Based on Substrate-Supported Gradiential Plasmonic Arrays**
>
> by Mareen B. Müller, Christian Kuttner, Tobias A. F. König, Vladimir V. Tsukruk, Stephan Förster, Matthias Karg* and Andreas Fery*

The project was initialized by Matthias Karg and me. I carried out all the experiments, imaged all samples *via* AFM and SEM, did the optical characterization via UV-Vis spectroscopy, evaluated the data, and wrote the publication. Christian Kuttner evaluated the effective diffusion coefficient by the incremental regression method and wrote parts of the publication. Tobias A. F. König conducted the Mie theory simulations, was involved in scientific discussions, and wrote parts of the manuscript. Vladimir V. Tsukruk, Stephan Förster, and Matthias Karg were involved in scientific discussions. Matthias Karg contributed the initial core/shell-particles and wrote parts of the manuscript. Andreas Fery supervised the work and corrected the manuscript.

Chapter 7 is unpublished work and prepared for future publication under the title:

> **Producing a Plasmonic library of plasmonic-core/PNIPAM-shell particles on the single particle level**
>
> by Mareen B. Müller, Kirsten Volk, Tobias Honold, Xingzhan Wei, Matthias Karg, Paul Mulvaney, and Andreas Fery*

The work was initialized by Andreas Fery, Matthias Karg and me. I carried out all experiments except of the particle synthesis. I recorded the AFM images, the dark field pictures and made the spectroscopic dark field investigation. I evaluated all data and wrote the manuscript. Kirsten Volk synthesized the silver-PNIPAM particles and characterized them *via* TEM. Tobias Honold carried out the synthesis of the Au-PNIPAM particles and did their TEM characterization. Xingzhan Wei fabricated the silicon masters with electron beam lithography. Matthias Karg, Paul Mulvaney, and Andreas Fery were involved in scientific discussion. Andreas Fery supervised the work.

References

1. A. Schweikart, A. Fortini, A. Wittemann, M. Schmidt and A. Fery, *Soft Matter*, 2010, **6**, 5860-5863.
2. R. Contreras-Cáceres, A. Sánchez-Iglesias, M. Karg, I. Pastoriza-Santos, J. Pérez-Juste, J. Pacifico, T. Hellweg, A. Fernández-Barbero and L. M. Liz-Marzán, *Advanced Materials*, 2008, **20**, 1666-1670.

3 STATUS OF THE FIELD AND THEORETICAL BACKGROUND

This chapter provides an overview of the status of the field and a basic theoretical background necessary to understand the results of this work. The first part of this chapter will focus on techniques for surface modification. Especially the template assisted self-assembly will be explained, since it played an important role for nanoparticle assemblies within this work. In the second part, the attention is drawn on plasmonic nanoparticles. These metallic particles offer many ways to alter optical properties of substrates. In this context, the fundamentals of the so-called localized plasmon resonance will be discussed as well as ways to control and manipulate this optical feature. The last part is dedicated to hard-core/soft-shell particles, explicitly inorganic hard-core/PNIPAM-shell particles. These were the colloidal building blocks used in this work.

3.1 Surface modification: From self-assembly to template assisted self-assembly

The modification of surfaces can be divided into four main groups: conventional "lithography techniques", "soft lithography" (SL), "template assisted self-assembly" (TASA) and simple "self-assembly" (SA). The focus of the following chapter will be on SA, SL and TASA.

The conventional so-called "hard lithography procedures" play an important role in the semiconductor industry for computer chip fabrication, but are not scope of this work. The attention of the reader is drawn to the existing articles, which address "extreme UV"[1], "soft x-ray"[2], "e-beam writing"[3] or "focused ion beam"[4] lithography.

Also not in the focus of this work, but worth to mention are methods like direct printing methods for instance "laser direct writing"[5] or "inkjet printing"[6].

3.1.1 *Particle self-assembly*

Self-assembly is defined by IUPAC as the "[s]pontaneous and reversible organization of molecular entities by noncovalent interactions" whereas "[...] a system of pre-existing components, under specific conditions, adopts a more organized structure through

interactions between the components". This "[...] noncovalent interactions are van der Waals interactions, π–π interactions, electro static interactions, and hydrogen bonds".[7] Also, gravity or capillary forces can drive the components - namely colloids - into regular structures. SA is an easy way to functionalize surfaces to introduce new properties ranging from self-cleaning substrates to optical applications.

The simplest self-assembly particle deposition is sedimentation, due to gravity with subsequent drying (Figure 3-1a). The accelerated process is centrifugation (b). The particles can be pressed to a surface (c) trough filtration. In addition, deposition *via* convective assembly (d), due to capillary forces is possible. Thin films can be generated by flow cells. Solvent free methods like pressing procedures are also suitable to force particles into ordered structures.[8]

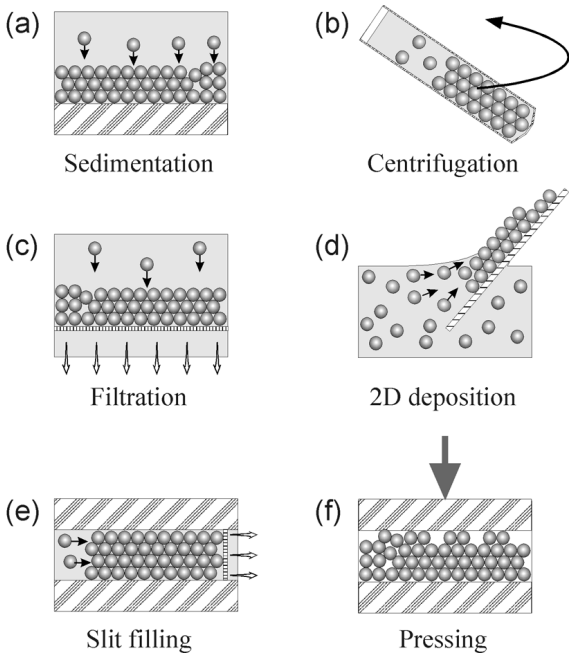

Figure 3-1 Methods to produce colloidal assemblies through (a) sedimentation, (b) centrifugation, (c) filtration, (d) convective assembly via dip coating, (e) thin film preparation in flow cells or (f) particle pressing. "Reprinted from Publication, *Current Opinion in Colloid & Interface Science*, 5, Orlin D. Velev, Abraham M. Lenhoff, Colloidal crystals as templates for porous materials, 56-63, Copyright **2000**, with permission from Elsevier" Ref. 8

An accelerated sedimentation process combined with capillary forces is spin coating. The particle suspension is put on the substrate and rotated with the velocity v_{spin} until the solvent is evaporated and a particle film remains. The aim is a smooth homogeneous

layer. This is achieved by centrifugal force with the velocity v_{radi}, which induces the spreading of the film. Over time, the film thickness is reduced until nearly all solvent is evaporated. Close to the dried state, the evaporating solvent between the particles causes a strong convective flow between the colloids, which pushes them together. The layer thickness and coverage are dependent on viscosity, drying rate, particle concentration, surface tension, acceleration, spin speed and wettability of the substrate.[9, 10] Figure 3-2a shows the spin coating process for a particle suspension on a flat substrate. It is important to adjust the parameter in the right fashion, else the surface coverage after drying is too low (b) or too high (c) and not uniform and homogeneous (d) like desired.

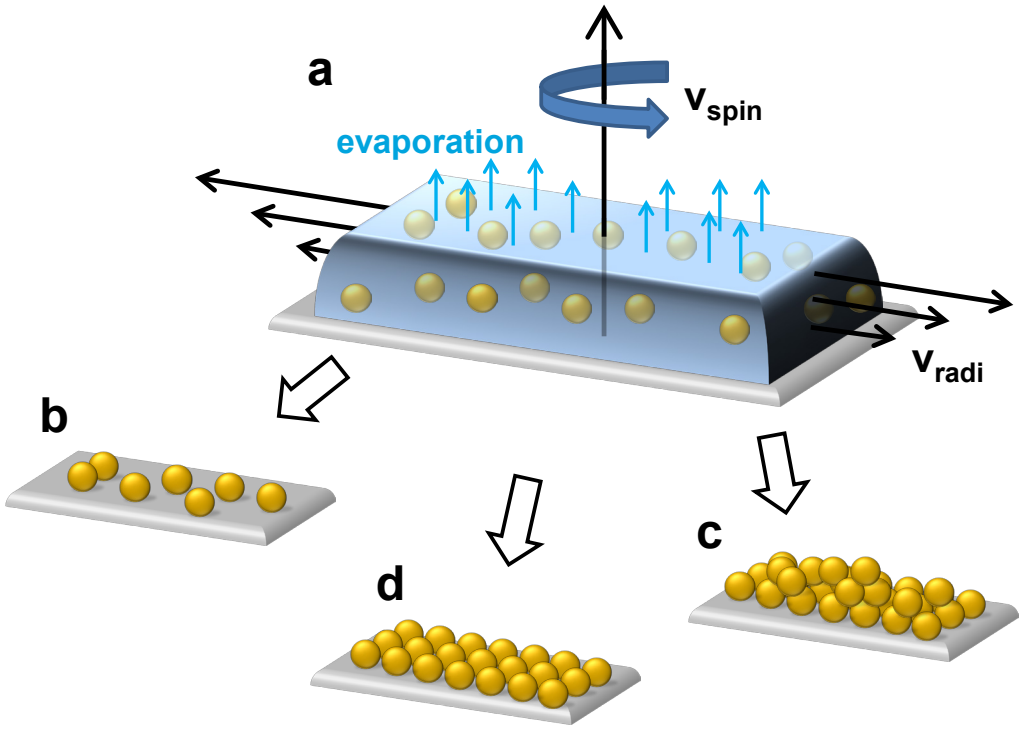

Figure 3-2 Drawing of the spin coating process depicted in (a). The rotation with the velocity v_{spin} introduces the centrifugal force, which spreads the suspension with the velocity v_{radi}. During spin coating, the solvent evaporates and the particle deposition takes place. Incorrect parameters lead either to a lack (b) or to excessive (c) particles on the substrate. Well adjustment leads to 2D or 3D colloidal crystals.

Spin coating is a fast and cost-efficient method but limited to planar 2D or 3D hexagonally close-packed arrays. To gain patterns that are more complex it is necessary to use chemically or topographically prestrucutred templates, which will be discussed in the next sections.

3.1.2 *Soft lithography: micro contact printing*

Soft lithography is a versatile tool to change the surface properties of substrates in multiple fashions. The technique we focus on is the so-called micro contact printing

(μCP). It was developed in the 1990s in the group of G. Whitesides and is meanwhile one of the most important soft lithography techniques.[11, 12] The basic concept of this soft lithography method is the replica molding of a master with silicon based elastomers, mostly polydimethylsiloxane (PDMS). The principle is depicted in Scheme 3-1(a) to (f). In the first step (a), the viscous PDMS is poured on a silicon master with the desired topography. After the PDMS is cured it can be stripped off the master (b) having the inverse profile. Following, the ink is placed on top of the PDMS (c). After removing excessive ink and drying, a layer of the dye covers the surface of the stamp (d). The ink is deposited to the desired substrate by contact printing (e), whereas the ink is transferred just from the contact areas (f) and stays in the grooves of the stamp.

Scheme 3-1 Depiction of the μCP procedure according to Whitesides. The elastomer polydimethylsiloxane (PDMS) is poured on a silicon master for replica molding (a). After curing the PDMS, it can be stripped (b) off and inked with a dye (c). After removing the excessive ink and drying (d), the PDMS stamp is brought into contact with the substrate (e). After certain contact time the PDMS is pulled off and the ink remains at the contact areas (f). Adapted with permission from Ref. 12.

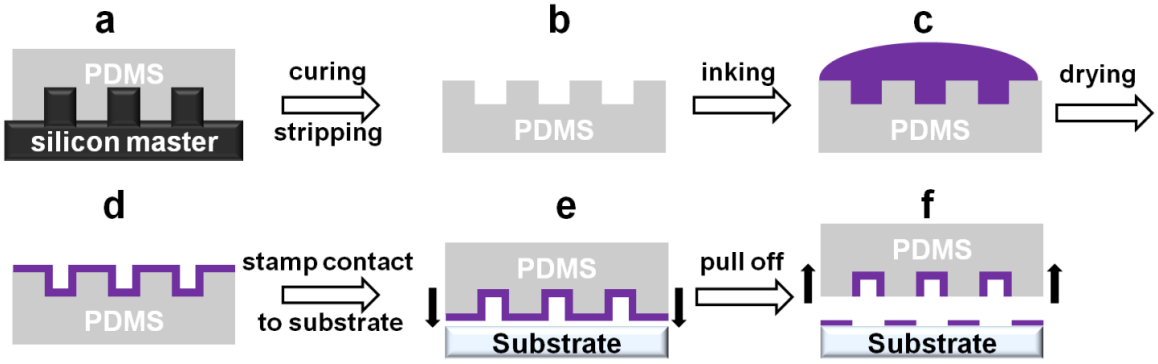

Many substances can be transferred in this manner. Originally, a layer of thiols was transported to a gold surface in a patterned fashion.[11] But also fluorescently labeled DNA[13] has been used to pattern surfaces. This technique can also be utilized to generate chemically structured substrates *e.g.* to produce wettability contrasts or electrostatically patterned surfaces.[14] Using a "ink pad" covered with particles makes also particle transfer printing possible, for instance shown by K. Tae-Ho for quantum dot displays fabrication.[15]

Particles have not mandatorily to be transferred from the top of the PDMS structure, but can also be deposited into the grooves *via* SA techniques followed by a transfer step. This technique is called "template assisted self-assembly" It is called this way, because the self-organization of the particles is assisted by topographically structured templates. A. Rey *et al.* presented in their work a way of aligning gold nano rods into channels of

PDMS. The particle deposition was controlled over the channel geometry.[16] PDMS templates with spherical grooves have been used by the group of H. Wolf for gold rod deposition.[17]

Further, the utilization of PDMS is not mandatory. Y. Yin *et al.* presented how monodisperse polystyrene colloids can be assembled into different geometries with the help pf convective assembly using a fluid cell with a lithographically structured wall.

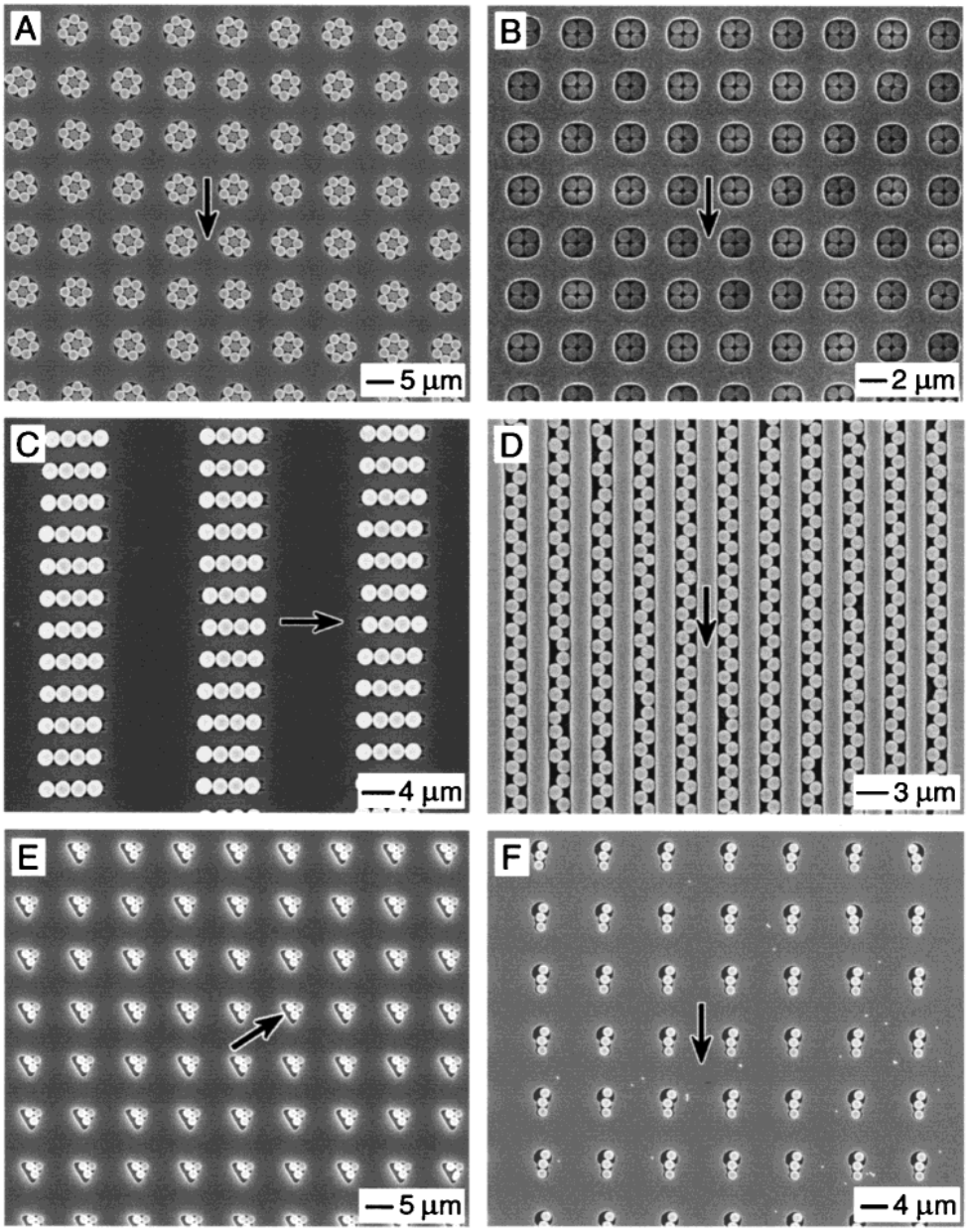

Figure 3-3 SEM images polystyrene particles assembled in various ways. Dependent on the geometry of used templates and the particle size, different types of particle arrangements could be achieved. (A) shows flower like aggregates, squares (B), short chains (C), zigzag lines in (D), triangular clusters (E) and short chains were the template consist of two cylindrical holes with different sizes. "Reprinted with permission from Y. Yin, Y. Lu, B. Gates and Y. Xia, *Journal of the American Chemical Society*, **2001**, 123, 8718-8729. Copyright 2001 American Chemical Society." Ref. 18

As shown in Figure 3-3 A to F various ways of particle clusters are possible just by changing the template and varying the particle size. The authors presented spherical (A) and square like (B) arrangements, short particle chains (C) and (F), zigzag lines (D), and triangular clusters (E).[18]

The here discussed examples of μCP and TASA, showed that these techniques are mighty tools for surface structuring. Unfortunately, they are still bound to lithographically produced masters with their limitations and disadvantages (time consuming, expensive, special equipment, harsh conditions, limited scalability...). How this lithography dependency can be overcome will be explained in the next paragraph.

3.1.3 *Lithography free template assisted particle assemblies - Wrinkle-assisted assembly*

Surface wrinkled substrates. To overcome the usage of replica molding of PDMS from lithographically produced masters one can operate with substrates which are fabricated by controlled wrinkling. The term of controlled wrinkling describes the targeted usage of mechanically instabilities. This is performed by working with elastomers. A widespread used elastomer is the PDMS (Scheme 3-2a) which is exposed to oxygen or UV/ozone plasma under stretched conditions. During plasma oxidation (b) of the PDMS, the surface is transformed into a rigid glass like layer. After strain release, sinusoidal wrinkles appear perpendicular to the direction of the strain (c).[19] This happens, due to different elastic moduli between the rigid thin layer on top and the elastic PDMS underneath. The elastomer bends if a critical compression stress is applied. The driving force for the bending under compression is the lower mechanical energy for a bended surface than for a flat surface. If the critical compression is now applied to the elastomer in the two-component system, it answers with wrinkling instead of bending, because the mechanical deformation energy is lower for a wrinkled surface than for the bend surface. To achieve permanent wrinkles the rigid layer is produced while the elastomer is stretched. After releasing the strain, the wrinkles are formed.[20-22]

During strain release of such substrates defects and cracks can occur. Defects are named points where two wrinkles merge into one, also-called Y-junctions. The faster the strain is released the more Y-defects arise. The reasons for the appearance of these defects are E-moduli fluctuation within the elastomer, caused during the preparation. To fabricate the PDMS a Pt-catalyzed polymerization of the alkenylsiloxane crosslinker with the

hydrosiloxane oligomers is done.[23] This polymerization is uncontrolled and local inhomogenieties in the cross-linking density and hence in the E-moduli are formed.[24] Decreasing the release speed, the rate of the defects decreases but the number of cracks is increased. Cracks are understood as fractures in the glass like layer perpendicular to the wrinkles. The elongated elastomer is compressed perpendicular to the strain orientation depending on the Poisson ration of the material. During relaxation, the stress in the elastomer is released just in the direction of the strain. Thus, the constricted areas expand again and cause the breaking of the rigid surface.[20]

Scheme 3-2 Schematic drawing of the wrinkling process. The PDMS elastomer stripe (a) is elongated with a certain strain ε and exposed to oxygen plasma under strained conditions (b). The generated oxide layer *h* is thin (nanometer range) compared to the thickness *D* (millimeter range) of the PDMS. After relaxation (c) sinusoidal wrinkles occur. (Adapted from Chapter 5)

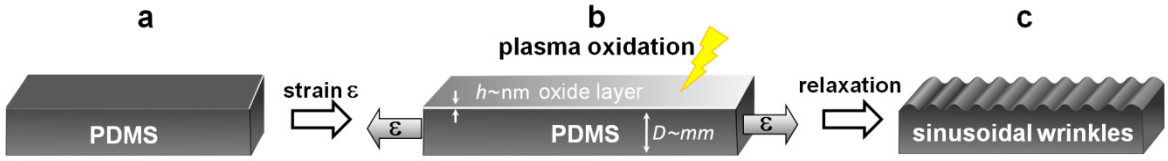

The wavelength λ and the amplitude A of the sinusoidal wrinkles can be controlled over the thickness h of the glass like layer. A prediction of the wavelength and amplitude is possible with the following equations:

$$\lambda = 2\pi h \left(\frac{E_l(1-\nu_s^2)}{3E_s(1-\nu_l^2)} \right)^{1/3} \qquad \textbf{3-1}$$

$$A = h\sqrt{\left(\frac{\varepsilon}{\varepsilon_c} - 1\right)} \qquad \textbf{3-2}$$

Whereas E_l is the elastic modulus of the rigid layer and $E_s$the modulus of the elastomeric bulk phase. The Poission ratios are given with ν_l respectively ν_s, ε is the strain and ε_c the critical value for buckling and has to be exceeded.[19] Equation 3-1 shows that the wavelength of the wrinkles is only dependent on the thickness of the rigid layer and is adjustable over the plasma exposure time. This means that increased exposure time leads to thicker layers and therefore to longer wavelengths. The amplitude of the wrinkles follows also this trend but is also influenced by the strain (Equation 3-2)[14] This mathematical descriptions are only valid for uniaxial strain and deformations below the plastic deformation of the elastomer.[25] The precision of the predictions is also dependent on the accuracy of the determination of the elastic moduli and the Poisson ratios.

Wrinkled assisted assembly (WAA) of nanoparticles. The just discussed wrinkles can be used as templates for TASA. C. Lu *et al.* reported for the first time the direct

deposition of spherical polystyrene particles in wrinkles using dip coating. The authors dipped wrinkles oriented parallel to the withdrawal direction into the particle solution.[26] In this way linear particle chains along the grooves have been achieved. This technique is also transferable to other types of particles as presented in Ref. 27, where the authors showed that optical anisotropic substrates can be fabricated using this technique but with gold nano rods.

Further development of the WAA was made also in the Fery group, where the particle alignment was directly done on a glass substrate over confinement assembly (CA). In this case, a particle suspension was placed on a clean glass slide and confined between the planar glass surface and the sinusoidal wrinkled PDMS stripe. After solvent evaporation, the particles remain in the linear fashion of the wrinkles. The patterning can be controlled over the particle concentration. Low volume particle fraction give single lines, high volume fractions result in pyramidal like 3D structures.[28]

Colloids can also be deposited *via* spin coating into to grooves of the wrinkles and transferred to substrates with contact printing.[29] However printing particles out off the wrinkles is limited to the ratio between the depth of the wrinkle and the height of the particles. It is necessary that the particle height exceed the depth of the grooves of wrinkles. This limitation can be overcome by adding a wet transfer step and is discussed in detail in Chapter 4 were the so-called "spin release" (SR) plays a central role. In this work, silver and silica-core/PNIPAM-shell particles were used for surface patterning. This technique was also applied to the surface structuring with gold-stars/PNIPAM-shell particles of Chapter 5. If the target substrate is prestructured before particle transfer, more complex patterns can be achieved. This is presented in Ref. 30, where a glass slide was modified with μCP to generate hydrophilic/hydrophobic contrasts with subsequent particle transfer over SR.

3.2 Plasmonic nanoparticles

This chapter focuses on the basics of plasmonic nanoparticles. In the first part, the optical phenomenon of the plasmon resonance and their physical background will be briefly discussed. Subsequently an introduction in manipulation of these optical properties will be given.

3.2.1 *Plasmon resonances of metallic nanoparticles*

Metal nanoparticles exhibit special properties compared to their properties in bulk, due to their small sizes. For example, gold and silver NPs in the size regime of five to several 100 nm show special optical properties in the frequency range of visible light.[31, 32] These optical properties can be detected as colors and result from of the interaction of electromagnetic waves with the conduction band electrons of the metallic particle. The wave, this is the corresponding electric field, initiates a displacement of these electrons away from the positive atomic cores toward the particle surface, which yields a polarization at the particle surface (see Figure 3-4). The electron displacement is compensated by the restoring Coulomb forces of the positively charged atomic cores. This results in an oscillating dipole and is induced by the electric field and can be described by the dipole momentum $\mathbf{p}$ and the polarizability α:

$$\mathbf{p} = \alpha \epsilon_0 \epsilon_d \mathbf{E}_0 \qquad \textbf{3-3}$$

with

$$\alpha = 4\pi r^3 \frac{\epsilon_m - \epsilon_d}{\epsilon_m + 2\epsilon_d} \qquad \textbf{3-4}$$

Whereas ϵ_0 is the dielectric constant of the vacuum, ϵ_d of the medium, ϵ_m of the metallic particle, r the radius of the NP and $\mathbf{E}_0$ is the external electric field. It is important to keep in mind that the dielectric constant of a metal is a complex quantity and varies over the frequency ω. Damping, which the surface electron experience during their oscillations are incorporated in the imaginary part of ϵ_m. This frequency dependent dielectric constant $\epsilon_m(\omega)$ is consolidated in the Drude model:

$$\epsilon_m = 1 - \frac{\omega_p^2}{\omega^2 + i\gamma\omega} \qquad \textbf{3-5}$$

with the plasma frequency ω_p and the electron collision frequency γ within the crystal lattice.

The polarization of a metallic sphere is resonantly enhanced if the term $\epsilon_m + 2\epsilon_d$ of Equation 3-4 is close to zero, hence polarizability is maximal. That means the dielectric constants of the metal has to fulfill $-\epsilon_m = 2\epsilon_d$.[32-34]

Equation 3-3 is just valid for particles smaller than the excitation wavelength. If the particle size is increased to dimensions in the range of the wavelength of the incoming light higher modes like quadrupole or octapole modes have to be taken into account.[33, 35]

The described dipole resonance can be detected as the so-called localized surface plasmon resonance (LSPR). The electric field induced by the plasmon oscillations at the LSPR frequency leads to an enhanced near-field in close proximity of the particle surface.[34] The resonance itself depends on different factors like size, shape, material of the NP, and on the surrounding environment.[36, 37] These factors will be discussed in more detail in section 3.2.2 and 3.2.3.

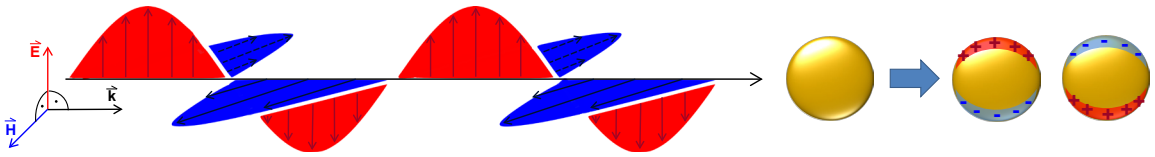

Figure 3-4 Schematic drawing of an incoming electromagnetic wave interacting with a gold NP and the following polarization of the surface electrons. The polarization of the surface electrons leads to an oscillating dipole, which is in phase with the electric field of the incoming light. (Not drawn to scale) Adapted with permission from L. M. Liz-Marzán, *Langmuir*, **2006**, 22, 32-41. Copyright 2006 American Chemical Society. Ref. 38

The LSPR phenomenon for spheroids is mathematically described by the Mie-theory using Maxwell´s equations under the right boundary conditions.[39] The exact description is not scope of this thesis and the reader is referred to the known textbooks given in Ref. 34, 40. To investigate the optical properties of gold nanospheres UV-Vis spectroscopy is commonly applied. The measured extinction (or absorbance) corresponds to the cross-section σ_{ext} of the particles. The extinction cross-section is the sum of the scattering σ_{scat} and absorption σ_{abs} cross-section:

$$\sigma_{ext} = \sigma_{sact} + \sigma_{abs} \qquad \textbf{3-6}$$

and

$$\sigma_{scat} = \frac{k^4}{6\pi}|\alpha|^2 = \frac{8\pi}{3}k^4 r^6 \left|\frac{\epsilon_m - \epsilon_d}{\epsilon_m + 2\epsilon_d}\right|^2 \qquad \textbf{3-7}$$

$$\sigma_{abs} = k\mathrm{Im}[r] = 4\pi k r^3 \mathrm{Im}\left|\frac{\epsilon_m - \epsilon_d}{\epsilon_m + 2\epsilon_d}\right| \qquad \textbf{3-8}$$

with the polarizability α and $k = 2\pi/\lambda$.[33] Equation 3-7 and 3-8 show clearly that the LSPR position depends on the polarizability and on the material of the nanoparticle. Therefore, the LSPR positions of different metals are located at different wavelengths and are size and shape depended.

3.2.2 *Controlling the LSPR via the intrinsic properties of nanoparticles*

As mentioned in the previous section, we will now discuss the intrinsic properties of the plasmonic particles. The light induced displacement of the surface electrons of the plasmonic nanoparticle strongly depends on its polarizability and size. If the particle diameter is increased, the electrons can be displaced easier so less excitation energy is needed to induce the oscillating dipole. This results in a red shift of the LSPR in the spectrum.[31-33, 35, 37, 38, 41, 42]

But not only the size also the shape of particle influences the polarizability and therefore the form and position of the LSPR.[43] Considering a rod-shaped particle, one will find two LSPR peaks - the so - called longitudinal and transversal LSPR peaks. This occurs, due to the anisotropic shape. The electrons can be displaced alongside the long (longitudinal) and short (transversal) axis of the rod.[38,44] Other particle geometries can also be obtained by wet chemical approaches, for example: dodecahedra,[45] cubes,[46] stars,[47] triangles,[48] dumbbells,[49] and nano shurikens.[50] Each of this examples show its own characteristic LSPR in the sense of shape, features and position in the spectral range.[32, 37, 51]

As visible from Equation 3-3, the polarizability also depends on the kind of metal as described by the dielectric constant ϵ_m. This means, that a silver sphere with a diameter of 48 nm shows a LSPR at 440 nm,[35] which is blue-shifted compared to a gold sphere with the same diameter (LSPR at 533 nm[42]).[52] This circumstance can be utilized for further tuning the optical properties of the particles. Depositing a silver layer on gold changes the spectra. Dependent on the thickness of the silver layer, the LSPR of gold can be continuously blue shifted. Increasing the silver layer further leads to a mixed gold and silver spectrum with features of both species. Additional silver deposition shields the gold signal completely and the silver characteristics dominate the optical properties.[53,54] Also gold and silver NP alloys can be synthesized,[38, 55] or strongly catalytic active metals like platinum[56] or palladium[57] can be grown on the plasmonic NPs. Platinum or palladium itself do not show a LSPR in the UV-Vis range but their presence

alter the refractive index in the close vicinity of the plasmonic particle and therefore it`s optical response. This is also the fact if a dielectric material like silica[58, 59] is grown on the plasmonic NPs. Reference 60 and 61 give a good overview of manifold synthesis and combinations of core/shell particles which are realized so far. The latest core/shell particles are examples, how plasmonic properties can be altered not only by manipulating the gold or silver colloid itself, but by extrinsic factors like the surrounding refractive index. The control of plasmonic properties using external tools will be scope of the next section.

3.2.3 *Controlling plasmonic properties via external stimuli*

We discussed already how the optical properties of the plasmonic NPs could be altered by manipulating the particle itself by changing its size, geometry, and material. Another tool to control the LSPR is the coupling behavior of the particles. If two plasmonic colloids are brought closer together than 2.5 times their diameter,[62] the surface electrons start to interact with each other. This interaction means that one particle feels the electric field $\boldsymbol{E}_0$ of the incident light and the near field $\boldsymbol{E}_{near}$ of the neighboring particle. Thus the plasmon oscillations of the individual particles are coupled and the following modulation of the electric field introduce a shift in the $LSPR_{max}$ position of the ensemble.[52] This shift is dependent on the polarization of the incident light.[27,63] Considering a dimer of gold spheres, the polarization can be set parallel to the inter particle axis or perpendicular. The first polarization leads to a red shift of the LSPR, the second case shifts the LSPR slightly into the blue, with respect to the plasmon resonance of an individual sphere. The coupling strength is depending on the number of neighboring particles and the inter particle distance. In coupled plasmonic structures, the local field is strongly enhanced in between the contributing particles. So-called "hot spots" are formed.[64] This can be used for sensing applications and will be discussed in section 3.2.4. As mentioned above coupling takes place at distances smaller 2.5 times the diameter and increases exponentially with decreasing spacing. This universal scaling behavior is independent of particle size, shape or metal and is well known as the so-called "plasmon ruler". This general trend is shown in Figure 3-5. Jain P. K. *et al.* simulated the LSPR shifts of gold discs of different diameters and decreasing inter particle distances. All LSPR shifts (normalized to the LSPR position of an individual disc) follow this exponential power law, which represents the increasing coupling

strength for reduced gap sizes.[65] Nevertheless, the LSPR changes drastically if the plasmonic colloids a brought into contact, due to quantum effects.[66]

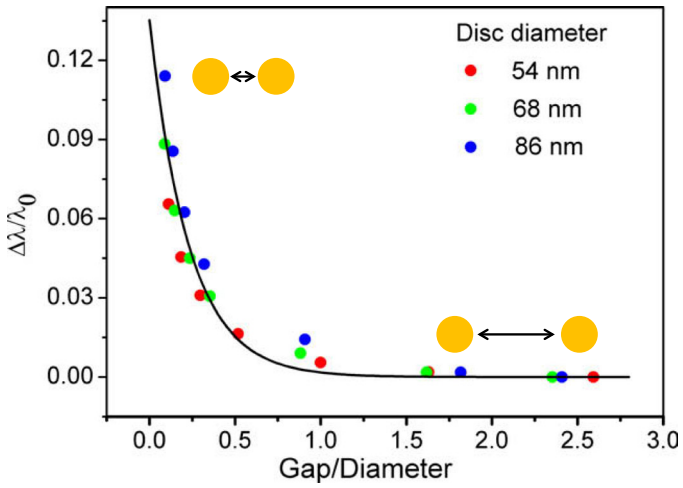

Figure 3-5 Simulation of near field LSPR frequency shifts of gold discs (normalized by $LSPR_{max}$ of an isolated disc) for three different diameters with increasing inter disc distance under polarized light. The polarization is set parallel to the inter particle axis. The LSPR shifts represent the inter particle coupling strength. The coupling strength decreases exponentially regardless of the disc diameter, which leads to the so called "plasmon ruler". "Reprinted and adapted with permission from P. K. Jain, W. Huang and M. A. El-Sayed, Nano Letters, **2007**, 7, 2080-2088. Copyright 2007 American Chemical Society." Ref. 65

Another influence on the position of the LSPR frequency is predicted by Equation 3-3. The dielectric constant ϵ_d of the surrounding medium influences the polarizability of the surface electrons of the NP and hence the resonance momentum of the oscillating dipole. This results in a refractive index sensitivity of the LSPR.[38, 67] Heo C.-J. *et al.* showed with their lithographically fabricated gold nano-forest, that the reflectance color of the arrays can be tuned from red over green into blue by increasing the refractive index n of the applied solvents (see Figure 3-6).[68] In general the LSPR shifts to higher wavelength by increasing n and *vice versa*.[69] This macroscopic color effect is not the single benefit, which can be drawn out of this sensitivity. Under the right conditions single molecule detection is possible. If a molecule attaches to the surface of a plasmonic NP it changes the average refractive index in the near field of the particle and therefore the position of the LSPR frequency.[70]

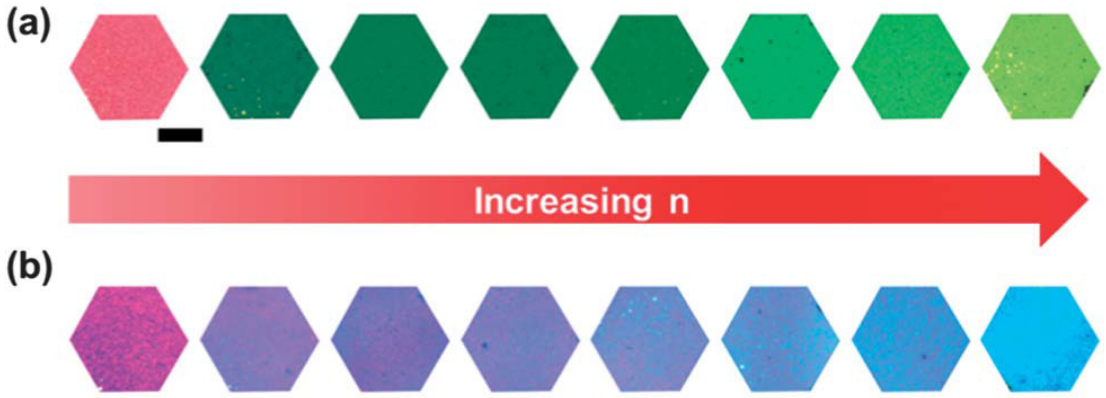

Figure 3-6 Color change of a lithographically fabricated gold nano-forest with increasing refractive index, due to different solvents. (a) and (b) show the results for different nano-forest geometries. Reproduced from Ref. 68 with permission from The Royal Society of Chemistry.

In addition, the deposition of plasmonic NPs to substrates or encapsulation in dielectric silica shells[58, 60] or polymers like poly(N-isopropylacrylamide) (PNIPAM)[71-73] alter their optical response. That the deposition of Au-PNIPAM core/shell-particles on glass substrates can alter the optical response even further will be scope of Chapter 6.

3.2.4 *Applications for plasmonic nanoparticles*

The last sections demonstrated how optical properties of plasmonic colloids could be changed or altered, due to external factors. This toolkit makes plasmon NPs attractive for sensing applications. A prominent example in this context is the "surface enhanced Raman spectroscopy" (SERS). Since Chapter 5 is also about SERS this sensing technique should be explained in more detail. Not only sensing applications are in the focus of the scientist, but also wave guiding or performance enhancement of photovoltaic devices.

Surface enhanced Raman spectroscopy is used for chemical and biological molecule detection. The detection is based on the inelastic light scattering of molecules in the vicinity of plasmonic materials. During scattering, a photon with the frequency ω_{inc} interacts with the molecule and excites vibrational and rotational states. The molecule itself emits thereupon a photon with the Raman shifted frequency ω_{em}. Compared to absorptive processes the emission of the photon is rapid and the direction of the wave vector is changed. Therefore, one calls the emitted photon the scattered photon. The frequency difference $\omega_{inc} - \omega_{em}$ hence the energy difference of the light can be detected and is characteristic for each molecule. This process can also be considered as a dipole oscillation similar to the theory of surface plasmon of section 3.2.1. The incoming light induces the dipole in the molecule, which emits the light. The intensity of the emitted

light is dependent on the polarizability of the molecule. Important for the following consideration are the Raman polarizability α_R and the Raman dipole p_R. Unfortunately, the Raman polarizability is small, hence scattering effects are inherently weak and the detection is difficult.[74-76] Therefore, the Raman signal has to be enhanced. This is done by using plasmonic materials, which can be gold or silver particle in solution, deposited to surfaces, or lithographically fabricated substrates. As already discussed, the intensity of the near field $\mathbf{E}_{near}$ of coupling metallic particles can be much higher than $\boldsymbol{E}_0$. This is of course just true, if the incoming light has the right excitation frequency for the plasmonic NP. This local field enhancement, the so called "hot spots", excite the Raman dipole oscillation with a higher magnitude than $\mathbf{E}_0$. Therefore, the emitted energy is higher and the Raman signal stronger. The enhancement of the signal depends for example on: the local field enhancement, the distance between the analyte and the metal hot spots (which should be small), the Raman polarizability of the NP, the energy of the used light source, and the excitation overlap of light and LSPR.[76]

The enhancement of the signal is given by the enhancement factor EF calculated by $\left(\frac{\boldsymbol{E}_{near,hot}}{\boldsymbol{E}_0}\right)^4$.[74] The EF lies typically in the range of 10^{10} or 10^{11} and is theoretical predicted even up to 10^{14}.[77, 78]

SERS instruments find application in scientific laboratories but also in forensics, pharmaceutics, food industry and many more. R. Mukhopadhyay gives an impressive overview of instruments and their applications in his product review article.[79] Besides these commercial available instruments, a lot of fundamental research is in progress. The reader is referred to recently published review articles for further information.[74, 77, 80-82]

The LSPR sensitivity regarding the dielectric environment can be directly utilized for **refractive index sensing**. This was shown by J. J. Mock *et al.* for silver particles, by A. Steinbrück *et al.* for gold-core/silver-shell particles or as presented in Figure 3-6 for the nano-forest. Changes in the refractive index surroundings can be caused by chemical reactions, appearance of different gases, or adsorbed molecule. Nevertheless, not only the changes of the environment can be detected also the plasmonic particle itself can be altered during reactions as shown by H. Jang and D-H. Min. They used Ag-Au alloy particles to monitor the presence of glucose in human blood or urine. A mixture of the alloy particles and the enzyme glucoseoxidase was added to the blood and urine. If

glucose was present, the enzymatic reaction between glucose and the enzyme produces H_2O_2 as a byproduct, which in turn etches the silver of the alloy particle. This results in a porous gold sphere with a different LSPR than for the alloy particle. Shifts of up to 180 nm have been achieved.[83]

Another route for monitoring a reaction *via* LSPR shifts is the selective aggregation of plasmonic NPs. The gold or silver surface is functionalized with enzymes or proteins that can bind to specific target analytes. The appearance of this analyte can act as a cross linker between the NPs, triggering the aggregation and inducing the LSPR shift, due to inter particle coupling.[84] Bimolecular sensors can be fabricated over a wide range, because functionalization with bio receptors is straightforward. In particular if the receptors carry a free thiol group. Thiols have an affinity towards gold and bind strongly to it. Such sensors can also be fabricated on chips, which increases their field of application further.[85]

Plasmonic systems are not only useful for sensing applications, but also for **wave guiding**. This is in the scope of the scientist, because data transfer *via* light is appealing for new fast types of computer chips. To transport information with light the beam has to be confined and sent along a path. Normal optical fibers are limited in their down scaling, due to the diffraction limit that is roughly $\lambda/2$. Plasmonic substrates are not limited in such ways.[86] One of the first and rather simple setups for long range plasmon polariton wave propagation was reported by E. Lisicka-Shrzek, where a metal stripe was sandwich between two insulators.[87] Meanwhile S. P. Burgos *et al.* showed that the light waves can also be guided along a grid using v-groove channels milled into a layer of gold.[88] Another access to plasmonic wave guides is the usage of plasmonic particles in coupling distance. This was reported by Atwater, where the authors used chains of gold and silver NPs.[89,90] Among lithographical generated structures also bottom up approaches are in the focus of scientist. So showed R. M Dickson *et al.* the coupling of photons into the plasmon mode of silver and gold nanowires.[91] And Link *et al.* showed the propagation of surface plasmon polaritons in silver particle chains around a sharp corner of 90°.[92]

Another promising utilization of plasmonic NPs is the implementation in **photovoltaic devices**. P. Reinicke *et al.* showed that embedding Ag or Au NPs into a layer of the organic hole conductor Spiro-OMeTAD of a photovoltaic device can generate a photo current.[93] There are numerous types of devices, for instance: dye-sensitized,[94,95] organic,[96,97] or perovskite[98,99] solar cells. Depending on the structure and configuration of such a device, the role of the plasmonic colloids can be different. On the one hand they can be used as backscatterer, which would extend the retention period of the photons. On the other hand they can serve as additional light absorbers. For example to absorb light in the spectral range where the unmodified device has a lack. This is feasible, due to the LSPR manipulation over the particle material, size, geometry and over deposition patterning. The interested reader is referred to the recent review article of Ref. [100] for further information of plasmonic structures in photovoltaic systems.

3.3 Inorganic core/soft PNIPAM shell particles

This section will introduce hard-core/soft-shell composite materials. In particularly hard-core/soft-polymer shell colloids. The core is always an inorganic material that can be silica, gold or silver. The soft shell is always PNIPAM a stimuli responsive micro gel. The synthesis of such hybrid NPs can be found in Ref. 71, 101, and 102, but is similar for all named core/shell systems and is schematically presented in Scheme 3-3d. The surface of the previously synthesized cores is modified with a functional molecule. This molecule has to contain two functional groups (Scheme 3-3a). One, which has to interact with the surface of the inorganic core, and the second that provides functionality, namely a double bond, to allow the emulsion polymerization of *N*-isopropylacrylamid (NIPAM) around the cores (Scheme 3-3b). The functionalization of the core is performed with methacryloxypropyltrimethoxysilane (MPS) in the case of silica particles and butenylamine hydrochloride (BA) in the case of gold and silver. Further, the presence of the crosslinker *N*,*N*-methylenebisacrylamide (BIS) is necessary to achieve a polymer network (Scheme 3-3d).

Scheme 3-3 (a) to (c) depicts the used molecules for the synthesis of hard inorganic-core/soft-PNIPAM shell particles. (d) depicts the schematic synthesis steps necessary to form such hybrid particles. The core is first functionalized with butenylammine hydrochlorid (for gold or silver) or with methacryloxypropyltrimethoxysilane (silica). Subsequent the shell is polymerized in an emulsion polymerization with *N*-isopropylacrylamide in the presence of the cross linker *N*,*N*-methylenebisacrylamide.

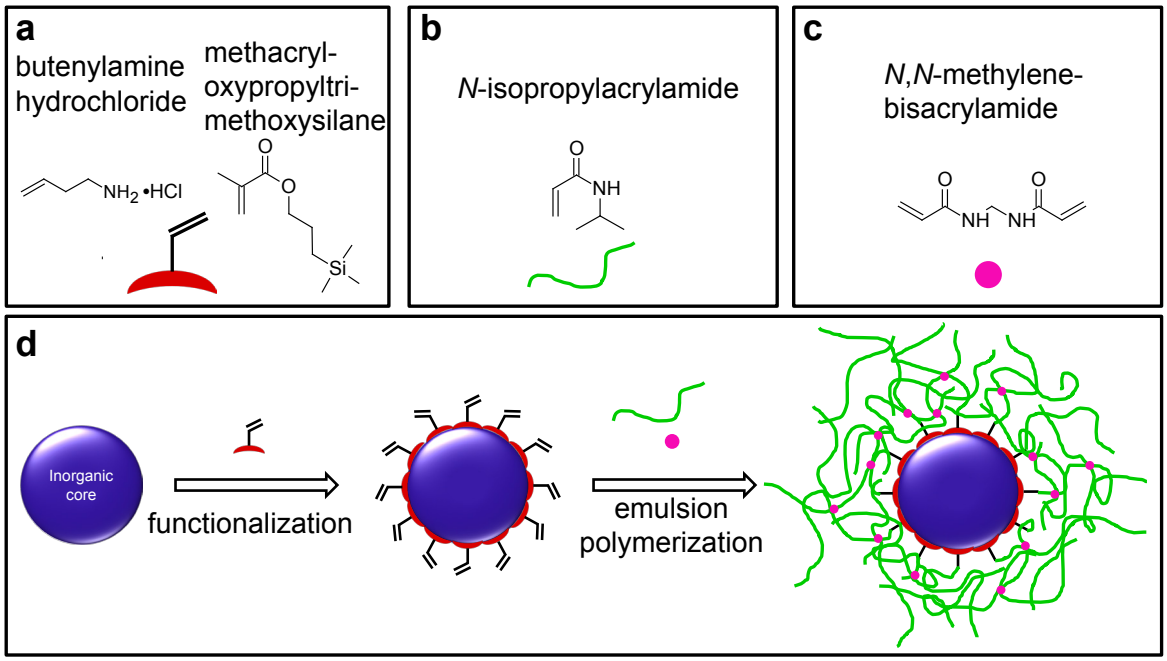

Such hybrid particles offer a multitude of advantages and possibilities for applications. On the first place, the shell acts as a stabilizer for the core, which is protected from

aggregation in this way. Furthermore, PNIPAM itself is thermo responsive. That means that the polymer reacts with a volume phase transition (VPT), if the temperature is changed - it reacts with shrinking or swelling.

The volume phase transition temperature (VPTT) describes the temperature where the VPT takes place or in other words the solubility of a polymer changes. Initially a polymer is insoluble in a solvent, but by increasing the temperature, the solubility can be increased. Once the VPTT is reached, the polymer passes the cloud point and is dissolved. That means the solvent interacts with the polymer chains and the network is fully swollen. This temperature is called the upper critical solution temperature. Normally the solubility increases with increasing temperature. However, this is different for polymer solutions. Increasing the temperature further, the polymer solution passes another cloud point, which means that the solvent changes from good to bad. This temperature is called the lower critical solution temperature (LCST).[103]

The solvent for PNIPAM at room temperature is water and the interaction forces between the polymer and water are very high, due hydrogen bonds between the amide groups and water. The network is fully swollen. The LCST for PNIPAM is 32 °C. Over this temperature, the hydrogen bonds break and the interaction forces between the polymer chains are higher than between polymer and water. This results in a shrinking of the network.[104] This process is reversible and can also be triggered by pH or ionic strength.[105]

Besides this responsibility, the polymer network acts as a spacer for the cores. This is important for long-term stability of suspensions or for particle assembly on surfaces. As described in section 3.2.3 distance control is essential in plasmonic systems and can be easily gained with core/shell particles.[41, 72, 102, 106, 107] In addition the PNIPAM shell is not rigid. The network is soft, compressible, and deformable in contrast to the inorganic core. The benefit of this property is used to break the symmetry in colloidal surface coatings and presented in Chapter 4 where core/shell NPs are transferred to glass substrates *via* SR. An additional aspect of the soft network is its permeability. Small molecules can diffuse through the meshes of the microgel and post-modifications of the cores are possible and in the scope of Chapter 5 and 6.

References

1. T. Itani and T. Kozawa, *Japanese Journal of Applied Physics*, 2013, **52**.
2. W. Chao, B. D. Harteneck, J. A. Liddle, E. H. Anderson and D. T. Attwood, *Nature*, 2005, **435**, 1210-1213.
3. S. J. Randolph, J. D. Fowlkes and P. D. Rack, *Critical Reviews in Solid State and Materials Sciences*, 2006, **31**, 55-89.
4. S. Reyntjens and R. Puers, *Journal of Micromechanics and Microengineering*, 2001, **11**, 287-300.
5. R. C. Y. Auyeung, H. Kim, S. A. Mathews and A. Pique, *Journal of Laser Micro Nanoengineering*, 2007, **2**, 21-25.
6. S. Roy, *Journal of Physics D-Applied Physics*, 2007, **40**, R413-R426.
7. R. G. Jones, C. K. Ober, P. Hodge, P. Kratochvil, G. Moad and M. Vert, *Pure Appl. Chem.*, 2013, **85**, 463-490.
8. O. D. Velev and A. M. Lenhoff, *Current Opinion in Colloid & Interface Science*, 2000, **5**, 56-63.
9. D. Schubert and T. Dunkel, *Mat Res Innovat*, 2003, **7**, 314-321.
10. O. D. Velev and S. Gupta, *Advanced Materials*, 2009, **21**, 1897-1905.
11. Y. N. Xia and G. M. Whitesides, *Angewandte Chemie-International Edition*, 1998, **37**, 550-575.
12. A. Perl, D. N. Reinhoudt and J. Huskens, *Advanced Materials*, 2009, **21**, 2257-2268.
13. S. A. Lange, V. Benes, D. P. Kern, J. K. H. Hörber and A. Bernard, *Analytical Chemistry*, 2004, **76**, 1641-1647.
14. M. Pretzl, A. Schweikart, C. Hanske, A. Chiche, U. Zettl, A. Horn, A. Boker and A. Fery, *Langmuir : the ACS journal of surfaces and colloids*, 2008, **24**, 12748-12753.
15. T.-H. Kim, K.-S. Cho, E. K. Lee, S. J. Lee, J. Chae, J. W. Kim, D. H. Kim, J.-Y. Kwon, G. Amaratunga, S. Y. Lee, B. L. Choi, Y. Kuk, J. M. Kim and K. Kim, *Nat Photon*, 2011, **5**, 176-182.
16. A. Rey, G. Billardon, E. Lortscher, K. Moth-Poulsen, N. Stuhr-Hansen, H. Wolf, T. Bjornholm, A. Stemmer and H. Riel, *Nanoscale*, 2013, **5**, 8680-8688.
17. C. Kuemin, R. Stutz, N. D. Spencer and H. Wolf, *Langmuir*, 2011, **27**, 6305-6310.
18. Y. Yin, Y. Lu, B. Gates and Y. Xia, *Journal of the American Chemical Society*, 2001, **123**, 8718-8729.
19. A. Schweikart and A. Fery, *Microchimica Acta*, 2009, **165**, 249-263.
20. N. Bowden, S. Brittain, A. G. Evans, J. W. Hutchinson and G. M. Whitesides, *Nature*, 1998, **393**, 146-149.
21. N. Bowden, W. T. S. Huck, K. E. Paul and G. M. Whitesides, *Applied Physics Letters*, 1999, **75**, 2557-2559.
22. D. Chen, J. Yoon, D. Chandra, A. J. Crosby and R. C. Hayward, *Journal of Polymer Science Part B: Polymer Physics*, 2014, **52**, 1441-1461.
23. V. V. Antić, M. P. Antić, M. N. Govedarica and P. R. Dvornić, *Journal of Polymer Science Part A: Polymer Chemistry*, 2007, **45**, 2246-2258.
24. B. Glatz and A. Fery, *submitted*, 2015.
25. D.-Y. Khang, J. A. Rogers and H. H. Lee, *Advanced Functional Materials*, 2009, **19**, 1526-1536.

26. C. Lu, H. Möhwald and A. Fery, *Soft Matter*, 2007, **3**, 1530-1536.
27. M. Tebbe, M. Mayer, B. A. Glatz, C. Hanske, P. T. Probst, M. B. Mueller, M. Karg, M. Chanana, T. Konig, C. Kuttner and A. Fery, *Faraday Discussions*, 2014.
28. A. Schweikart, A. Fortini, A. Wittemann, M. Schmidt and A. Fery, *Soft Matter*, 2010, **6**, 5860-5863.
29. S. Hiltl, M.-P. Schurings, A. Balaceanu, V. Mayorga, C. Liedel, A. Pich and A. Boker, *Soft Matter*, 2011, **7**, 8231-8238.
30. C. Hanske, M. B. Müller, V. Bieber, M. Tebbe, S. Jessl, A. Wittemann and A. Fery, *Langmuir*, 2012, **28**, 16745-16750.
31. N. Pazos-Perez, F. J. Garcia de Abajo, A. Fery and R. A. Alvarez-Puebla, *Langmuir*, 2012, **28**, 8909-8914.
32. W. A. Murray and W. L. Barnes, *Advanced Materials*, 2007, **19**, 3771-3782.
33. Y. Sonnefraud, A. Leen Koh, D. W. McComb and S. A. Maier, *Laser & Photonics Reviews*, 2012, **6**, 277-295.
34. U. Kreibig and M. Vollmer, *Optical properties of metal clusters*, Springer, 1995.
35. D. D. Evanoff and G. Chumanov, *ChemPhysChem*, 2005, **6**, 1221-1231.
36. F. Aussenegg and H. Ditlbacher, *Physik in unserer Zeit*, 2006, **37**, 220-226.
37. P. K. Jain, K. S. Lee, I. H. El-Sayed and M. A. El-Sayed, *Journal of Physical Chemistry B*, 2006, **110**, 7238-7248.
38. L. M. Liz-Marzán, *Langmuir*, 2005, **22**, 32-41.
39. G. Mie, *Annalen der Physik*, 1908, **330**, 377-445.
40. C. Bohren, F and D. Huffmann, R, eds., *Absorption and Scattering of Light by Small Particles*, Wiley, New York, 1983.
41. M. B. Müller, C. Kuttner, T. A. F. König, V. V. Tsukruk, S. Förster, M. Karg and A. Fery, *Acs Nano*, 2014, **8**, 9410-9421.
42. S. Link and M. A. El-Sayed, *Journal of Physical Chemistry B*, 1999, **103**, 4212-4217.
43. X. Lu, M. Rycenga, S. E. Skrabalak, B. Wiley and Y. Xia, *Annual Review of Physical Chemistry*, 2009, **60**, 167-192.
44. J. Pérez-Juste, I. Pastoriza-Santos, L. M. Liz-Marzán and P. Mulvaney, *Coordination Chemistry Reviews*, 2005, **249**, 1870-1901.
45. W. Niu, W. Zhang, S. Firdoz and X. Lu, *Journal of the American Chemical Society*, 2014, **136**, 3010-3012.
46. D. Y. Kim, S. H. Im, O. O. Park and Y. T. Lim, *CrystEngComm*, 2010, **12**, 116-121.
47. M. Müller, M. Tebbe, D. V. Andreeva, M. Karg, R. A. Alvarez Puebla, N. Pazos Perez and A. Fery, *Langmuir*, 2012, **28**, 9168-9173.
48. D. V. R. Kumar, A. A. Kulkarni and B. L. V. Prasad, *Colloids and Surfaces A: Physicochemical and Engineering Aspects*, 2013, **422**, 181-190.
49. M. Grzelczak, A. Sánchez-Iglesias, B. Rodríguez-González, R. Alvarez-Puebla, J. Pérez-Juste and L. M. Liz-Marzán, *Advanced Functional Materials*, 2008, **18**, 3780-3786.
50. J. Morla-Folch, L. Guerrini, N. Pazos-Perez, R. Arenal and R. A. Alvarez-Puebla, *ACS Photonics*, 2014, **1**, 1237-1244.
51. M. Rycenga, C. M. Cobley, J. Zeng, W. Li, C. H. Moran, Q. Zhang, D. Qin and Y. Xia, *Chemical Reviews*, 2011, **111**, 3669-3712.

52. P. K. Jain and M. A. El-Sayed, *Chemical Physics Letters*, 2010, **487**, 153-164.
53. A. Steinbruck, O. Stranik, A. Csaki and W. Fritzsche, *Anal. Bioanal. Chem.*, 2011, **401**, 1241-1249.
54. L. Lu, G. Burkey, I. Halaciuga and D. V. Goia, *Journal of Colloid and Interface Science*, 2013, **392**, 90-95.
55. S. Link, Z. L. Wang and M. A. El-Sayed, *The Journal of Physical Chemistry B*, 1999, **103**, 3529-3533.
56. H. Liu and J. Yang, *Journal of Materials Chemistry A*, 2014, **2**, 7075-7081.
57. Y. Mizukoshi, T. Fujimoto, Y. Nagata, R. Oshima and Y. Maeda, *The Journal of Physical Chemistry B*, 2000, **104**, 6028-6032.
58. T. Li, J. Moon, A. A. Morrone, J. J. Mecholsky, D. R. Talham and J. H. Adair, *Langmuir*, 1999, **15**, 4328-4334.
59. L. M. Liz-Marzán, M. Giersig and P. Mulvaney, *Langmuir*, 1996, **12**, 4329-4335.
60. S. Thatai, P. Khurana, J. Boken, S. Prasad and D. Kumar, *Microchemical Journal*, 2014, **116**, 62-76.
61. R. Ghosh Chaudhuri and S. Paria, *Chemical Reviews*, 2011, **112**, 2373-2433.
62. S. K. Ghosh and T. Pal, *Chemical Reviews*, 2007, **107**, 4797-4862.
63. C. Hanske, M. Tebbe, C. Kuttner, V. Bieber, V. V. Tsukruk, M. Chanana, T. A. F. König and A. Fery, *Nano Letters*, 2014, **14**, 6863-6871.
64. T. Vo-Dinh, Y. Liu, A. M. Fales, H. Ngo, H.-N. Wang, J. K. Register, H. Yuan, S. J. Norton and G. D. Griffin, *Wiley Interdisciplinary Reviews: Nanomedicine and Nanobiotechnology*, 2015, **7**, 17-33.
65. P. K. Jain, W. Huang and M. A. El-Sayed, *Nano Letters*, 2007, **7**, 2080-2088.
66. N. J. Halas, S. Lal, W.-S. Chang, S. Link and P. Nordlander, *Chemical Reviews*, 2011, **111**, 3913-3961.
67. P. Mulvaney, *Langmuir*, 1996, **12**, 788-800.
68. C.-J. Heo, H. C. Jeon, S. Y. Lee, S. G. Jang, S. Cho, Y. Choi and S.-M. Yang, *Journal of Materials Chemistry*, 2012, **22**, 13903-13907.
69. J. J. Mock, D. R. Smith and S. Schultz, *Nano Letters*, 2003, **3**, 485-491.
70. J. Zhao, A. Das, X. Zhang, G. C. Schatz, S. G. Sligar and R. P. Van Duyne, *Journal of the American Chemical Society*, 2006, **128**, 11004-11005.
71. M. Karg, S. Jaber, T. Hellweg and P. Mulvaney, *Langmuir*, 2011, **27**, 820-827.
72. J. Clara-Rahola, R. Contreras-Caceres, B. Sierra-Martin, A. Maldonado-Valdivia, M. Hund, A. Fery, T. Hellweg and A. Fernandez-Barbero, *Colloids and Surfaces A: Physicochemical and Engineering Aspects*, 2014, **463**, 18-27.
73. S. Carregal-Romero, N. J. Buurma, J. Perez-Juste, L. M. Liz-Marzan and P. Herves, *Chemistry of Materials*, 2010, **22**, 3051-3059.
74. S. Schlücker, *Angewandte Chemie International Edition*, 2014, **53**, 4756-4795.
75. E. C. Le Ru and P. G. Etchegoin, in *Principles of Surface-Enhanced Raman Spectroscopy*, eds. E. C. L. Ru and P. G. Etchegoin, Elsevier, Amsterdam, 2009, pp. 29-120.
76. E. C. Le Ru and P. G. Etchegoin, in *Principles of Surface-Enhanced Raman Spectroscopy*, eds. E. C. L. Ru and P. G. Etchegoin, Elsevier, Amsterdam, 2009, pp. 185-264.

77. D. Cialla, A. März, R. Böhme, F. Theil, K. Weber, M. Schmitt and J. Popp, *Anal. Bioanal. Chem.*, 2012, **403**, 27-54.
78. E. C. Le Ru, E. Blackie, M. Meyer and P. G. Etchegoin, *The Journal of Physical Chemistry C*, 2007, **111**, 13794-13803.
79. R. Mukhopadhyay, *Analytical Chemistry*, 2007, **79**, 3265-3270.
80. W. Xie and S. Schlucker, *Rep Prog Phys*, 2014, **77**, 0034-4885.
81. J. F. Betz, W. W. Yu, Y. Cheng, I. M. White and G. W. Rubloff, *Phys Chem Chem Phys*, 2014, **16**, 2224-2239.
82. B. Sharma, R. R. Frontiera, A.-I. Henry, E. Ringe and R. P. Van Duyne, *Materials Today*, 2012, **15**, 16-25.
83. H. Jang and D.-H. Min, *RSC Advances*, 2015.
84. W. Zhao, M. A. Brook and Y. Li, *ChemBioChem*, 2008, **9**, 2363-2371.
85. J. Cao, T. Sun and K. T. V. Grattan, *Sensors and Actuators B: Chemical*, 2014, **195**, 332-351.
86. S. Lal, S. Link and N. J. Halas, *Nat Photon*, 2007, **1**, 641-648.
87. R. Charbonneau, P. Berini, E. Berolo and E. Lisicka-Shrzek, *Opt. Lett.*, 2000, **25**, 844-846.
88. S. P. Burgos, H. W. Lee, E. Feigenbaum, R. M. Briggs and H. A. Atwater, *Nano Letters*, 2014, **14**, 3284-3292.
89. S. A. Maier, P. G. Kik and H. A. Atwater, *Applied Physics Letters*, 2002, **81**, 1714-1716.
90. S. A. Maier, P. G. Kik, H. A. Atwater, S. Meltzer, E. Harel, B. E. Koel and A. A. G. Requicha, *Nat Mater*, 2003, **2**, 229-232.
91. R. M. Dickson and L. A. Lyon, *The Journal of Physical Chemistry B*, 2000, **104**, 6095-6098.
92. D. Solis, A. Paul, J. Olson, L. S. Slaughter, P. Swanglap, W.-S. Chang and S. Link, *Nano Letters*, 2013, **13**, 4779-4784.
93. P. Reineck, G. P. Lee, D. Brick, M. Karg, P. Mulvaney and U. Bach, *Advanced Materials*, 2012, **24**, 4750-4755.
94. N. Sharifi, F. Tajabadi and N. Taghavinia, *ChemPhysChem*, 2014, **15**, 3902-3927.
95. H. Dong, Z. Wu, Y. Gao, A. El-Shafei, B. Jiao, Y. Dai and X. Hou, *Organic Electronics*, 2014, **15**, 1641-1649.
96. S. Günes, H. Neugebauer and N. S. Sariciftci, *Chemical Reviews*, 2007, **107**, 1324-1338.
97. Q. Gan, F. J. Bartoli and Z. H. Kafafi, *Advanced Materials*, 2013, **25**, 2385-2396.
98. H. S. Jung and N.-G. Park, *Small*, 2015, **11**, 10-25.
99. N. Chander, P. S. Chandrasekhar and V. K. Komarala, *RSC Advances*, 2014, **4**, 55658-55665.
100. M. Karg, T. A. F. König, M. Retsch, C. Stelling, P. M. Reichstein, T. Honold, M. Thelakkat and A. Fery, *Materials Today*, 2014.
101. M. Karg, I. Pastoriza-Santos, L. M. Liz-Marzan and T. Hellweg, *Chemphyschem*, 2006, **7**, 2298-2301.
102. M. Müller, M. Karg, A. Fortini, T. Hellweg and A. Fery, *Nanoscale*, 2012, **4**, 2491-2499.

103. M. D. Lechner, E. H. Nordmeier and K. Gehrke, in *Makromolekulare Chemie*, Birkhäuser Basel, 2010, ch. 4, pp. 171-343.
104. P. Robert, *Advances in Colloid and Interface Science*, 2000, **85**, 1-33.
105. M. Karg, I. Pastoriza-Santos, B. Rodriguez-González, R. von Klitzing, S. Wellert and T. Hellweg, *Langmuir*, 2008, **24**, 6300-6306.
106. M. Karg, S. Jaber, A. Morfa and P. Mulvaney, *Phys Chem Chem Phys*, 2011, **13**, 5576-5578.
107. N. Vogel, C. Fernández-López, J. Pérez-Juste, L. M. Liz-Marzán, K. Landfester and C. K. Weiss, *Langmuir*, 2012, **28**, 8985-8993.

4 Wrinkle-assisted linear assembly of hard-core/soft-shell particles: impact of the soft shell on the local structure

*Mareen Müller,[a] Matthias Karg,[b] Andrea Fortini,[c] Thomas Hellweg[d] and Andreas Fery[a]**

[a] Physical Chemistry II, University of Bayreuth, Universitätsstr. 30, 95447 Bayreuth, Germany

[b] Physical Chemistry I, University of Bayreuth, Universitätsstr. 30, 95447 Bayreuth, Germany

[c] Theoretical Physics, University of Bayreuth, Universitätsstr. 30, 95447 Bayreuth, Germany

[d] Physical Chemistry III, University of Bielefeld, Universitätsstr. 25, 33615 Bielefeld, Germany

* e-mail: andreas.fery@uni-bayreuth.de

Published in *Nanoscale* **2012**, 4, 2491-2499

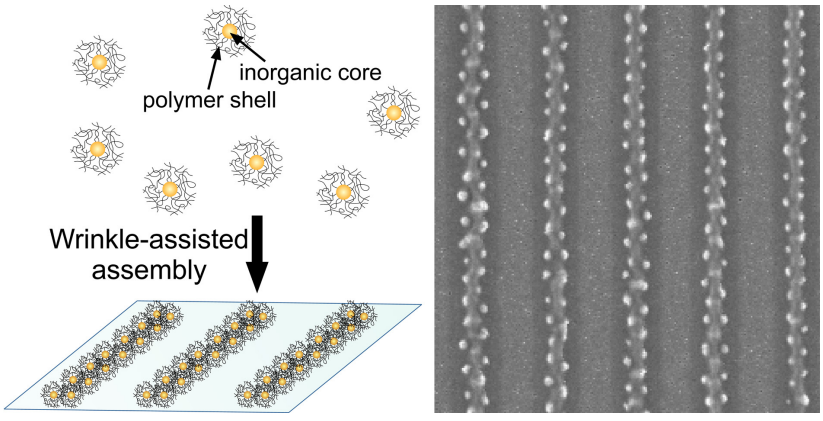

Abstract

This article addresses wrinkle-assisted assembly of core–shell particles with hard cores and soft poly-(N-isopropylacrylamide) shells. As core materials we chose silica as well as silver nanoparticles. The assembled structures show that the soft shells act as a separator between the inorganic cores. Anisotropic alignment is found on two length scales, macroscopically guided through the wrinkle structure and locally due to deformation of the polymer shell leading to smaller inter-core separations as compared to assembly on flat substrates without confinement. The structures were analysed by means of scanning electron microscopy. Radial distribution functions are shown, clearly highlighting the impact of confinement on nearest neighbour distances and symmetry. The observed ordering is directly compared to Monte-Carlo simulations for hard-core/soft-shell particles, showing that the observed symmetries are a consequence of the soft interaction potential and differ qualitatively from a hard-sphere situation. For the silver-poly-(N-isopropylacrylamide) particles, we show UV-Vis absorbance measurements revealing optical anisotropy of the generated structures due to plasmon coupling. Furthermore, the high degree of order of the assembled structures on macroscopic areas is demonstrated by laser diffraction effects.

4.1 Introduction

Ordering of nanoparticles into assemblies which are well-defined on the nanoscale and at the same time of macroscopic dimensions is one of the most pressing challenges in materials science for various reasons: if particles aggregate in a random fashion, often uncontrolled electronic coupling effects occur, which result at best in less defined electronic, optical or magnetic properties or—in worse cases—in a complete loss of the specific nanoparticle effects and a re-entrance of bulk material properties. Creating ordered nanoparticle structures is one means of avoiding such uncontrolled coupling. On the other hand, well defined assemblies may give rise to novel collective effects due to spatial periodicity like optical bandgaps. Finally, local coupling between nanoparticles can—if controlled by precise arrangements— provide an excellent means for controlling interactions with electromagnetic radiation like for example hot-spot formation,[1] plasmonic properties[2] or optical metamaterials effects.[3]

Still, many strategies which are well suited for ordering of colloidal particles of micron-dimensions fail for nanoscale particles, due to scaling of the underlying interactions.[4] Out of the ''nanoscale-compatible approaches'' template assisted selfassembly (TASA) offers a great potential for creating 1D, 2D and even 3D structures.[5, 6, 7, 8] Substrates that are topographically structured can guide surface assemblies of particles and—via colloidal epitaxy effects—even control three-dimensional colloidal crystal structures. However, as template dimensions have to be on the order of a few particle diameters to provide sufficient constraints for high fidelity, technological effort for TASA increases when particles approach diameters below the wavelength of visible light. Rather than conventional lithography, time and resource consuming techniques like electronbeam lithography,[9] extreme UV interference lithography,[10] focused ion beam milling[11] or nanoimprint-lithography[12] are necessary. We have recently introduced wrinkle-assisted selfassembly as a lithography-free alternative to classical TASA.[13] Wrinkles develop if an elastic material coated with a thin, hard layer is exposed to strain.[14] Permanently stable wrinkles can be achieved if the coating is applied in a strained state, such that wrinkles form upon relaxation. Wrinkles can, depending on the particular strain situation, show a variety of patterns/symmetries including parallel grooves, chevron topologies or spoke and target-like patterns.[15] They can reach periodicities as low as 200 nanometres and be replicated in a variety of materials.[16] In addition, topographical patterns can be translated into chemical ones by microcontact printing.[17, 18] Therefore both topographically and/or chemically structured templates can be created *without lithography*.

Our preliminary results demonstrate that the quality of particle ordering is sufficient to control even effects like hot-spot formation, which is known to be extremely sensitive to the interparticle distance.[1] Particle structures can be predicted using Monte-Carlo (MC) simulations.[19]

In this manuscript, we expand our approach for the first time from hard particles to particles consisting of a hard core and a soft gel-shell.[20] This core–shell architecture is of interest, because it provides a means of controlling inter-particle distances in the sub-optical wavelength regime, which is a prerequisite for controlling plasmonic coupling effects.[21, 22, 23, 24, 25, 26] Furthermore, numerous experiments, simulation and modelling results show dramatic differences in terms of phase behaviour, structure and colloidal stability between hard-core and hard-core/soft-shell systems.[20, 27, 28, 29, 30]

≥In the present manuscript, we focus on the impact of the particle's architecture on the resulting assembly symmetry. We show that particle assemblies templated from core–shell particles display novel symmetries as compared to hard-sphere systems studied previously.[19] In particular, we observe a massive reduction of inter-particle spacing in the wrinkles as compared to an unconfined situation. Monte-Carlo simulations are in good agreement with experiments indicating that the effects are indeed a consequence of the soft nature of inter-particle interactions. In addition, we provide first evidence that particle assemblies show local coupling resulting in polarisation dependent plasmonic properties.

4.2 Experimental

Materials

Polydimethylsiloxane (PDMS) was prepared by polymerisation of the monomer Sylgard 184 using the Sylgard 184 curing agent, from Dow Corning, USA. For the microgel synthesis the N-isopropylacrylamide (NIPAM; Aldrich, 97%), N,N 0-methylenebisacrylamide (BIS; Fluka, ≥99.5%), and potassium peroxodisulfate (PPS; Fluka, ≥99.0%) were used as received. Tetraethoxysilane (TEOS; Aldrich, ≥98.0%), methacryloxypropyltrimethoxysilane (MPS; Aldrich, 98%), ethanol (Scharlau, 96%), silver nitrate (Ajax Chemicals, 99.9%), D-(+)-glucose (Sigma-Aldrich, ACS reagent), ammonium hydroxide (Aldrich, ACS reagent, 28–30% in water), sodium hydroxide (ChemSupply, Analytical reagent), sodium dodecylsulfate (SDS; Ajax Laboratory Chemicals, Techn.), and butenylamine hydrochloride (BA; Aldrich, 97%) were used without further purification. Water was purified by a MilliQ system (Millipore).

4.2.1 *Silica–PNIPAM synthesis*

The synthesis of silica–PNIPAM core–shell particles was performed as reported elsewhere.[31] Briefly, silica nanoparticles of 35 and 100 nm in diameter were prepared by the well-known protocol by Stöber.[32] Prior to the growth of the polymer shell, the silica particle surface was functionalised with MPS. Finally, the functionalised silica nanoparticles were used as core particles in the polymerisation of NIPAM and BIS leading to core–shell particles with single silica cores and homogeneous PNIPAM shells.

4.2.2 *Ag–PNIPAM synthesis*

Silver nanoparticles of 90 nm in diameter were synthesised by reduction of silver nitrate in an aqueous glucose solution.[33] 5 mL of a freshly prepared 0.04 M ammonia solution were quickly added to 25 mL of a 2 mM $AgNO_3$ solution in a conical flask of 100 mL volume. The solutions were mixed by gentle shaking and then left aside for 30 minutes. Then, 20 mL of a 25 mM aqueous glucose solution were added followed by the quick addition of 0.9 mL NaOH solution (25 mM). Again, just gentle shaking of the flask was used to mix the reactants. Within the first minutes after the addition of NaOH, the dispersion turned yellow, became turbid and finally a strongly turbid, yellow-gray particle dispersion was obtained. After 48 hours most of the particles sedimented and the almost clear, colourless supernatant was removed carefully. The sediment was redispersed in 45 mL of water and 45 mL of a SDS solution (0.6 mM) were added under stirring with a magnetic stirrer. 20 minutes after the SDS addition, 15 mL of an aqueous BA solution (3 mM) were added under continuous stirring. The amine group of the BA has a strong affinity towards silver and the double bond of the alkyl chain is a reactive functionality for the following polymerisation step. 20 minutes after the addition of BA, the particle dispersion was kept in the dark for 48 hours without stirring. Again, the supernatant was removed leaving 1 mL of a concentrated dispersion of functionalised silver nanoparticles. The polymer coating of the silver particles was done by precipitation polymerisation of the monomer NIPAM and the cross-linker BIS in the presence of the functionalised silver particles. This protocol is based on the recipe we employed for polymer coating of gold nanoparticles published elsewhere.[34] Briefly, 45 mg NIPAM and 16 mg BIS were dissolved in 20 mL of water in a 50 mL three-neck round bottom flask equipped with a reflux condenser. The solution was degassed with nitrogen for 20 minutes and heated to 70 °C using an oil bath. Under continuous stirring with a magnetic stirrer, 0.9 mL of the functionalised Ag nanoparticles were added dropwise. 10 minutes after the addition of the Ag nanoparticles, the polymerisation was initiated by the quick injection of 0.5 mg potassium peroxodisulfate dissolved in 0.5 mL of water. The reaction was allowed to proceed for 2 hours at 70 °C. Finally, the dispersion was cooled down to room temperature. Cleaning of the particles was performed by repeated centrifugation (30 minutes at 2000 rpm) and redispersion in water. Three centrifugation/ redispersion steps were performed. The resulting particle dispersion is strongly turbid with a deep yellow colour.

4.2.3 *Preparation of wrinkles*

The PDMS for the wrinkled substrates was prepared by polymerising the monomer and the curing agent in a weight ratio of 10 : 1. The mixture was cast into a clean and plane glass dish of 2 mm height. After pre-polymerisation overnight, the PDMS was cured for 5 h at 80 °C. The cross-linked PDMS was cut into pieces of 0.6 x 3 cm^2. To gain the wrinkled surface, the PDMS strip was fixed in a custom made stretching apparatus and was stretched 25% of its primary length. The stretched strips were exposed to oxygen plasma for 600 s or 300 s at 0.2 mbar (Plasma Activate Flecto 10 USB) with a power of 100 W. After 5 min of cooling, the stripes were allowed to relax.

4.2.4 *Particle assembly*

20 mL of the aqueous particle suspension were placed on top of the wrinkled substrates, which were hydrophilised directly before use for 15 s in oxygen plasma to gain good wetting of the surface. The particles were spin coated into the cavities at 2000 rpm for 60 s (Model P6700 from Specialty Coating Systems INC). The coated strip was placed onto a drop of MilliQ water (10 µL) on a cleaned glass slide without external pressure. The slide was cleaned by using standard RCA-1 solution of $NH_4OH/H_2O_2/H_2O$ in the ratio 1 : 1 : 5 at 80 °C.[35] After drying for 3 h, the PDMS was carefully removed.

4.2.5 *Characterisation*

The wrinkles were characterised by AFM (Multimode AFM Veeco Instruments Inc.) using tips from Olympus (296–340 kHz, 41–62 N m^{-1}) in tapping mode. The wavelengths and amplitudes were obtained by analysing the height images. The wavelengths of the patterned structures were calculated from SEM images by using the software ImageJ (NIH USA) with the ''radial profile'' plug-in. The SEM measurements were performed with a LEO 1530 VP Gemini from Zeiss operating at 2 kV. The samples were sputtered with 2 nm Pt layer and the working distance was kept at 4 mm. Transmission electron microscopy (TEM) was performed on an FEI TF 20 operated with an acceleration voltage of 200 kV. The samples were prepared on carbon-coated copper grids (300 mesh) by drop casting from aqueous dispersion. UV-Vis absorbance spectra were recorded with an Agilent 8453 spectrophotometer. Measurements were done at 25 °C controlled by using a circulated water bath. DLS measurements were done on a classical goniometer setup (ALV, Langen, Germany) with a HeNe laser (λ = 632.8 nm). Intensity–time autocorrelation functions were recorded at various scattering angles using a multiple τ digital correlator (ALV-5000/E). The temperature of the sample was controlled by a

circulated water bath and a toluene refractive index matching/temperature bath. The data were analysed using inverse Laplace transformation through the CONTIN algorithm by S. Provencher.

4.3 Results and discussion

4.3.1 *Formation and characterisation of used wrinkles*

The wrinkled surface was formed by stretching of polydimethylsiloxane (PDMS), a silicone elastomer, and oxygen exposure in the elongated state. During the oxidation a hard silica layer was formed on the PDMS surface. After relaxation stable and uniform wrinkles were obtained. Wavelength and amplitude can be controlled by the plasma exposure time. Longer times lead to thicker silica layers and therefore to longer wavelengths and amplitudes.[14] The wrinkles were characterised using atomic force microscopy (AFM). The found wavelengths and amplitudes for 600 s and 300 s exposure in plasma are summarised in Table 4-1. The error of the wavelength and amplitude is determined by analysing cross-sections of the AFM height images on three different spots of the substrate, and an additional error contribution of the tip diameter.

4.3.2 *Surface patterning via ''Spin-Release''*

For surface patterning with hard-core/soft-shell particles the method of ''Spin-Release'' (SR) was used. This procedure combines stamping and confinement assembly as illustrated schematically in Fig 4-1.[36, 37] For surface structuring the wrinkled PDMS was first hydrophilised in an oxygen plasma to gain a wettable surface. Then, the substrate was placed on a spin coater and a small amount of the core–shell particle suspension was deposited on top of the wrinkled substrate. During the spinning the cavities were filled with the particles and excessive suspension was cast away. In the next step, the filled wrinkles were brought in contact with a cleaned glass slide covered with a water droplet. No external pressure was applied. Glass and wrinkles stayed in contact until the water was evaporated. Then, the PDMS strip was carefully lifted off. The achieved structures were characterised with SEM and are presented in Fig 4-2A–D and Fig 4-5B–E.

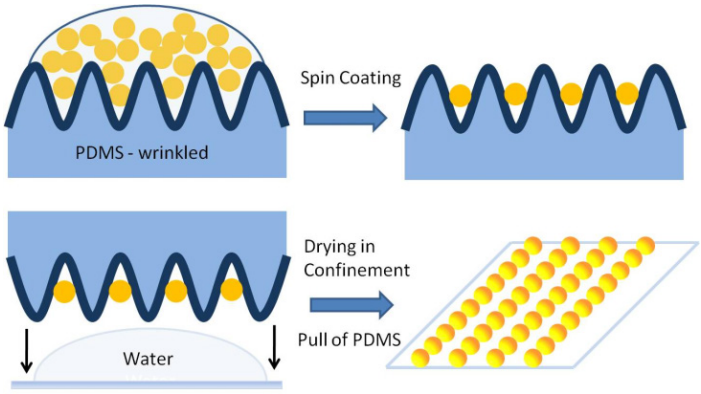

Fig 4-1 Schematic depiction of the "Spin-Release" (SR) process.

4.3.3 *Spin-Release with silica–PNIPAM core–shell particles*

In order to study the assembly of hard-core/soft-shell particles with different core sizes, we prepared silica–PNIPAM core–shell systems with two different sizes of the silica cores (35 and 100 nm in diameter). The overall diameter of both systems is approx. 500 nm in the swollen state as determined by DLS at 20 °C. A detailed analysis of these particles can be found elsewhere.[31, 38] These particles were assembled in a linear fashion using the SR approach with PDMS templates of two different wavelengths. The results are presented in Fig 4-2 and Table 4-1.

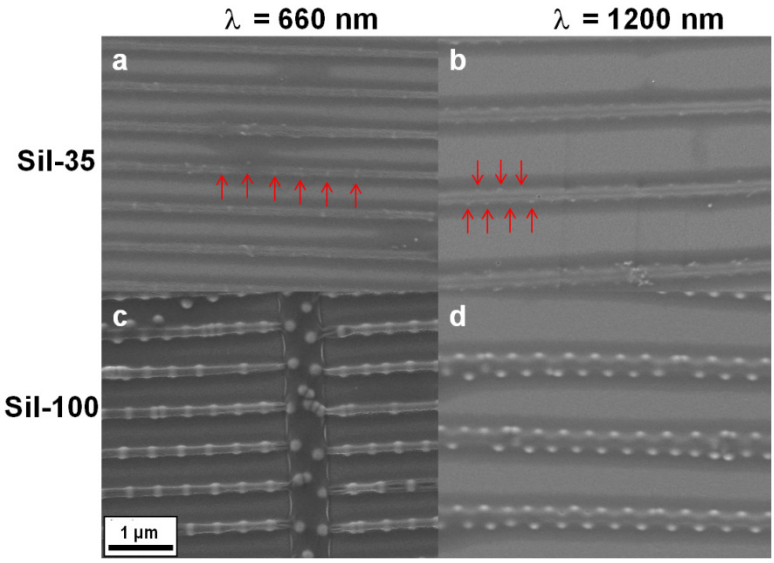

Fig 4-2 Results of SR for two Silica-PNIPAM core-shell particles using PDMS templates with two different wavelengths (660 nm for (a) and (c); 1200 nm for (b) and (d). The core diameter for Sil-35 is 35 nm, presented in image (a) and (b). The core diameter for Sil-100 is 100 nm, presented in image (c) and (d). The red arrows in (a) and (b) indicate the position of the silica cores for the Sil-35 sample. For a template wavelength of 660 nm, single particle lines are formed. For a template wavelength of 1200 nm, 2D zigzag lines are observed for both samples.

Table 4-1 Summary of wavelengths, amplitudes, core-to-core distances and wavelengths of patterns.

	Wavelength of PDMS / nm	Amplitude of PDMS / nm	Centre-to-centre distance / nm	Pattern wavelength / nm
Sil-100 λ_{660}	667 ± 30	56 ± 14	408 ± 10	657 ± 18
Sil-100 λ_{1200}	1175 ± 43	108 ± 16	314 ± 25	1164 ± 74
Sil- 35 λ_{660}	605 ± 47	63 ± 15	-	-
Sil-35 λ_{1200}	1170 ± 68	107 ± 19	-	-
Ag-A	-	-	433 ± 21	-
Ag-B	1323 ± 55	134 ± 16	276 ± 13	1311 ± 11
Ag-C	1181 ± 49	125 ± 17	212 ± 42	1167 ± 53

The SEM images in Fig 4-2 nicely show that both core–shell systems can be assembled in a linear fashion. Whereas the silica cores of the Sil-100 sample are easily visible in Fig 4-2c and d, the comparably small cores of sample Sil-35 are rather hard to identify (Fig 4-2a and b). Therefore, we highlighted the position of some of the cores of the Sil-35 sample by red arrows in Fig 4-2 and b. For a wrinkle wavelength of 660 nm, which is close to the diameter of the core–shell particles in the swollen state, we observe quasi-1D linear particle assemblies with well separated silica cores due to the presence of the PNIPAM shell. For a template wavelength larger than the particle diameter, 2D zigzag lines are formed (Fig 4-2b and d). This is due to the fact that the wrinkle cavities are much larger compared to the template with only 660 nm in wavelength. To determine the nearest neighbour distance, radial distribution functions (RDFs) were calculated. The values for the centre-to-centre distance and the wavelength of the patterns are listed in Table 4-1. These values are average values of ten independent RDFs for each substrate for at least 250 particles. The RDF, also-called pair correlation function, describes how the particle density changes with distance from one specific particle. Due to the poor visibility of the rather small silica cores of the Sil-35 sample, RDFs were only generated for the Sil-100 sample. One can see that for both wrinkles, the particle distance is significantly smaller than the particle diameter in the swollen state. In single particle lines (Sil-100 λ_{600}) the centre-to-centre distance is 408 ± 10 nm. In contrast the centre-to-centre distance in 2D zigzag lines (Sil-100 λ_{1200}) is smaller (314 ± 25 nm). This can be attributed to a higher particle compression under confinement during the SR process. The SEM images in Fig 4-2 also show that the polymer shells form a continuous connection between the silica cores. This is due to the fact that the polymer shells collapse during spin coating into the wrinkles. The transfer from PDMS to the glass is

done under aqueous conditions and hence the PNIPAM shells swell. Therefore, neighbouring particles compress each other, leading to an interdigitation of the dangling ends of their polymer coronas. The presented SR technique allows preparation of large particle arrays which can be transferred to other substrates very easily, which is necessary if optical measurements should be done. The advantage of the printing step during SR is that the pre-arrangement in wrinkles leads to homogeneous arrays and geometries. Due to the water droplet, the particles were washed out from the wrinkles in confined conditions and no pressure is necessary for transfer. This technique represents a versatile tool for surface patterning with re-dispersible particles such as the presented hard-core/soft-shell systems. The photographs of the PDMS stamp and the particle assembly on a glass substrate shown in Fig 4-3 demonstrate that assemblies over large areas can be realised utilising the SR approach. The strong iridescence visible in both photographs is related to interference of light with the periodic structures.[39]

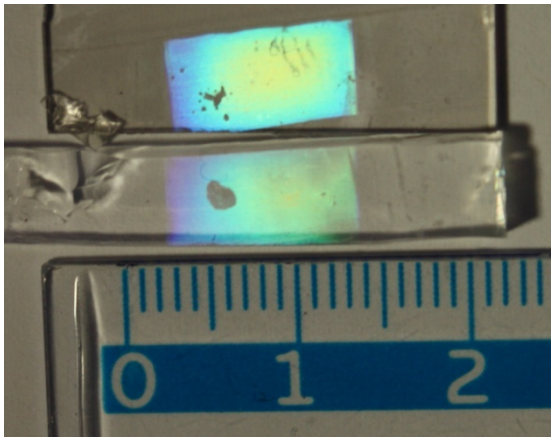

Fig 4-3 Digital camera pictures of the wrinkled PDMS-stripe (bottom) and the corresponding glass substrate (top) with the transferred Silica-PNIPAM particles of sample Sil-100 λ_{1200}, illuminated with white light. The iridescent colors occur due to interference of the incident light with the periodic particle arrays.

4.3.4 *Spin-Release with Ag-PNIPAM core-shell particles*

The presented results for the assembly of silica–PNIPAM core–shell particles show the influence of the PDMS template wavelength and the core dimensions on the assembly structure. Due to the presence of the PNIPAM shell, the silica cores are well separated in the aligned structures. In order to obtain linear assemblies with interesting optical properties, we synthesised Ag–PNIPAM core–shell particles by precipitation polymerisation of NIPAM and BIS in the presence of functionalised Ag nanoparticles.

The size and morphology of the Ag–PNIPAM core–shell particles were characterised by means of transmission electron microscopy (TEM) and dynamic light scattering (DLS).

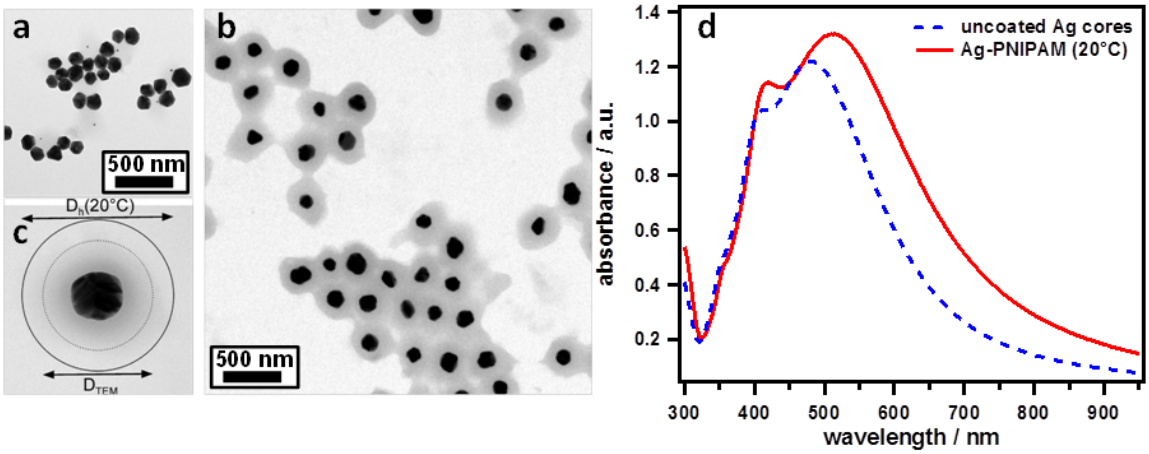

Fig 4-4 (a) TEM image of uncoated silver nanoparticles. (b) Ag-PNIPAM core-shell particles. (c) Magnification of a single core-shell particle. The two circles illustrate the hydrodynamic diameter in the swollen state (D_h(25 °C)) as well as the diameter from TEM, D_{TEM}. d) UV-Vis spectrum of the uncoated silver nanoparticles (blue, dashed line) and the Ag-PNIPAM core-shell particles (solid, red line) in aqueous dispersion at 20 °C.

Figure 4-4a shows a representative TEM image of the uncoated silver particles. The diameter of the Ag cores was determined by analysing the size of 150 individual Ag cores from various TEM images and found to be 105 ± 19 nm. The TEM images in Fig 4-4b and c show the silver–PNIPAM core–shell particles. Here the core–shell structure is clearly visible. The diameter of the overall core–shell particles is 260 ± 20 nm as determined from TEM images and 360 nm as determined by DLS at 20 °C. It is noted that the particle size is rather difficult to determine by TEM due to the low contrast of the polymer shell. In addition, in electron microscopy the particles are imaged in a rather collapsed state due to the high vacuum in the microscope. As a consequence, the size from DLS is much more reliable and also gives a representative value of the particle dimensions in the swollen state, the state under which the assembly was done. The optical properties of the hybrid system were analysed by UV-Vis spectroscopy. Fig 4-4d represents UV-Vis absorbance spectra recorded from dilute dispersions of the uncoated silver particles and the silver–PNIPAM core–shell particles in water at 20 °C. Due to the rather large dimensions of the Ag cores not only a dipole plasmon mode at $\lambda \approx 500$ nm but also a quadrupole mode at $\lambda \approx 400$ nm is observed.[40] It can be seen that the plasmon resonances are slightly red-shifted for the core–shell system. These shifts can be related to the change of the local refractive index due to the polymer coating. To the best of our

knowledge core–shell particles from direct incorporation of metal nanoparticles of such large dimensions have not been presented in the literature yet. Only for silica particles as core material, this core-size range was explored.[31] The main advantages of the coating with PNIPAM are the enormous stability of the final particles and the induced increase in effective particle volume. Usually colloidal stability and protection against aggregation are rather strong limitations for metal nanoparticles. However, PNIPAM coated metal nanoparticles can be separated by centrifugation and redispersed multiple times. In addition, redispersion in media of different composition is possible (*e.g.* alcohols, chloroform) without addition of any further ligands. For 2D and 3D assemblies of metal nanoparticles on large areas a major limitation is the amount of particles which can be synthesised in a reasonable manner as well as the particle concentration which can be reached without loss of colloidal stability. Coating metal particles with rather thick polymer structures increases the effective particle volume without changing the particle properties significantly. In our case, the Ag–PNIPAM particles show the strong localised plasmon resonance of the bare Ag particles[40] but have an overall volume being 40 times larger than the initial Ag particle volume. This difference in volume allows obtaining higher volume fractions with a comparably low number of particles. As discussed above the inter-core distance can be manipulated by the used wrinkle wavelength. To achieve plasmon coupling between silver nanoparticles it is important to control the Ag core to core distance.[41] Based on the results discussed in Section 4.3.3 we decided to use wavelengths considerably larger than the particle diameter (Table 4-1) SEM images of the assembled structures are shown in Fig 4-5.

4.3.5 *Resulting structures*

The SEM images presented in Fig 4-5 demonstrate that homogeneous particle assemblies were obtained over large areas. The magnifications in Fig 4-5d and e show the found particle arrangements in detail: 2D zigzag lines and 3D pyramidal assemblies. The shell is detectable as faint shadow around the bright Ag-cores. The shells of Ag–PNIPAM overlap for the same reason as for the silica–PNIPAM core–shell particles described in Section 4.3.3. Caused by the higher material density due to the compression, the shell occurs brighter in SEM as to the left or right of the cores. In comparison, if the particles were spin coated on a plane substrate as shown for sample Ag-A (Fig 4-5a) no overlap is visible. In addition, no ordering is observed in the latter case.

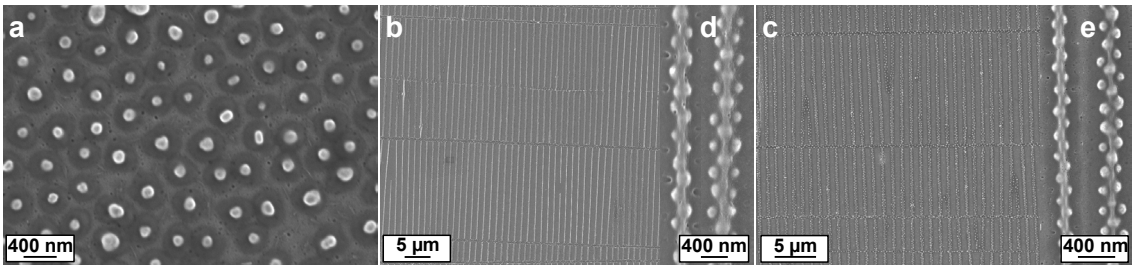

Fig 4-5 SEM images. (a) Sample Ag-A randomly adsorbed Ag-PNIPAM particles. (b) and (c) Linear assembly of sample Ag-B and sample Ag-C, respectively. (d) Magnification of the two structures found in sample Ag-B: 2d zigzag-lines and 3d pyramidal structures. (e) Magnification of the structures of sample (c) zigzag-lines and 3D pyramids. The PNIPAM shell appears as shadow around the Ag-cores. Wavelengths and amplitudes are summarized in Table 4-1.

Also for this Ag-system RDFs were calculated, to determine the nearest neighbour distance. As presented in Fig 4-6, calculated for at least 500 particles and the values of Table 4-1, the largest distance, with 433 ± 21 nm, is found for the sample Ag-A for randomly adsorbed particles. The graphs for sample Ag-B and Ag-C give the following information: first, the nearest neighbour distance from the first peak as mentioned before, second, the wavelength of the deposited structures. The second peak can be matched to the next row of particles, the third peak one row further, because peak three appears at twice the distance as peak two. For example for sample Ag-C peak two occurs at 1167 nm and peak three at 2306 nm. The wavelengths determined from RDF are also in good agreement with the wavelengths of the wrinkled PDMS. The smallest interparticle distance is achieved for sample Ag-C.

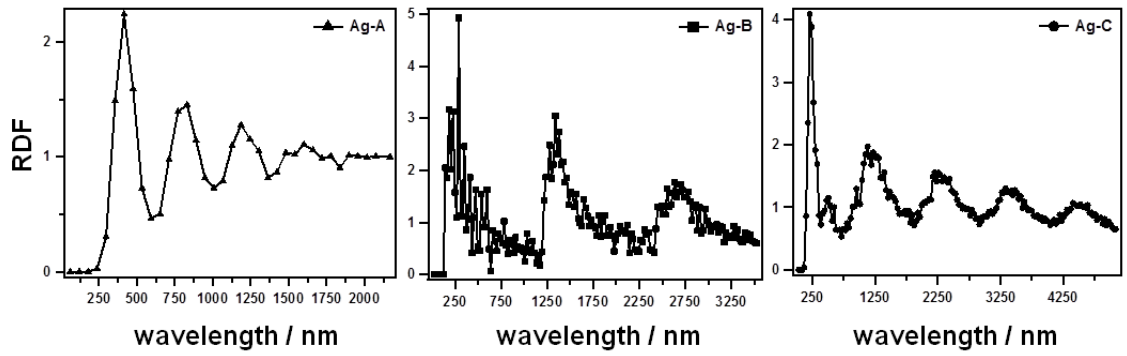

Fig 4-6: Radial distribution functions (RDF) of random adsorbed particles. From left to right: Sample Ag-A, Ag-B and Ag-C. The RDF-function gives the distance distribution from the particle centers to each other. The first peak gives the dominant inter particle distance to the next neigbour. For sample Ag-B and Ag-C the peaks at larger distances give the wavelength of the patterning. The results are summarized in Table 4-1. The calculation was done for more than 500 particles.

This can be explained as follows: the amount of core–shell particles for each SR process is similar, but the available volume under each confinement differs, due to differences in wavelengths and amplitudes. For sample Ag-B the wavelength and amplitude are larger than for sample Ag-C. Hence, the particles have more space and the packing is not as

dense compared to sample Ag-C. If the free volume is reduced, the particles are confined stronger and the shell is more compressed, due to the flexible soft PNIPAM network, which can be easily deformed.[42] It should be mentioned here that the volume decrease of the cavities must not be too drastic. If the volume reduction is in the range of the particle diameter the main structure will be changed from multiple particle lines to single particle lines, as it was discussed for the silica particles at 660 nm wavelength. The symmetries presented within the linear assemblies are similar to the ones predicted for hard spheres, as presented in Ref. [19]. A direct comparison of the hard sphere assemblies from Monte Carlo simulation and the results presented in this work is given in Fig. 4-7. The change in morphology for MC-simulation of the top image and the bottom image is caused by increasing volume fraction of the particles. The changes in sample Ag-C must be caused by a local concentration gradient. It can be seen that the metal cores from our Ag–PNIPAM core–shell system are well-separated, due to the presence of the soft PNIPAM shell. In order to investigate the influence of confinement on the structuring process of core–shell particles, we employ a minimal model, similar to the hard-core model explained in detail in ref.[19]. For the simulation we allow particle interactions using a hard core diameter σ_c and a soft repulsive shell with an exponentially decaying potential with range $\sigma_c = 3\sigma_c$ equal to the total diameter σ_s of the core plus the polymer shell.

$$U(r) = \begin{cases} \infty & r < \sigma_c \\ A\left[\exp\left(-\kappa\left(r-\sigma_c\right)\right) - \exp\left(-\kappa\left(\sigma_s-\sigma_c\right)\right)\right] & \sigma_c < r < \sigma_s \\ 0 & otherwise \end{cases}$$

We fixed the parameters $\kappa\sigma_c = 2$ and $A = 200k_BT$, with k_B the Boltzmann constant and T the temperature. The particles were confined between one smooth planar hard wall and one sinusoidal hard wall with wavelength $12\sigma_c$ and amplitude $1.3\sigma_c$. The system was equilibrated with Monte Carlo simulations with a particle number of the order of 100, for a total of 10^6 MC steps per particle. We used compression runs, where a constant normal pressure was applied to the wrinkled wall until an equilibrium configuration was reached. The results are presented in Fig 4-7, right. As can be clearly seen, in contrast to the results from simulation for hard spheres, the SEM image of sample Ag-C as well as the simulation for hard-core/soft-shell particles show well separated nanoparticle cores. This separation can be attributed to the soft PNIPAM shell, acting as a spacer.[43] Furthermore, the soft shell and the conditions under confinement lead to structures

which are compressed. This leads to distorted angles in the zigzag lines, other than in the model prediction for hard spheres. Also for pyramidal patterning the confinement and the shell have an influence on the formed structure. The distance between the base particles is increased. Simulations for hardcore/ soft-shell particles lead to a better agreement with the experimentally obtained results, as one can see in Fig 4-7, right. For the experiment (middle) as well as for the MC results (right) the angle between the zigzag aligned particles deviates from 60° as one might expect for close packed structures and how it was computed for the hard sphere simulation. Also for the pyramidal patterning the adjusted MC-simulation is able to reproduce the experimental patterns. The influence of compression and the shell size are tools, which allow control of the inter-particle distance, by decreasing or increasing wavelengths and amplitudes of the wrinkles or by varying the shell thickness and density of PNIPAM.[34]

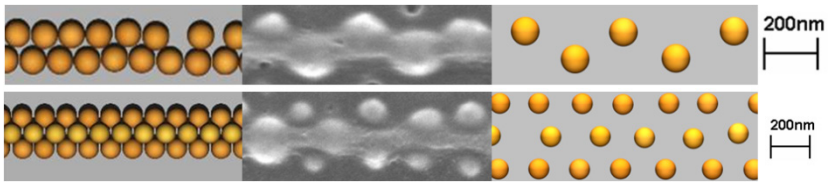

Fig 4-7: Comparison of the local assembly structure from sample Ag-C (middle) to results from MC-simulations for hard spheres (left)[19]and MC-simulation for hard-core/soft-shell (right). In the latter simulation, only the cores are presented. For the MC-simulation the volume fraction increases from the top to the bottom, which leads to the different structures. The difference for sample C is probably caused by local concentration variations.

4.3.6 *Optical properties/UV-Vis measurement*

Fig 4-8a shows UV-Vis absorbance spectra of the linear assembled Ag–PNIPAM particles on glass (sample Ag-B) recorded under different polarisations of the incoming light. For unpolarised light the dipole mode of the Ag particles is located at $\lambda \approx 530$ nm, whereas the quadrupole mode is at $\lambda \approx 428$ nm. Both values are red shifted compared to their peak positions from aqueous dispersion shown in Fig. 4-4d. These shifts can be related to the change in refractive index when the particles are deposited on glass ($n = 1.47$ compared to $n = 1.33$ for water). If now the incoming light is polarised parallel to the direction of the linear assembly (0°), the overall absorbance decreases over the whole range of wavelength showing the strongest deviation in a range of $\lambda = 650 - 800$ nm. In contrast a stronger absorbance in this range is found for polarisation perpendicular to the direction of the linear assembly (90°). Fig 4-8B compares the spectrum recorded under unpolarised conditions with the average spectrum, which can be calculated from

the spectra for 0° and 90° polarisation. It can be clearly seen that the number average of the two polarised spectra resembles the spectrum measured under unpolarised conditions.

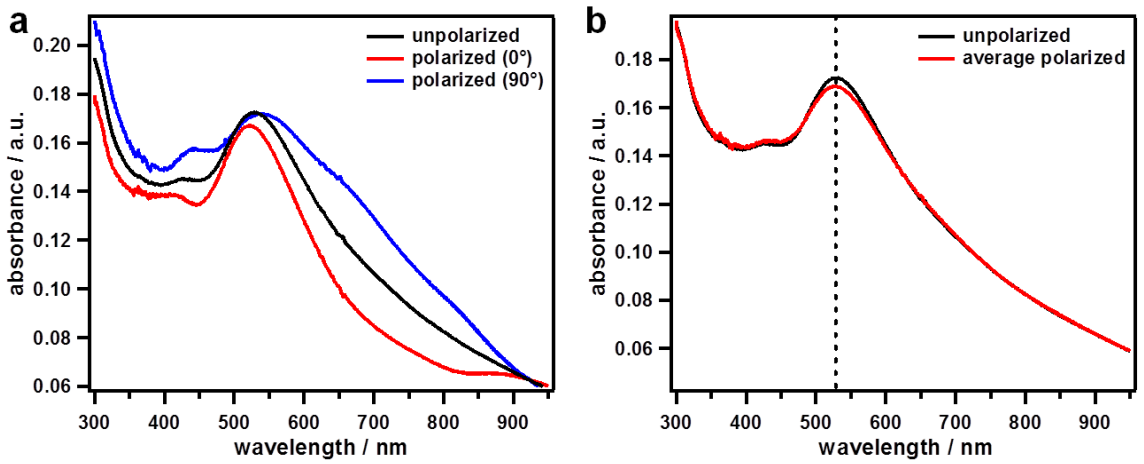

Fig 4-8: Top: (a) UV-Vis absorbance spectra for different polarisations of the incoming beam. Black solid line: Unpolarised light. Red line: Polarised light parallel to the direction of the linear assembly of the Ag-PNIPAM particles. Blue line: Polarisation perpendicular to the structure on the glass substrates. (b) Presents a comparison of the absorbance spectrum measured with unpolarised light (black solid line) and the number average of the spectra recorded for 0° and 90° of polarisation (red line). The dashed line indicates the position of the dipole mode.

However, a quantitative analysis of the spectra cannot be given here and is not within the scope of the manuscript. Nevertheless, the spectra nicely demonstrate that local (presumably plasmonic) coupling of the metal cores results in anisotropic optical properties. Further investigations, also with core–shell particles of various shell thicknesses and exploring the tunability of inter-particle distances by utilising the stimulus responsivity of the shell, are underway. As an example of collective effects, we show diffraction patterns arising from the periodic arrangement with periodicities in the range of the wavelength (here 1300 nm). Diffraction spots up to 4th order are visible even with a simple home-built setup, indicating the high quality and large index of refraction contrast of the particle arrangements. Laser diffraction was studied using a laser pointer (λ = 522-542 nm at < 100 mW). Up to four diffraction orders could be observed for both samples, Ag-A and Ag-B. This reveals the high degree of order of the linear particle assemblies. Fig 4-9 shows a representative photograph of the observed diffraction. In this photograph the laser illuminates the sample from the top as indicated by the arrow. The transmitted beam is visible as a bright, circular spot below the sample. On the left and right hand side of the direct beam, the first and second order diffraction spots are visible. We used the position of the first order diffraction spots in order to calculate the wavelength of the linear assemblies Λ according to

$$\Lambda = \frac{2\pi}{q}$$

with the momentum transfer

$$q = \frac{4\pi}{\lambda} sin\frac{\theta}{2}$$

where λ is the laser wavelength and θ the angle of diffraction. We found Λ = 1300 ± 20 nm for sample B and Λ = 1200 ± 20 nm for sample Ag-C. These values are in good agreement with the values obtained from SEM and RDF as listed in Table 4-1.

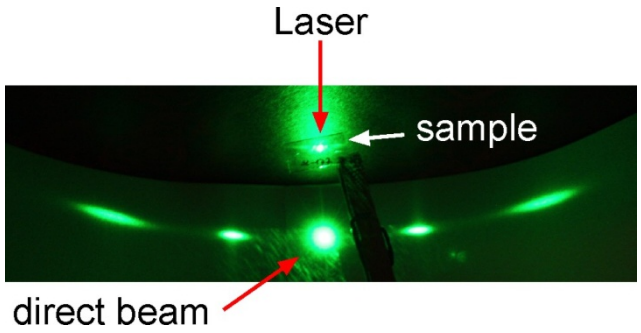

Fig 4-9: Diffraction of normally incident light on sample Ag-C using a laser pointer. In this photograph, the first and second order diffraction spots are visible.

4.4 Conclusion

We have shown that wrinkle-assisted assembly of silica– and silver–PNIPAM core–shell particles allows the top-down fabrication of highly ordered linear particle assemblies. The use of wrinkle templates (PDMS) with different cavity volumes significantly influences the local structure of the assemblies. Moreover, we find well-pronounced inter-core separations due to the presence of the polymer shell (PNIPAM). As a consequence of the soft character of the polymer shell, differences of the local structure, as compared to the structure of assembled hard spheres, can be observed. In particular, interparticle distances are greatly reduced and the particle assemblies appear ''compressed'' in the direction perpendicular to the wrinkle direction. The excellent agreement between experiments and Monte-Carlo simulations provides solid evidence that the soft nature of the inter-particle potential is the reason for these effects. We show first evidence that there are both local coupling effects and cooperative optical effects for these structures: polarisation dependent absorbance measurements using UV-Vis spectroscopy have shown that the particle assemblies display optical anisotropy. This anisotropy can be related to coupling of the Ag cores. At the same time, pronounced diffraction peaks indicate the high long range order and hence the good quality of the

produced surface pattern. The presented method is a fast, cost-effective approach to generate structures with high anisotropy also noticeable macroscopically by polarisation dependent absorbance behaviour. The PNIPAM shell allows nanoparticle separation which is of interest for the preparation of assemblies with control over the nanoparticle plasmon resonance coupling. Moreover it has the potential for tuning inter-particle distances by external stimuli, since the gel-shell is stimuli responsive. Experiments on tuning the plasmon coupling are currently underway and will be presented elsewhere.

Acknowledgements

We wish to acknowledge Alexandra Schweikart for the introduction into the topic, her preliminary work and numerous useful advices on handling of wrinkles. The authors acknowledge the German Science Foundation (DFG) for funding through SFB 840 (TP B5 and B6).

References

1. Pazos-Perez, N.; Ni, W.; Schweikart, A.; Alvarez-Puebla, R. A.; Fery, A.; Liz-Marzan, L. M. *Chemical Science*, **2010**, 1, 174-178.
2. Romo-Herrera, J. M.; Alvarez-Puebla, R. A.; Liz-Marzan, L. M. *Nanoscale*, **2011**, 3, 1304-1315.
3. Fan, J. A.; Wu, C.; Bao, K.; Bao, J.; Bardhan, R.; Halas, N. J.; Manoharan, V. N.; Nordlander, P.; Shvets, G.; Capasso, F. *Science*, **2010**, 328, 1135-1138.
4. Velev, O. D.; Gupta, S. *Advanced Materials*, **2009**, 21, 1897-1905.
5. van Blaaderen, A.; Ruel, R.; Wiltzius, P. *Nature*, **1997**, 385, 321-324.
6. Yin, Y.; Lu, Y.; Gates, B.; Xia, Y. *Journal of the American Chemical Society*, **2001**, 123, 8718-8729.
7. Xia, D. Y.; Biswas, A.; Li, D.; Brueck, S. R. J. *Advanced Materials*, **2004**, 16, 1427-+.
8. Masuda, Y.; Itoh, M.; Yonezawa, T.; Koumoto, K. *Langmuir*, **2002**, 18, 4155-4159.
9. Xia, Y.; Rogers, J. A.; Paul, K. E.; Whitesides, G. M. *Chemical Reviews*, **1999**, 99, 1823-1848.
10. Wua, B. Q.; Kumar, A. *J. Vac. Sci. Technol. B*, **2007**, 25, 1743-1761.
11. Melngailis, J.; Mondelli, A. A.; Berry, I. L.; Mohondro, R. *J. Vac. Sci. Technol. B*, **1998**, 16, 927-957.
12. Costner, E. A.; Lin, M. W.; Jen, W. L.; Willson, C. G. Nanoimprint Lithography Materials Development for Semiconductor Device Fabrication. In *Annual Review of Materials Research*, Annual Reviews: Palo Alto, 2009; Vol. 39, pp 155-180.

13. Lu, C.; Mohwald, H.; Fery, A. *Soft Matter*, **2007**, 3, 1530-1536.
14. Bowden, N.; Huck, W.; Paul, K.; Whitesides, G. **1999**, - 75.
15. Genzer, J.; Groenewold, J. *Soft Matter*, **2006**, 2, 310-323.
16. Schweikart, A.; Zimin, D.; Handge, U. A.; Bennemann, M.; Altstädt, V.; Fery, A.; Koch, K. *Macromolecular Chemistry and Physics*, **2010**, 211, 259-264.
17. Mrksich, M.; Whitesides, G. M. *Trends in Biotechnology*, **1995**, 13, 228-235.
18. Pretzl, M.; Schweikart, A.; Hanske, C.; Chiche, A.; Zettl, U.; Horn, A.; Böker, A.; Fery, A. *Langmuir*, **2008**, 24, 12748-12753.
19. Schweikart, A.; Fortini, A.; Wittemann, A.; Schmidt, M.; Fery, A. *Soft Matter*, **2010**, 6, 5860-5863.
20. Karg, M.; Hellweg, T. *J Mater Chem*, **2009**, 19, 8714-8727.
21. Maier, S. A.; Kik, P. G.; Atwater, H. A.; Meltzer, S.; Harel, E.; Koel, B. E.; Requicha, A. A. G. *Nat Mater*, **2003**, 2, 229-232.
22. Barrow, S. J.; Funston, A. M.; Gómez, D. E.; Davis, T. J.; Mulvaney, P. *Nano Letters*, **2011**, 11, 4180-4187.
23. Jain, P. K.; Eustis, S.; El-Sayed, M. A. *J Phys Chem B*, **2006**, 110, 18243-18253.
24. Funston, A. M.; Novo, C.; Davis, T. J.; Mulvaney, P. *Nano Letters*, **2009**, 9, 1651-1658.
25. Schweikart, A.; Pazos-Perez, N.; Alvarez-Puebla, R. A.; Fery, A. *Soft Matter*, **2011**, 7, 4093-4100.
26. Karg, M.; Pastoriza-Santos, I.; Perez-Juste, J.; Hellweg, T.; Liz-Marzan, L. M. *Small*, **2007**, 3, 1222-1229.
27. Makino, K.; Yamamoto, S.; Fujimoto, K.; Kawaguchi, H.; Ohshima, H. *Journal of Colloid and Interface Science*, **1994**, 166, 251-258.
28. Linse, P. *The Journal of Chemical Physics*, **2007**, 126, 114903-13.
29. Karg, M.; Hellweg, T. *Current Opinion in Colloid & Interface Science*, **2009**, 14, 438-450.
30. Karg, M.; Hellweg, T.; Mulvaney, P. *Adv. Funct. Mater.*, **2011**, 8.
31. Karg, M.; Wellert, S.; Prevost, S.; Schweins, R.; Dewhurst, C.; Liz-Marzan, L. M.; Hellweg, T. *Colloid Polym Sci*, **2011**, 289, 699-709.
32. Stober, W.; Fink, A.; Bohn, E. *Journal of Colloid and Interface Science*, **1968**, 26, 62-&.
33. Sharma, V. K.; Panacek, A.; Kvitek, L.; Prucek, R.; Kolar, M.; Vecerova, R.; Pizurova, N.; Nevecna, T.; Zboril, R. *J Phys Chem B*, **2006**, 110, 16248-16253.
34. Karg, M.; Jaber, S.; Hellweg, T.; Mulvaney, P. *Langmuir*, **2011**, 27, 820-827.
35. Kern, W.; Piotinen, D. A. *RCA Rev.*, **1970**, 31, 19.
36. Hiltl, S.; Schurings, M.-P.; Balaceanu, A.; Mayorga, V.; Liedel, C.; Pich, A.; Boker, A. *Soft Matter*, **2011**, 7, 8231-8238.
37. Horn, A.; Hiltl, S.; Fery, A.; Böker, A. *Small*, **2010**, 6, 2122-2125.
38. Karg, M.; Pastoriza-Santos, I.; Liz-Marzan, L. M.; Hellweg, T. *Chemphyschem*, **2006**, 7, 2298-2301.
39. Pursiainen, O. L.; Baumberg, J. J.; Winkler, H.; Viel, B.; Spahn, P.; Ruhl, T. *Opt. Express*, **2007**, 15, 9553-9561.
40. Evanoff, D. D.; Chumanov, G. *Chemphyschem*, **2005**, 6, 1221-1231.

41. Kinnan, M. K.; Chumanov, G. *The Journal of Physical Chemistry C*, **2010**, 114, 7496-7501.
42. Tagit, O.; Tomczak, N.; Vancso, G. J. *Small*, **2008**, 4, 119-126.
43. Jaber, S.; Karg, M.; Morfa, A.; Mulvaney, P. *Phys Chem Chem Phys*, **2011**, 13, 5576-5578.

5 Large-Area Organization of PNIPAM-Coated Nanostars as SERS Platforms for Polycyclic Aromatic Hydrocarbons Sensing in Gas Phase

Mareen Müller,[a] Moritz Tebbe,[a] Daria A. Andreeva,[a] Matthias Karg,[b] Ramón A. Álvarez Puebla,[c] Nicolas Pazos Peréz[a], and Andreas Fery[a]**

[a] Physical Chemistry II, University of Bayreuth, Universitätsstr. 30, 95447 Bayreuth, Germany

[b] Physical Chemistry I, University of Bayreuth, Universitätsstr. 30, 95447 Bayreuth, Germany

[c] Departemento de Quimica Fisica, Universidade de Vigo, 36310, Vigo, Spain

* e-mail: andreas.fery@uni-bayreuth.de

* e-mail: nicolas.pazos@uni-bayreuth.de

Published in *Langmuir* **2012**, 28, 9168-9173

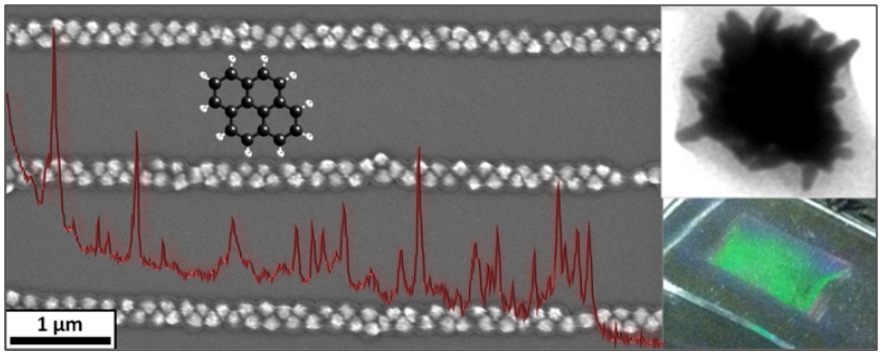

Abstract

Here, a new surface enhanced Raman spectroscopy (SERS) platform suitable for gas phase sensing based on the extended organization of poly-N-isopropylacrylamide (PNIPAM)-coated nanostars over large areas is presented. This system yields high and homogeneous SERS intensities, and simultaneously traps organic chemical agents as pollutants from the gas phase. PNIPAM-coated gold nanostars were organized into parallel linear arrays. The optical properties of the fabricated substrates are investigated, and applicability for advanced sensing is demonstrated through the detection in the gas phase of pyrene traces, a well-known polyaromatic hydrocarbon.

5.1 Introduction

Surface enhanced Raman spectroscopy (SERS) is a spectroscopic technique with the ability to yield ultrasensitive detection of molecules under environmental conditions without special sample preparation. The requirements to obtain strong SERS include an optical enhancer, typically a metallic nanostructure, that produces an intense electromagnetic field at its surface upon excitation with the appropriate light (*i.e.*, localized surface plasmon resonance, LSPR) and the proximity of analyte molecules to the metallic nanostructure. So far, a variety of nanostructures of gold and silver have been introduced in the literature as optical enhancers. For example, single-molecule SERS was reached for the first time using silver nanoparticle aggregates.[1, 2] The formation of aggregates was necessary to obtain highly active regions where the electromagnetic field is gigantic due to the interparticle plasmon interaction (i.e., hot spots).[3, 4] Unfortunately, aggregation yields heterogeneous surfaces where the hot spots are randomly distributed in intensity, shape, and density. This makes quantitative detection impossible, as all the spots for a given surface are intrinsically different in their optical properties.[5] In other words, quantitativity is sacrificed in order to gain sensitivity. To solve this issue, much effort has been dedicated to produce metallic structures, which are well-defined on the nanoscale and thus give rise to hot-spots of uniform intensity, shape, and density: Evaporated films have been lithographically etched with electron or ion beams providing homogeneous optical platforms.[6] Unfortunately, lithographic etching is time consuming, expensive, and cannot be carried out over large areas. Alternatives to these methods have been proposed. For example, the Van Duynés group

developed a surface modification by combining nanosphere lithography with metal films over the nanospheres (NSL-FON), which results in a homogeneous high efficient optical platform that can be produced over large areas.[7, 8] On the other hand, another approach recently developed by our groups consists of the confinement of preformed colloidal nanoparticles aided by controlled polymer wrinkling.[9] This alternative yields inexpensive, highly homogeneous, and efficient SERS platforms that can be patterned over large areas with minimum technical requirements.[10, 11]

As mentioned before, the other requirement to obtain strong SERS relies on the molecule to be analyzed. SERS is eminently a first-layer effect. In general, molecules that have strong affinity toward the metallic nanostructured surface lead to strong SERS signals. However, molecules with low or no affinity usually do not yield SERS. To solve this problem, nanostructures have been functionalized with a variety of materials that may attract/ increase the concentration of the analyte close to the plasmonic surface.[12] As an example, polycyclic aromatic hydrocarbons (PAHs), a class of naturally formed persisting air pollutants that can induce severe cancer and poisoning, have been detected in solution by adding functionalities to the plasmonic surfaces such as thiolated alkyl chains,[13] viologen,[14] humic acids,[15] or cyclodextrins.[16] Poly-N-isopropylacrylamide (PNIPAM)-coated nanoparticles have been demonstrated as one of the most effective molecular traps, especially for hydrophobic analytes.[17] However, a homogeneous coating of the nanoparticles by polymers such as PNIPAM completely inhibits the plasmon coupling of the metal cores if the polymer shell has a certain thickness. In other words, the polymer shell, acting as a sterical spacer between the metal cores, prevents the formation of hot spots. Therefore, the achieved sensitivity is quite modest. One alternative relies on the generation of aggregates, which will increase the SERS intensity[18] but, as previously commented, will lead to intensity fluctuations due to the random generation of hot spots. Another alternative exploits the coating of starshaped nanoparticles.[19-23] In these highly branched nanoparticles, the core acts as a plasmonic nanoantenna, while the tips concentrate the electromagnetic field at their apex.[24, 25] In fact, these nanostars are one of the very little number of SERS platforms able to sustain an electric field large enough to be used as single-particle SERS substrates.[26-28] Notably, a distinctive property of these particles is that, upon aggregation, their optical efficiency decreases. This phenomenon occurs because the interaction of different particles with different symmetries leads to field deactivation rather than plasmon Experimental

coupling.[29] Thus, in this scenario the polymer coating not only adds a trapping functionality to the structure but will preserve its unique optical properties.

Scheme 5-1 (1) Synthesis and functionalization of Au nanoparticles. (2) PNIPAM coating of AU nanoparticles. (3) PVP functionalization and nanostar overgrowth. (4) Fabrication of a PDMS wrinkled surface. (5) Nanoparticle organization

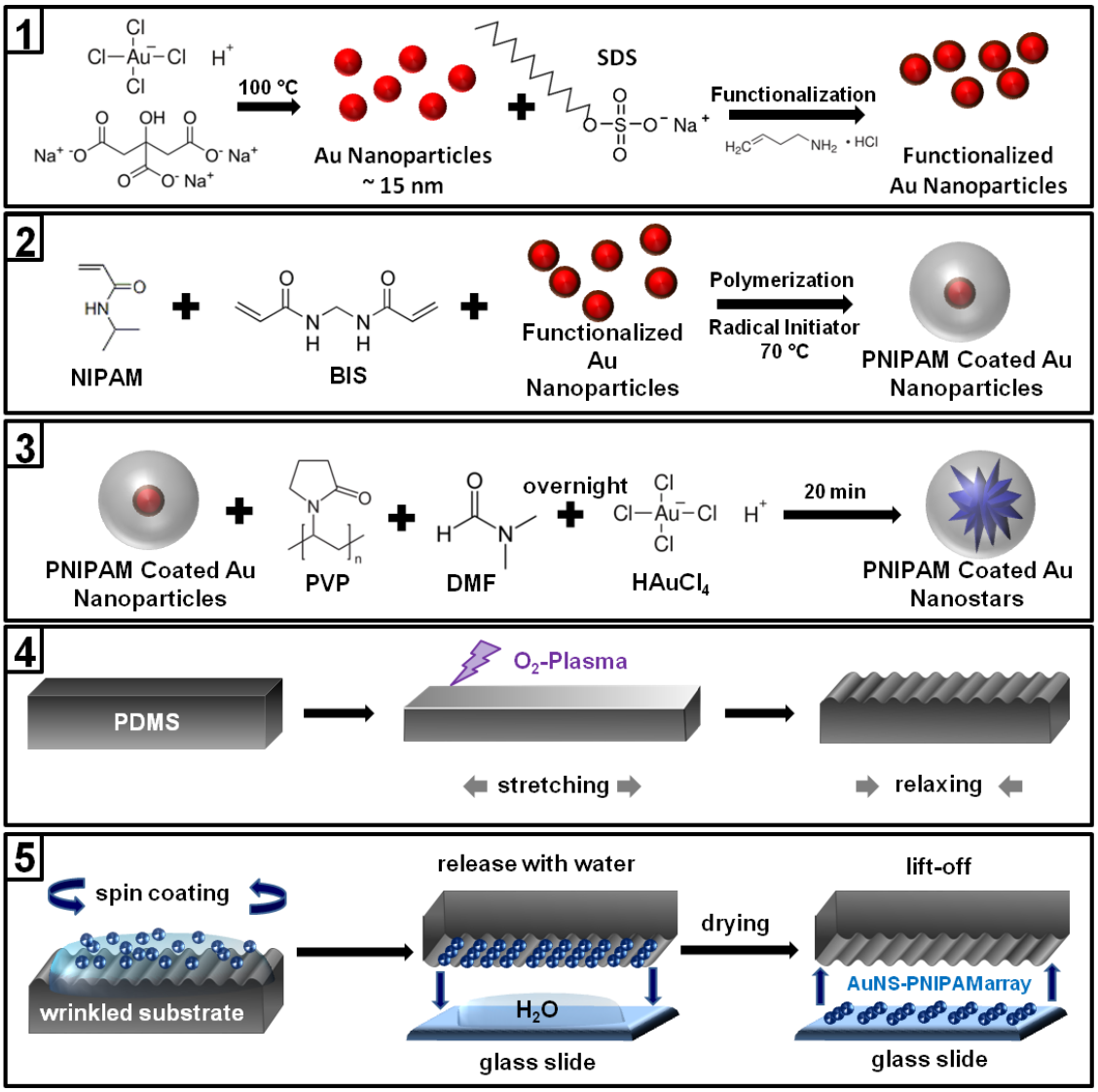

Herein we show the preparation of optically active gold nanostars coated with PNIPAM and their controlled assembly into highly ordered linear structures. The optical properties of the imprinted particle assemblies were characterized, and the SERS efficiency was compared with films of PNIPAM-coated gold stars and coated gold spheres, respectively. Finally, demonstration of their capabilities for gas sensing was illustrated by the detection of the PAH pyrene in the gas phase.

5.2 Experimental

Materials

Gold(III) chloride trihydrate ($HAuCl_4 \times 3H_2O$), trisodium citrate dihydrate, N,N-dimethylformamidee, N-isopropylacrylamide (NIPAM), butenylamine hydrochloride (BA), ethanol, benzenethiol (BT), pyrene and poly(vinylpyrrolidone) (PVP, $M_w = 10\,000$) were purchased from Aldrich. Polydimethylsiloxane (PDMS) Sylgard (184) silicon elastomer, curing agent, and precursor were purchased from Dow Corning, USA. N,N-Methylenebisacrylamide (BIS) and potassium peroxodisulfate (PPS) were acquired from Fluka. Sodium dodecyl sulfate (SDS) was from Ajax Laboratory Chemicals. All chemicals were used as received. Water was purified using a Millipore Milli-Q system (resistivity higher than 18 $M\Omega cm^{-1}$). All experiments were carried out at room temperature.

5.2.1 *Synthesis of PNIPAM-coated Gold Nanoparticles*

Au@PNIPAM core−shell particles were prepared by precipitation polymerization of the monomer NIPAM in the presence of functionalized, spherical gold nanoparticles as reported elsewhere.[30] First, gold nanoparticles approximately 15 nm in diameter were synthesized according to the well-known method by Turkevich and Enüstün.[31] Briefly, 2.5 mL of an aqueous solution of $HAuCl_4$ (0.1 M) was added to 497.5 mL of water in a conical flask of 1 L volume. The light yellow, clear solution was heated to heavy boiling under continuous stirring with a magnetic stirrer, and 25 mL of water containing 255 mg trisodium citrate was added quickly. The solution turned colorless immediately after the addition of citrate and turned deep red within the next 5 min. The solution was kept boiling for 20 min upon the addition of citrate and was then cooled to room temperature. Then, the gold particles were surface functionalized by the addition of 3 mL of an aqueous SDS solution (0.62 mM) and, after 20 min, the addition of 980 µL of a solution of BA in ethanol (0.12 mM). Twenty minutes after the addition of BA, the particle dispersion was cleaned and concentrated by repeated centrifugation. Three centrifugation steps were performed (each for 90 min at 3500 rpm). Finally, the residues were collected, resulting in a deep red nanoparticle dispersion with a concentration [Au] = 0.01 M (see Scheme 5-1 (1)).

The growth of the PNIPAM shell around the gold nanoparticles was performed by precipitation polymerization using 1.188 g of the monomer NIPAM and 243 mg of the

cross-linker BIS, dissolved in 350 mL of water. The solution was stirred in a three-neck roundbottom flask of 500 mL volume and heated to 45 °C while degassing with nitrogen. After 20 min of degassing, 5.32 g of the concentrated dispersion of functionalized gold nanoparticles ([Au] = 0.01 M) were injected dropwise with a syringe. In the following, the red and clear reaction medium was heated to 70 °C and after an equilibration time of 10−15 min, 5 mg PPS dissolved in 1 mL of water were added in order to initiate the polymerization. The reaction was allowed to occur for 2 h. Then, the turbid, red dispersion was cooled to room temperature. Cleaning of the core−shell particles was done by repeated centrifugation and redispersion in water (3 h at 9000 rpm, two repetitions). Finally, the residues were collected and freeze-dried (see Scheme 5-1(2)).

5.2.2 *PVP Functionalization and Nanostar Growth*

The previously described PNIPAM coated gold nanoparticles (0.023 g) were dispersed in 5 mL ethanol via sonication during 20 min. This solution (350 µL) was added to a solution containing 4.88 g of PVP in 35 mL of N,N-dimethylformamidee. The solution was sonicated for 30 min and was left standing overnight to allow diffusion of PVP to the Au surface. Next, 105 µL of an aqueous solution of 0.105 M $HAuCl_4$ were added rapidly under vigorous stirring. Within 20 min, the color of the solution changed from pink to colorless, and finally turned blue, indicating the formation of gold nanostars. The dispersion was kept overnight with continuous stirring (see Scheme 5-1 (3)). After that, the solution was centrifuged at 7000 rpm for 20 min, the clear supernatant was discarded, and the precipitate was redispersed in 40 mL of ethanol. This process was repeated three times. Before organizing the particles, the solution was concentrated to a final volume of 2 mL via centrifugation steps at 7000 rpm for 20 min. Finally, 1 mL of the previously concentrated solution was centrifuged again at 7000 rpm for 20 min, the supernatant was discarded, and the precipitate redispersed in a total volume of 0.5 mL of milli-Q water.

5.2.3 *Particle Organization.*

In order to organize the particles on substrates, the fabrication of a PDMS wrinkled surface is required as a template.[9-11] The PDMS elastomer was prepared by mixing Sylgard 184 with a 10 : 1 ratio by mass of prepolymer to curing agent. The mixture was stirred and filled in a clean, flat Petri dish. After 24 h at room temperature and baking at

80 °C for 5 h, the cross-linked PDMS was cut into 30 × 8 mm stripes. One of these stripes was stretched uniaxially in a custom-made apparatus to a strain of 25% of the initial length. The stretched substrate was oxidized during 900 s in oxygen plasma at 0.2 mbar using a plasma etcher operating at 0.1 kW (flecto10, Plasma Technology, Germany). After that, the sample wasrelaxed, and wrinkles with a periodicity of 1700 nm were obtained (see Scheme 5-1 (4)). The hydrophilic wrinkled substrates were used directly after plasma treatment. Briefly, a drop of the nanoparticles solution (20 µL) was spin coated onto the wrinkled PDMS at 1500 rpm for 1 min.[32] Next, a drop of water (10 µL) was placed on a clean glass slide,[10, 33] and the wrinkled PDMS containing the particles was placed on top of the water droplet. The system was left undisturbed for 2 h in order to allow the water to evaporate. After that, the PDMS was removed, and the particles remained organized into lines on the glass slide (see Scheme 5-1 (5)).

Spin coating at 1500 rpm for 1 min of 15 nm spherical gold cores coated with PNIPAM and 130 nm gold stars coated with PNIPAM was also performed for control experiments.

5.2.4 *Characterization*

Ultraviolet−visible (UV−vis) spectroscopy (PerkinElmer, Lambda 19), transmission (TEM) and scanning (SEM) electron microscopies (LEO 922 EFTEM operating at 200 kV and LEO 1530 FE-SEM, Zeiss, respectively) were applied to characterize the optical response, structure, and size of the nanoparticles and their arrays.

Optical surface enhancing Raman activity was characterized using BT in the gas phase. BT was adsorbed on the whole surface of the metallic samples by casting a drop of BT (0.1 M in ethanol) in a Petri dish where the substrate was also contained. SERS spectra were collected in backscattering geometry with a Renishaw Invia Reflex system equipped with two-dimensional charge-coupled device (2D-CCD) detector and a Leica confocal Microscope. The spectrograph uses a high-resolution grating (1200 gcm^{-1}) with additional bandpass filter optics. Excitation of the sample was carried out with a 830 nm diode laser line, with acquisition times of 200 ms and power at the sample of about 1 mW, using the Renishaw's StreamLine accessory. The laser was focused onto the sample with a 50x objective. For pyrene detection, the analyte was adsorbed in the gas phase by placing the samples and a drop of pyrene (10 mM in ethanol) (organized lines

of PNIPAM-coated nanostars and a film with uncoated nanostars for reference) in an oven at 150 °C with vacuum for 10 min.

5.3 Results and discussion

In order to obtain gold nanostars coated with homogeneous polymer shells based on PNIPAM, core−shell particles with spherical gold cores of 15 nm in diameter and PNIPAM shells with a total diameter of 273 nm as determined by dynamic light scattering (DLS) at 20 °C (AuNP@PNIPAM, Figure 5-1A) were prepared according to a recently reported protocol.[30]

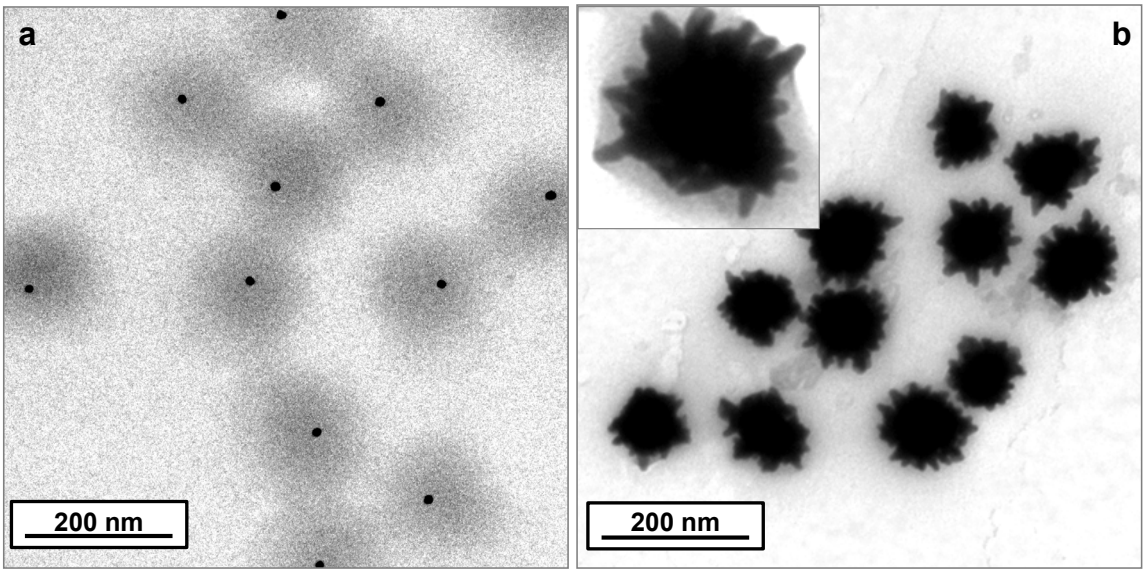

Figure 5-1 TEM images of (a) AuNP-PNIPAM and (b) AuNS-PNIPAM core-shell particles

Although the direct PNIPAM coating of gold nanostars (AuNS) has been recently reported,[19] this approach requires a rather time consuming procedure and the design of specific chemicals. Hence, to fabricate the final AuNS-PNIPAM, PNIPAM-coated gold spheres were used as seed particles for the further overgrowth of the metal core. In this synthetic approach, it is very important to previously functionalize the seed particles with PVP before adding the growth solution, thus allowing the epitaxial growth of the gold onto the spheres and the formation of spikes, as can be seen in Figure 5-1b. During this process, the color of the solution gradually turns from red to dark blue. This change of color indicates the formation of stars. The obtained particles have a nanostar core of 130 nm in diameter. The overall diameter of the core−shell particle is 250 nm, again determined using DLS at 20 °C.

The UV−vis−near-infrared (UV−vis−NIR) spectra of the prepared nanoparticles (Figure 5-2) show how the nanospheres are characterized by the typical LSPR at 520 nm, while, for the nanostars, this band remains as a shoulder of a much stronger absorption peak located at 810 nm. This last signal is attributed to the tip growth and is broad because of the overlapping of the plasmonic bands of tips with different lengths and aperture angles as previously reported.[26]

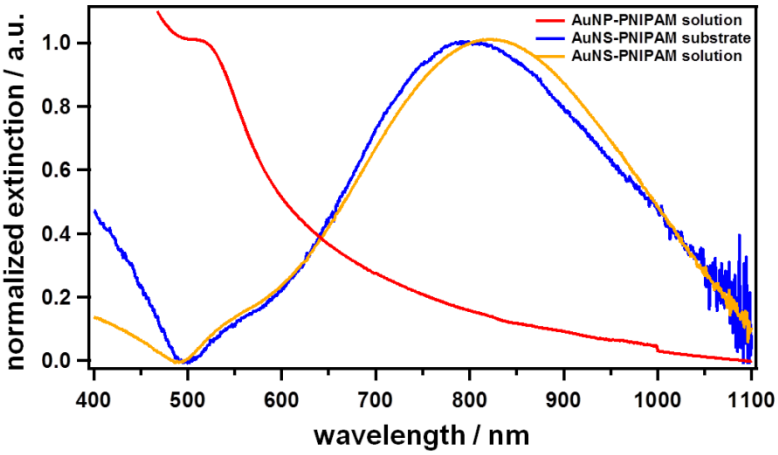

Figure 5-2 UV-Vis-NIR spectra of the AuNP-PNIPAM (red) and Au-NS-PNIPAM (yellow) in solution and after organization into lines on a substrate (blue)

In order to organize the core−shell particles in a linear fashion on planar substrates, we employed PDMS wrinkled substrates with a periodicity of 1700 nm as an assembly template, by spinning the particles onto the wrinkled PDMS[32] and transferring them on a clean glass slide.[10, 33] Notably, as observed by SEM (Figure 5-3) this method leads to a highly homogeneous patterning that can be extended over cm² (see, for example, the iridescent colors of the digital camera picture of the stamped colloidal lines, inset in Figure 5-3). The upper insets of Figure 5-3 show the internal geometry of the structure. This is characterized by double-particle zigzag lines with an overall width of 340 nm and a periodicity between them of 1700 nm. Within the line, the particles remain separated due to the PNIPAM shell. This spacing is also confirmed in the UV− vis−NIR spectrum of the patterned film (Figure 5-2, blue). It can be seen that the plasmon peak position remains very similar to that of the sample in solution with only a small blue-shift (10 nm). This shift is attributed to the change of the dielectric medium (air in the film, ethanol in the solution). Thus, the similarity in the plasmonic response indicates that there is no plasmonic interaction between neighbor particles.

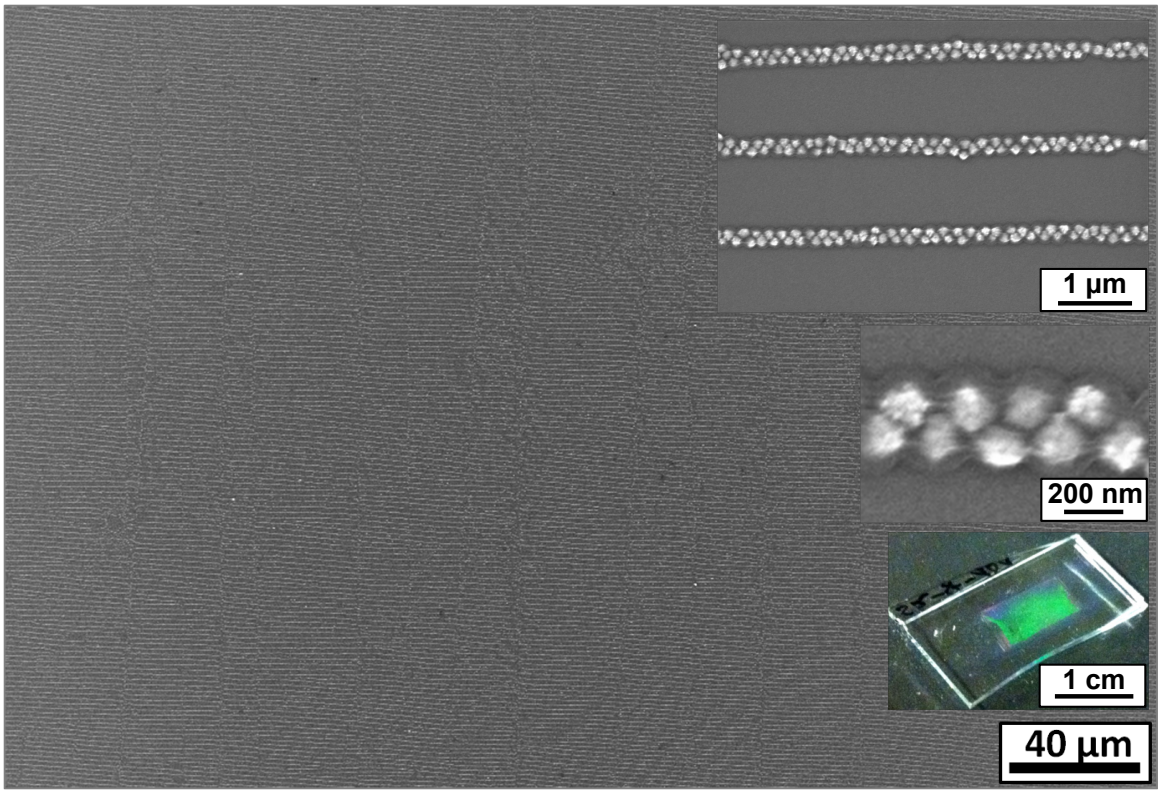

Figure 5-3 SEM images of the linear assembled AuNS-PNIPAM particles at different magnifications and a digital camera photograph showing the characteristic iridescence provided by the colloidal grating over ca. 1 cm.

To test the optical enhancing properties, BT was retained in the gas phase over all the film. Figure 5-4a shows the SERS spectrum on BT recorded on the AuNS-PNIPAM pattern. The spectrum is characterized by the BT typical vibrational pattern including the ring stretching (1573 cm^{-1}), C−H bending (1022 cm^{-1}), ring breathing (1073 and 999 cm^{-1}), and low frequency mode with contribution of C−S stretching (417 cm^{-1}) modes. Figure 5-4b, (c) shows the optical images and the SERS mappings over an extended area (40 × 40 µm, step size 1 µm) for the AuNS-PNIPAM patterned lines and spin-coated films. Notably, while the line patterned film shows slightly lower intensity than the corresponding spin-coated one, the signal remains constant spot to spot in contrast to the strong fluctuations found in the spin-coated film. For comparison, a spin-coated AuNP-PNIPAM film was also mapped (Figure 5-3d) without any SERS signal. This illustrates the optical efficiency of the stars as previously described elsewhere.[29]

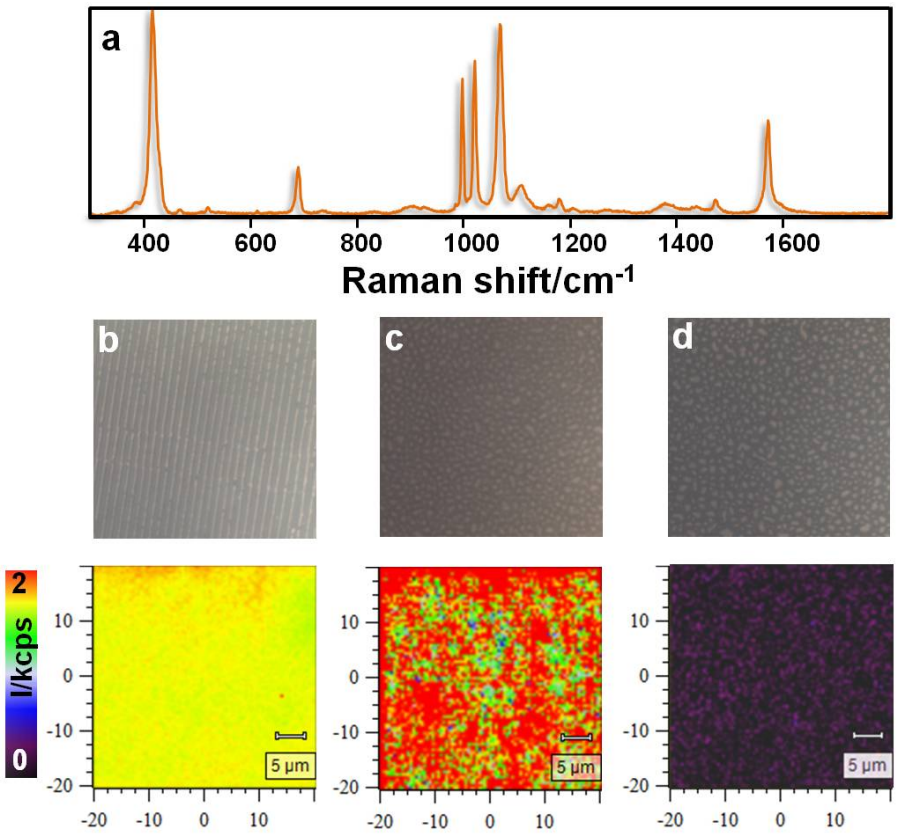

Figure 5-4 (a) SERS spectrum of BT on the AuNS-PNIPAM line patterned film. Optical and Raman maps (1073 cm^{-1}) over extended areas (40 × 40 µm, step size 1 µm) on (b) AuNS-PNIPAM line patterned, (c) AuNS-PNIPAM monolayered, and (d) AuNP@PNIPAM monolayered films.

Besides the previously mentioned role of the PNIPAM shell to act as a separation layer between the individual Au nanostars and thus avoiding the deactivation of the field enhancement at their tips,[34] the PNIPAM shell could be used as an effective molecular trap for hydrophobic analytes. In order to do that, the ability of the composite AuNS-PNIPAM particles to trap and analyze potential pollutants in the air was demonstrated by exposing the organized lines to an atmosphere containing traces of pyrene. Pyrene is formed during combustion of organic matter; thus to promote its dispersion into the gas phase, the patterned film together with a film of bare nanostars and an ethanolic solution containing pyrene were placed in a vacuum oven at 150 °C for 10 min. After exposure, both samples, the PNIPAM-coated and the uncoated one, were analyzed by SERS. Figure 5-5 shows the obtained experimental spectra for both samples, PNIPAM-coated stars (red) and bare Au stars (black). This experiment reveals the vibrational SERS pattern of pyrene when PNIPAM was used (red). This spectrum correlates well with the Raman spectrum of the solid,[14] which is characterized by vibrational modes at 1627, 1601, 1557, 1440, and 1398 cm^{-1} due to the ring stretchings, 1241 cm^{-1} CCH in plane deformation and

the 601 and 413 cm^{-1} CCH out of plane deformations. Notably, when the bare nanostars were used (black), the spectrum only shows very weak signals of pyrene because it is not retained on the gold surface, thus corroborating the effectiveness of PNIPAM shells as molecular traps for hydrophobic analytes.

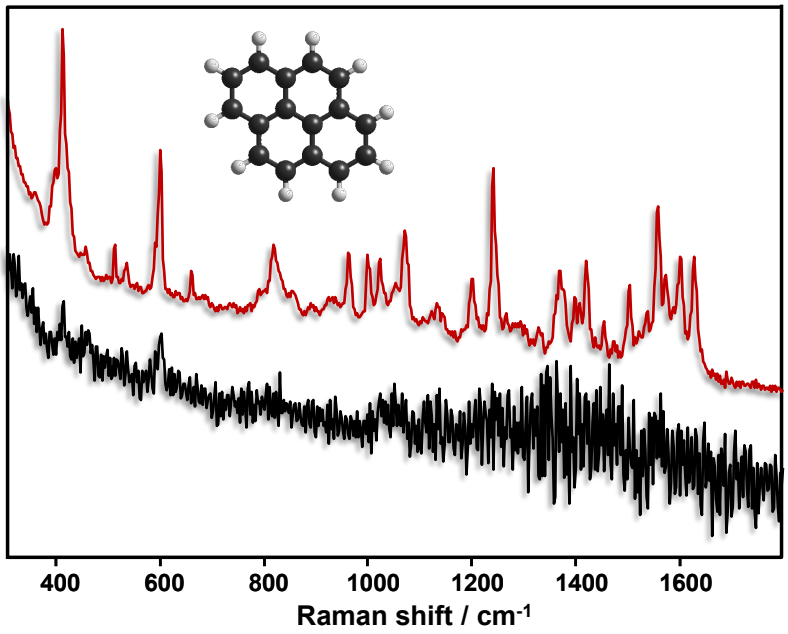

Figure 5-5 SERS spectra of pyrene from the gas phase on the AuNS-PNIPAM line patterned film (red) and on a film of bare AuNS (black)

5.4 Conclusion

In summary, here we demonstrate the possibility of generating 2D structured arrays of PNIPAM-coated nanostars extend over square centimeters via the wrinkle-assisted assembly in order to create a new, versatile SERS platform suitable for gas phase sensing. Also the optical properties and enhancing activity are characterized. In addition, trapping efficient for gas phase pollutants is demonstrated with the detection of pyrene, a well-known polyaromatic hydrocarbon. We anticipate that these materials will be a key technology in the development of highly efficient advanced air- or gas-sensing devices with environmental, industrial, and homeland security applications.

Aknowledgements

The authors would like to thank Carmen Kunert for helping during TEM characterization. This work was funded by the Spanish Ministerio de Ciencia e

Innovación (CTQ2011-23167) and by the German Science Foundation within SFB 840, TP B5.

References

1. Nie, S. M.; Emery, S. R. *Science*, **1997**, 275, 1102-1106.
2. Kneipp, K.; Wang, Y.; Kneipp, H.; Perelman, L. T.; Itzkan, I.; Dasari, R.; Feld, M. S. *Physical Review Letters*, **1997**, 78, 1667-1670.
3. Alvarez-Puebla, R.; Liz-Marzan, L. M.; Javier Garcia de Abajo, F. *Journal of Physical Chemistry Letters*, **2010**, 1, 2428-2434.
4. Pazos-Perez, N.; Borke, T.; Andreeva, D. V.; Alvarez-Puebla, R. A. *Nanoscale*, **2011**, 3, 3265-3268.
5. Le Ru, E. C.; Etchegoin, P. G. *Journal of Chemical Physics*, **2009**, 130.
6. De Jesus, M. A.; Giesfeldt, K. S.; Oran, J. M.; Abu-Hatab, N. A.; Lavrik, N. V.; Sepaniak, M. J. *Applied Spectroscopy*, **2005**, 59, 1501-1508.
7. Camden, J. P.; Dieringer, J. A.; Zhao, J.; Van Duyne, R. P. *Accounts of Chemical Research*, **2008**, 41, 1653-1661.
8. Zhang, X.; Zhao, J.; Whitney, A. V.; Elam, J. W.; Van Duyne, R. P. *Journal of the American Chemical Society*, **2006**, 128, 10304-10309.
9. Lu, C.; Moehwald, H.; Fery, A. *Soft Matter*, **2007**, 3, 1530-1536.
10. Pazos-Perez, N.; Ni, W.; Schweikart, A.; Alvarez-Puebla, R. A.; Fery, A.; Liz-Marzan, L. M. *Chemical Science*, **2010**, 1, 174-178.
11. Schweikart, A.; Pazos-Perez, N.; Alvarez-Puebla, R. A.; Fery, A. *Soft Matter*, **2011**, 7, 4093-4100.
12. Alvarez-Puebla, R. A.; Liz-Marzan, L. M. *Chemical Society Reviews*, **2012**, 41, 43-51.
13. Jones, C. L.; Bantz, K. C.; Haynes, C. L. *Analytical and Bioanalytical Chemistry*, **2009**, 394, 303-311.
14. Guerrini, L.; Garcia-Ramos, J. V.; Domingo, C.; Sanchez-Cortes, S. *Analytical Chemistry*, **2009**, 81, 1418-1425.
15. Leyton, P.; Cordova, I.; Lizama-Vergara, P. A.; Gomez-Jeria, J. S.; Aliaga, A. E.; Campos-Vallette, M. M.; Clavijo, E.; Garcia-Ramos, J. V.; Sanchez-Cortes, S. *Vibrational Spectroscopy*, **2008**, 46, 77-81.
16. Xie, Y.; Wang, X.; Han, X.; Xue, X.; Ji, W.; Qi, Z.; Liu, J.; Zhao, B.; Ozaki, Y. *Analyst*, **2010**, 135, 1389-1394.
17. Alvarez-Puebla, R. A.; Contreras-Caceres, R.; Pastoriza-Santos, I.; Perez-Juste, J.; Liz-Marzan, L. M. *Angewandte Chemie-International Edition*, **2009**, 48, 138-143.
18. Contreras-Caceres, R.; Abade-Cela, S.; Guardia-Giros, P.; Fernandez-Barbero, A.; Perez-Juste, J.; Alvarez-Puebla, R. A.; Liz-Marzan, L. M. *Langmuir*, **2011**, 27, 4520-4525.
19. Fernandez-Lopez, C.; Perez-Balado, C.; Perez-Juste, J.; Pastoriza-Santos, I.; de Lera, A. R.; Liz-Marzan, L. M. *Soft Matter*, **2012**, 8, 4165-4170.
20. Song, H.-M.; Wei, Q.; Ong, Q. K.; Wei, A. *Acs Nano*, **2010**, 4, 5163-5173.

21. Wei, Q.; Song, H.-M.; Leonov, A. P.; Hale, J. A.; Oh, D.; Ong, Q. K.; Ritchie, K.; Wei, A. *Journal of the American Chemical Society*, **2009**, 131, 9728-9734.
22. Pazos-Perez, N.; Rodriguez-Gonzalez, B.; Hilgendorff, M.; Giersig, M.; Liz-Marzan, L. M. *Journal of Materials Chemistry*, **2010**, 20, 61-64.
23. Fales, A. M.; Yuan, H.; Vo-Dinh, T. *Langmuir*, **2011**, 27, 12186-12190.
24. Hao, F.; Nehl, C. L.; Hafner, J. H.; Nordlander, P. *Nano Letters*, **2007**, 7, 729-732.
25. Pazos-Perez, N.; Barbosa, S.; Rodriguez-Lorenzo, L.; Aldeanueva-Potel, P.; Perez-Juste, J.; Pastoriza-Santos, I.; Alvarez-Puebla, R. A.; Liz-Marzan, L. M. *Journal of Physical Chemistry Letters*, **2010**, 1, 24-27.
26. Rodriguez-Lorenzo, L.; Alvarez-Puebla, R. A.; Pastoriza-Santos, I.; Mazzucco, S.; Stephan, O.; Kociak, M.; Liz-Marzan, L. M.; Javier Garcia de Abajo, F. *Journal of the American Chemical Society*, **2009**, 131, 4616-+.
27. Khoury, C. G.; Vo-Dinh, T. *Journal of Physical Chemistry C*, **2008**, 112, 18849-18859.
28. Kneipp, J.; Kneipp, H.; Kneipp, K. *Chemical Society Reviews*, **2008**, 37, 1052-1060.
29. Rodriguez-Lorenzo, L.; Alvarez-Puebla, R. A.; Javier Garcia de Abajo, F.; Liz-Marzan, L. M. *Journal of Physical Chemistry C*, **2010**, 114, 7336-7340.
30. Karg, M.; Jaber, S.; Hellweg, T.; Mulvaney, P. *Langmuir*, **2011**, 27, 820-827.
31. Enustun, B. V.; Turkevich, J. *Journal of the American Chemical Society*, **1963**, 85, 3317-&.
32. Horn, A.; Hiltl, S.; Fery, A.; Boeker, A. *Small*, **2010**, 6, 2122-2125.
33. Müller, M.; Karg, M.; Fortini, A.; Hellweg, T.; Fery, A. *Nanoscale*, **2012**, 4, 2491-2499.
34. Aldeanueva-Potel, P.; Carbo-Argibay, E.; Pazos-Perez, N.; Barbosa, S.; Pastoriza-Santos, I.; Alvarez-Puebla, R. A.; Liz-Marzan, L. M. *Chemphyschem*, **2012**, 13, 2561-2565.

6 Plasmonic Library Based on Substrate-Supported Gradientiel Plasmonic Arrays

Mareen Müller,[a] Christian Kuttner,[a] Tobias A. F. König,[a,b] Vladimir V. Tsukruk,[b] Stephan Förster,[c] Matthias Karg,[c] and Andreas Fery[a]**

[a] Physical Chemistry II, University of Bayreuth, Universitätsstr. 30, 95447 Bayreuth, Germany

[b] School of Material Science and Engineering, Georgia Institute of Technology, Atlanta, Georgia 30332-0245, United States

[c] Physical Chemistry III, University of Bielefeld, Universitätsstr. 25, 33615 Bielefeld, Germany

* e-mail: Matthias.karg@uni-bayreuth.de

* e-mail: andreas.fery@uni-bayreuth.de

Published in *ACS Nano* **2014**, 8, 9410-9421

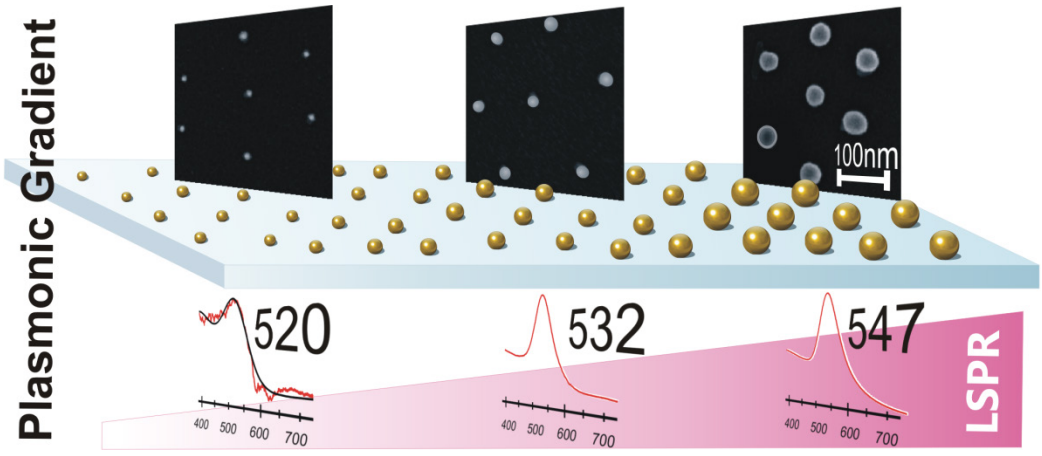

Abstract

We present a versatile approach to produce macroscopic, substrate-supported arrays of plasmonic nanoparticles with well-defined interparticle spacing and a continuous particle size gradient. The arrays thus present a "plasmonic library" of locally noncoupling plasmonic particles of different sizes, which can serve as a platform for future combinatorial screening of size effects. The structures were prepared by substrate assembly of gold-core/ poly(N-isopropylacrylamide)-shell particles and subsequent postmodification. Coupling of the localized surface plasmon resonance (LSPR) could be avoided since the polymer shell separates the encapsulated gold cores. To produce a particle array with a broad range of well-defined but laterally distinguishable particle sizes, the substrate was dip-coated in a growth solution, which resulted in an overgrowth of the gold cores controlled by the local exposure time. The kinetics was quantitatively analyzed and found to be diffusion rate controlled, allowing for precise tuning of particle size by adjusting the withdrawal speed. We determined the kinetics of the overgrowth process, investigated the LSPRs along the gradient by UV-Vis extinction spectroscopy, and compared the spectroscopic results to the predictions from Mie theory, indicating the absence of local interparticle coupling. We finally discuss potential applications of these substrate-supported plasmonic particle libraries and perspectives toward extending the concept from size to composition variation and screening of plasmonic coupling effects.

6.1 Introduction

The interaction of light with metal nanoparticles leads to the appearance of localized surface plasmon resonances (LSPRs), *i.e.*, the collective oscillation of the conduction electrons at a specific energy. The scattering and absorption cross-section as well as the frequency of the plasmon oscillation depend directly on the particle composition, size, shape, and surrounding effects.[1, 2]

The fascinating scattering and absorption properties gained metal nanoparticles a broad interest from a fundamental point of view but also for applications in the field of sensing,[3-7] subwavelength optical components,[8-12] light harvesting in photovoltaic devices,[13-15] and electrode materials.[16] Such applications require tailored optical properties. Thus, adjusting particle size and shape become essential. Consequently many

approaches for the synthesis of size and shape-controlled metal nanoparticles have been presented in the literature, ranging from procedures of the reduction of the metal salt in solution to seed-mediated growth on a substrate.[17-24] Indeed, accurate control of particle growth kinetics was established for a number of synthesis routes, such that size-monodisperse gold and silver nanoparticles are available as building blocks for plasmonic assemblies.[25, 26] However, even if well-defined particles can be synthesized, choosing the optimum particle size for the applications mentioned above is a highly challenging task. First, purely theoretical predictions on the ideal particle size for a specific task are difficult. For example surface enhanced Raman scattering (SERS) from single nanoparticles shows a complex size dependence.[27] As another example, the ideal particle size of metal nanoparticles to be used as scattering centers in photovoltaic devices is difficult to estimate due to the strong absorptive losses.[28] As well, the catalytic activity of nanoparticles shows a highly complex size and composition dependence. Second, particles are typically used in a substrate supported form, and hence their optical properties differ from the ones in solution.

Consequently experimental screening studies of substrate-supported nanoparticles of variable size are inevitable for finding the optimal size for particular tasks. For such screening studies, ideally, a library of particles with different size should be immobilized on specific positions of a substrate, such that combinatorial screening of properties under identical conditions is possible. At the same time, interparticle coupling has to be avoided, since coupling results in a complex alteration of LSPR properties.

In this work we present the first realization of such a "plasmonic library". We take advantage of diffusion rate controlled preparation of spherical and highly monodisperse gold particles with distinct particle sizes that are immobilized on a substrate in a way that avoids interparticle plasmonic coupling. Our colloidal building blocks were gold-core/poly(N-isopropylacrylamide)-shell (PNIPAM) particles.[29] These particles were deposited on glass substrates by spin-coating in order to prepare a homogeneous monolayer of gold nanoparticles of 9-15 nm in diameter. Due to the polymeric shell, the gold cores were well separated with interparticle distances on the order of 200 nm. Consequently, agglomeration of the particles and hence plasmon resonance coupling are avoided and a constant particle density is ensured. In addition the particles can be fixed to the substrate, which allows for wet-chemical post-treatment. Larger particle sizes were achieved by seeded growth of the adsorbed particles with a growth solution containing surfactant, $HAuCl_4$, and ascorbic acid. Instead of focusing on a particular

particle size, we prepared a uniaxial gradient of particle sizes on substrates with extraordinarily large macroscopic dimensions. The gradient was achieved using a dip-coating procedure. The immersion time of the substrate in the growing solution determined the reaction time. Thus, a direct investigation of particle growth in terms of particle size as a function of time is accessible. Our system shows diffusion-limited growth, which allows the exact size adjustment, but also size predictions become possible. Furthermore, we observe neither Ostwald ripening nor secondary nucleation.
Due to the continuous gradient in particle size, the prepared substrates show a gradient in plasmonic properties, too. The optical properties were investigated by UV-Vis spectroscopy, and the results were compared to theoretical predictions from Mie theory.[30] Since the particle monolayer has a constant particle density independent of the position on the large substrate, the optical changes along the particle gradient are caused solely by the changes in particle size. The presented approach is fast, cost-effective, and versatile in terms of accessible particle sizes. Since the interparticle distance is determined by the thickness of the PNIPAM shell, larger or smaller separations are achievable through tuning the polymer thickness.[31] This will for example allow for single-particle spectroscopy and sensing studies and the effective screening of the particle performance.

6.2 Experimental

Materials

All chemicals were purchased from Sigma-Aldrich unless mentioned differently: Gold(III) chloride, $HAuCl_4$ $3H_2O$ (≥99.9%), cetylmethylammonium bromide (CTAB; ≥99.9%), ascorbic acid (≥99.9), *N*-isopropylacrylamide (NIPAM; 97%), *N,N´*-methylenebis(acrylamide) (BIS; ≥99.5%; Fluka), potassium peroxodisulfate (≥99.0%; Fluka), trisodium citrate dihydrate (≥99%), sodium dodecyl sulfate (SDS; ≥99.0%), and 3-butenylamine hydrochloride (BA; 97.0%) were used as received without any further purification. Water was purified using a Milli-Q system (Millipore). The final resistivity was 18 MΩcm.

6.2.1 *Synthesis of Gold-Core/PNIPAM-Shell Particles*

Au-core/PNIPAM shell particles were prepared as previously reported.[29] Briefly the core/shell particles were synthesized in two steps: Gold nanoparticles of 9-15 nm in

diameter were prepared by the well-known citrate reduction protocol of Turkevich and Enüstün.[20] A 500 mL amount of an aqueous solution of $HAuCl_4$ ($[Au^{3+}]$ = 0.5 mM) was heated until heavy boiling. Then 25 mL of a 1 wt % aqueous trisodium citrate dihydrate solution was added quickly during strong stirring with a magnetic stirrer. After 15 min, the deep-red gold nanoparticle dispersion was allowed to cool to room temperature. The gold particles were then functionalized by the dropwise addition of 3 mL of an aqueous SDS solution ([SDS] = 0.624 mM) and 20 min later by the addition of 0.98 mL of an ethanolic BA solution ([BA] = 2.88 mM). The particles were cleaned and concentrated using centrifugation at 1400 rcf. Several centrifugation steps were necessary to separate the majority of particles from the dispersions. The residues were collected and mixed, leading to a gold nanoparticle stock solution with a concentration of $[Au_0]$ = 0.011 mM. The as-prepared functionalized gold nanoparticles were encapsulated in poly(*N*-isopropylacrylamide) shells using free-radical precipitation polymerization. A 791 mg amount of the monomer NIPAM and 161 mg of the cross-linker BIS were dissolved in 200 mL of water in a 250 mL three-neck round bottom flask. The clear solution was heated to 70 °C and purged with nitrogen. After 15 min of equilibration time, 5 mL of the as-prepared functionalized gold nanoparticle stock solution ($[Au_0]$ = 0.011 mM) was added dropwise. The polymerization was initiated by the rapid addition of 4 mg of potassium peroxodisulfate dissolved in 1 mL of water. The reaction was allowed to proceed for 2 h under continuous stirring with a magnetic stirrer. The core/shell particles were cleaned by repeated centrifugation/redispersion steps. The final residues were collected, redispersed in approximately 15 mL of water, and freeze-dried.

6.2.2 *Substrate Preparation*

Microscopy glass slides (Fisher Scientific, Premium microscope slides 12-544-4) were cleaned by using an RCA-1 solution of $NH_4OH/H_2O_2/H_2O$ in the ratio 1 : 1 : 5 at 80 °C for 20 min.[32] The cleaned glass slide was placed on the spincoater (model P6700, Specialty Coating Systems Inc.) and was coated with a 1 wt% solution of Au-PNIPAM particles, which were deposited by using a ramp of 20 s from 0 to 500 rpm, 20 s from 500 to 1000 rpm, and kept at this speed for 90 s. Both sides of the glass slide were coated. To fix the monolayer on the substrate, the slide was heated by a heat gun for 1 min at 200 °C. For the overgrowth of the 15 nm gold cores the substrate was dipped into a growing solution at 100 mm/min and pulled out with decreasing speed (see SI 3) using a dip-

coater (DC/D/LM, KSV Instruments). The growth solution was prepared by slowly adding 416.8 μL of 0.1 M $HAuCl_4$ under vigorous stirring to 100 mL of 0.1 M CTAB, and after 5 min 588 μL of a fresh solution of 0.1 M ascorbic acid was added dropwise under vigorous stirring. Finally the substrate was washed by immersing it twice in Milli-Q water at 29 °C first for 20 min then for 19 h. The optical properties of the plasmonic substrate were investigated by UV-Vis extinction spectroscopy. To investigate the gold-core dimensions, the PNIPAM shell was removed by heat treatment, following the procedure of Jaber et al. under a nitrogen atmosphere.[31]

Simulation. Classical Mie theory[30] is an exact solution of Maxwell's equations that was applied to model the optical response of Au particles in different media. Extinction cross sections of ideal spherical particles were calculated by a code implementation based on C. Mätzler[33] following the formulations of Bohren and Huffman.[2] We modified the code to allow for screening of the LSPR by variation of the optical constants of the surrounding medium. For the optical constants of gold we applied a fitting of the experimental data by Johnson and Christy[34] (six coefficients, RMS error = 0.211).

Characterization. UV-Vis spectra were taken with a Specord 250 Plus from Analytik Jena. To determine the particle diameter, AFM height images were recorded in intermittent contact mode with a Nanoscope V from Bruker. The height of the particles was determined by cross-section analysis using the program WSxM 5.0 from Nanotec Electronica S.L. The SEM pictures were made with a LEO 1530 VP Gemini from Zeiss operating at 2 kV, and the sample was sputtered with 1.3 nm of Pt. The initial gold nanoparticle cores as well as the initial Au-core/PNIPAM-shell particles were analyzed by TEM using a FEI TF 20 transmission electron microscope operated with an acceleration voltage of 200 kV. Samples were prepared by drop-casting of dilute aqueous dispersions on carbon-coated copper grids (400 mesh). The hydrodynamic dimensions of the Au-core/PNIPAM-shell particles were determined by dynamic light scattering (DLS). DLS measurements were conducted with a standard goniometer setup (ALV, Langen, Germany). Measurements were performed at a constant scattering angle of 60°. We used a HeNe laser (JDSU, USA) with 632.8 nm and a maximum output power of 35 mW as the light source. The sample temperature was regulated by a heat-controlled toluene refractive index matching/ temperature bath. Multiple intensitytime autocorrelation functions were recorded and analyzed by inverse Laplace transformation using the CONTIN algorithm.

6.3 Results and Discussion

The basis of our substrate-supported plasmonic arrays are gold-core/poly(*N*-isopropylacrylamide)-shell particles. These inorganic/organic hybrid particles were synthesized in two steps. First the gold cores were synthesized *via* the method of Turkevich and Enüstün[20] (Figure 6-1a) and afterward encapsulated in a PNIPAM network by free-radical precipitation polymerization Figure 6-1b). The diameter of gold cores (prior encapsulation) was measured with TEM and found to be 15.4 ± 1.6 nm. The corresponding UV-Vis extinction spectra can be found in SI 1 in the Supporting Information.

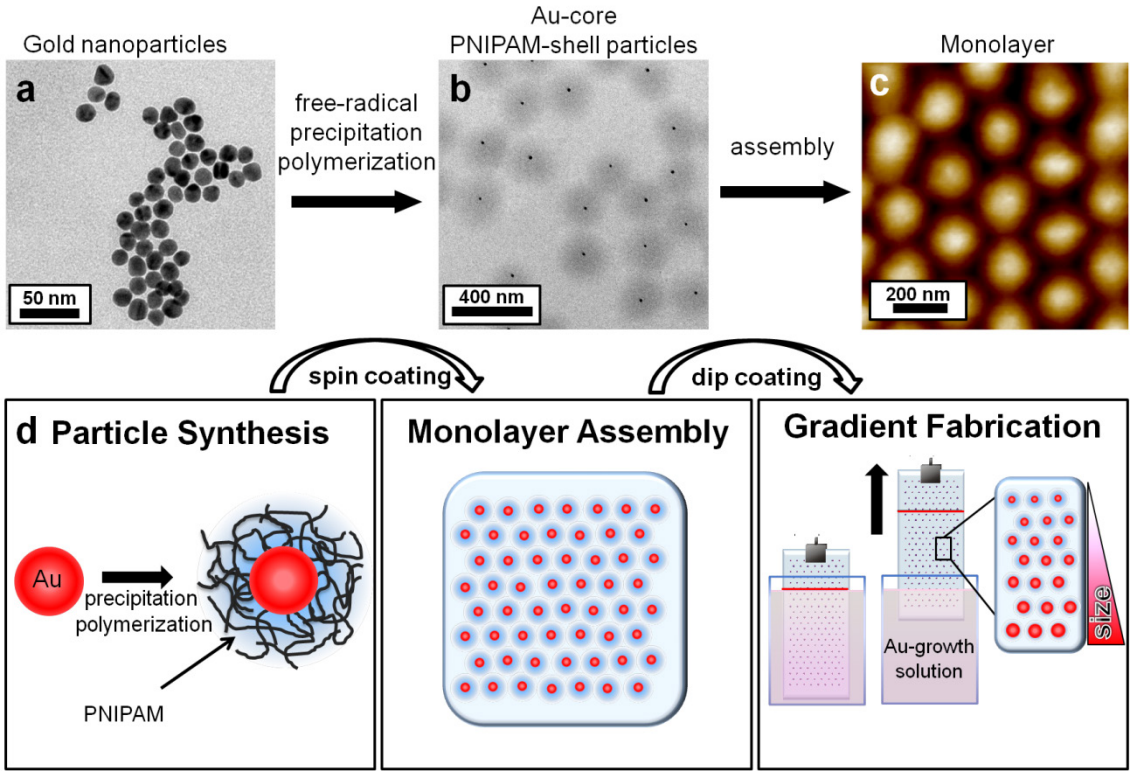

Figure 6-1 TEM images of (a) the Au cores prior to polymer encapsulation and of (b) the Au-core/PNIPAM-shell particles. The shell is visible as the dark gray corona around the gold cores. (c) AFM height image of a monolayer of the core/shell particles deposited on glass by spin-coating. (d) Depiction of the gradient fabrication: First the core/shell particles were synthesized. Second the particles were deposited on glass substrate via spin-coating. In the last step the substrate was mounted on a dip coater and immersed in an Au growth solution and pulled out.

Figure 6-1d depicts how the surface coatings with a gradient in plasmonic properties were prepared. After the particle synthesis a monolayer of well-separated gold nanoparticles was produced by spin-coating of the gold-core/PNIPAM-shell particles onto glass substrates. This deposition results in a close-packed monolayer of particles, which has locally hexagonally close-packed structures. Due to the PNIPAM shell, a well defined separation of the gold cores is achieved.[31] Thus, plasmonic coupling between the

gold cores by aggregate formation can be avoided.[35] Our selfassembly approach *via* spin-coating of the gold-core/ hydrogel-shell particles differs from recent works reported in the literature, which focus on systems with plasmonic coupling. These assemblies utilize small interparticle distances, which can be achieved by short spacers such as polymer ligands,[36,37] DNA,[38] or polymeric spacers combined with Langmuir-Blodgett techniques.[39,40] A representative AFM image of the spin-coated monolayer is presented in Figure 6-1c and in SI 2 of the Supporting Information. The radial distribution function of SI 4 shows five distinct peaks, which emphasizes also the quality of the monolayer. In the last step the gradient in particle size was created by *in situ* overgrowth of the deposited colloids. Before the overgrowth the particles were physically immobilized on the substrates by short thermal treatment for the following modification. In order to change the gold particle dimensions of the adsorbed Au-PNIPAM particles, a gold growing solution containing CTAB, $HAuCl_4$, and a weak reducing agent (ascorbic acid) was used. To produce a gradient in core size, and therefore in plasmonic properties, the sample was mounted on a dip-coater. The glass slide with the particle monolayer was fully immersed into the gold growing solution. The substrate was pulled out immediately with decreasing speed. In order to create substrates with a well-defined distribution of nanoparticle sizes and consequently well-defined localized plasmonic properties, the kinetics of nanoparticle growth has to be considered when choosing the dipping protocol. The dipping experiment is performed under a massive excess of gold ions in solution, such that nanoparticle growth is not affected by depletion of the gold ions in the course of the experiment. As well, secondary nucleation is not observed. As a consequence, the number of particles remains constant throughout the experiment, and only the radius of the assembled gold cores increases. The growth kinetics for post-modification of Au-core/PNIPAM-shell particles in solution has not been quantitatively investigated yet. Studies on the catalytic performance of gold nanoparticles encapsulated in crosslinked PNIPAM networks show that diffusion of reactants is hindered inside the PNIPAM network as compared to free diffusion in water.[41] The authors have also found that the diffusion rate decreases with increasing cross-linker content. In addition, surpassing the volume phase transition temperature the diffusion becomes significantly slower due to the collapse of the microgel shell. Hence we expect that the growth of gold nanoparticle cores inside PNIPAM should be limited by diffusion and significantly slowed due to the polymer shell as compared to bare nanoparticles in solution. For a diffusion-limited process, we expect nonlinear growth kinetics with a decrease in radial

growth with time (in the simplest case a square-root time dependence). Thus, in order to compensate for the expected nonlinear growth kinetics and arrive at a continuous variation of particle diameter across the substrates, we varied the dipping speed of the samples accordingly. The applied dip-coating ramp for withdrawal is depicted in the histogram presented in SI 3, illustrating a fast withdrawal speed at the beginning and a deceleration throughout the experiment. Following this growth procedure the particles on the top part of the substrate leave the growing solution first, and particles deposited at the bottom have the longest exposure time in the growing solution. The solid red line in the photograph shown in Figure 6-2c displays the maximum immersion depths. The differences in exposure time lead to a continuous increase of core diameters from top (position A) to bottom (position P).

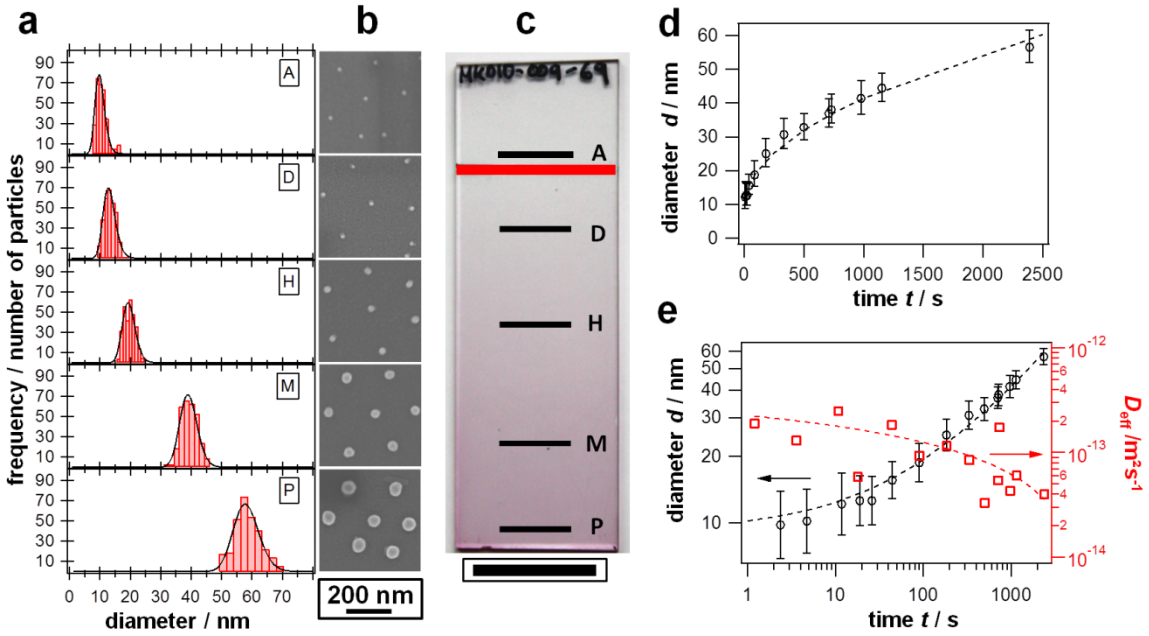

Figure 6-2 Particle size investigation along the gradient: (a) Histograms of the particle size for five different positions on the substrate (details for all 16 spots can be found in Figure 6-5) with diameter increasing from top to bottom (positions A to P) and (b) corresponding SEM images. (c) Photograph illustrating the macroscopic appearance of the glass slide, where the color gradient is attributed to the increasing particle size from position A (smallest gold cores, not overgrown) to P (largest, overgrown gold cores). The black lines indicate the positions on the substrate. The red line marks the maximum immersion depth. The scale bar is 2 cm. (d) Growth kinetics evaluated by AFM. (e) Effective diffusion coefficient (D_{eff}) evaluated by incremental regression of the change in size using Eq 1. Dashed curves are guides to the eye.

To investigate the gold-core diameter, we performed atomic force microscopy (AFM) at 16 positions on the substrate (see Figure 6-5 for a complete overview of particle sizes for all positions). The z-resolution of AFM is very reliable from the subnanometer to the micrometer regime and therefore suitable for size investigations of the experimental diameter range.[42] Before the AFM images were recorded, the polymer shell was removed by thermal treatment at 550 °C. This is necessary in order to be able to analyze only the

dimensions of the gold cores. Since this step influences the spectroscopic properties, it was carried out after the spectroscopic characterization reported later. For each position on the substrate, 300 particle cross sections of particles with a circularity larger than 0.85 were analyzed. The results of five individual positions are shown in Figure 6-2a (see Figure 6-5 for a complete data set). In order to determine the mean diameter at each position, we applied log-normal fits to account for slight deviations from normal distributions (see Figure 6-2a and 5). From the results the increase in diameter from 9.2 (+4.9/-4.5) nm to 56.6 (+3.9/-2.7) nm from position A to P is clearly visible, which results in an average size increase of 0.77±0.05 nm/mm. The diameter obtained from AFM at position A, where no overgrowth happened (not immersed in the growing solution), is slightly smaller than what we obtained from TEM measurements. This was also observed in ref [31]. Considering the error for both measurement techniques, AFM and TEM, the particle sizes are in the same range. The SEM pictures presented in Figure 6-2b show the particles at the corresponding positions without the shell (after thermal treatment). The size increase along the gradient is clearly visible. The images also prove the position stability, because the particles have not aggregated during the overgrowth. They are still assembled in a hexagonal fashion and well separated from each other. The period of the hexagonal arrangement of particles was analyzed by a radial distribution function (RDF), from which the average nearest neighbor distance between the centers of gold cores and the quality of the monolayer can be determined (see Supporting Information SI 4). As expected, the RDF exhibited an average intercore separation of 233 nm, which is in good agreement with the hydrodynamic diameter (253 nm, DLS) of the core shell particles. Interparticle coupling comes into account when the gap between the two particles is less than 2.5 times the particle diameter.[43] Consequently, we can neglect the interparticle coupling because the expected minimum gap between the particles is still about 3.2 times the particle diameter when the system reaches its maximum particle size of 56.6 nm. The SEM images also reveal the high quality of our growth procedure, since no additional particles appeared on the substrate, and hence secondary nucleation is completely avoided. The evolution of the particle diameter as a function of the exposure time allowed for a quantitative analysis of the growth kinetics. Figure 6-2d displays the increase in diameter with time as obtained by AFM. As expected for a diffusion-limited process, the increase in size slows over time.[44] From the evolution of the particle size the effective diffusion coefficient (D_{eff}) can be evaluated based on Fick's first law of diffusion: We consider that a known amount of seed particles

with initial radius r_0 is introduced into a supersaturated solution containing a concentration c of Au^+ ions, at t = 0. The seed particles (r_0 = 4.6 nm, AFM) are much larger than the Au^+ ionic species (r_{Au^+} = 0.137 nm).[45] Furthermore, we assume that (a) the seed particles are immobilized on the substrate and thus do not aggregate, (b) no nucleation occurs during the seeded growth process, and (c) particle growth may be viewed in terms of the reduction of the Au^+ ions to Au^0 on the surfaces of stationary seed particles. The flux J of Au^+ ions toward the seed particles is given by Fick's first law of diffusion: $J = -D\partial_r c$. At steady state, the number of ions per time reaching the seed particle is $j = 4\pi r^2 |J|$. Assuming a linear concentration gradient of Au^+ between the seed particle surface and the bulk solution, we have have $j = 4\pi\ D\ r\ c_\infty$, where c_∞ is the concentration of Au^+ ions at infinite distance from the central seed particle of radius r. Assuming that only the Au^+ ions undergo Brownian motion, characterized by a diffusion coefficient D, then the volume growth of the seed particles is $\partial_t V = V_{Au0}\ j$, *i.e.*, the ion flux j times the partial volume increase per ion (r_{Au0} = 0.144 nm),[45] which yields $r\ dr = V_{Au0}\ D\ c_\infty\ dt$. If the aqueous phase is of infinite volume, then the bulk concentration of Au^+ is constant (c_∞ = 0.413 mM) and the equation may be integrated with the initial condition $r(t = 0) = r_0$ to give the effective diffusion constant D_{eff}. Thus the resulting growth law is $r^2 - r_0^2 = 2\ V_{Au0}\ D_{eff}\ c_\infty\ t$ which can be solved for D_{eff}:

$$D_{\mathrm{eff}} = \frac{r^2 - r_0^2}{2V_{\mathrm{Au0}} c_\infty t} \qquad (1)$$

Considering the complete growth process, we found a mean effective diffusion coefficient of $\langle D_{eff} \rangle = 6\ 10^{-14}$ $m^2 s^{-1}$, *i.e.* about 3 orders of magnitude slower than for CTAB-stabilized Au^+ ions in aqueous solution. The Stokes-Einstein relation predicts a $D_{Au+@CTAB} = 9 \cdot 10^{-11}$ $m^2 s^{-1}$ for Au^+ species complexed with stabilizing CTAB micelles of 6 nm diameter[46] in pure water at 30 °C. This deceleration could easily be due to the slower diffusion inside the PNIPAM shell, which acts as a diffusion barrier, and the confined location of the seeds at the surface (not being distributed homogeneously in the bulk solution).

The high data density of our AFM study also allows for an incremental investigation of the diffusion evolution and thus the time-dependent character of D_{eff}. The time evolution of the effective diffusion coefficient is depicted in Figure 6-2e for each individual growth step. Apparently, D_{eff} decreases almost a full order of magnitude throughout the growth process. The double logarithmic plot in Figure 6-2e indicates the direct correlation of the diffusion deceleration and the size increase of Au cores inside the PNIPAM shells.

We believe that the deceleration of the diffusion is related to morphological changes of the PNIPAM shell. Upon growth, the expansion of the core particle may induce a compression of the PNIPAM network in close vicinity. Thus, a more compact polymer interphase[47-49] would hinder the transport from bulk solution through the shell membrane. A detailed investigation of this rather complex behavior will be addressed in a future study and is not in the scope of the present work.

The impact of the change in core size on the plasmonic properties of the particle monolayer is already visible with the bare eye. In the photograph shown in Figure 6-2c a pronounced color gradient from nearly transparent to deep purple from the top to the bottom of the substrate is visible. This impression on the macroscopic scale is an indication of the gradient in Au-core size. The increase in color intensity can be attributed to a rise in extinction of the overgrown gold cores. This size gradient leads to position-dependent plasmonic properties.[50] For the optical characterization we performed UV-Vis extinction spectroscopy. The results for five positions along the gradient are presented in Figure 6-3a and b (for all 16 positions see Figure 6-5). The measured area was 7x1.3 mm² due to the beam size of the UV-Vis spectrometer. The rectangular illumination spot was set perpendicular to the dipping direction (indicated by the black lines in the photograph of Figure 6-2c). Since the measurement averages over a large population of nanoparticles, a local ensemble average of spectroscopic properties is analyzed.

In order to determine the influence of the refractive index of the surrounding medium on the plasmonic properties, we performed extinction measurements against air as well as in water. The spectra were taken in 4 mm steps starting from the original, not overgrown particles, at position A. The extinction spectrum recorded at position A is noisy, and only a week signal was detected. In order to determine the LSPR position, we fitted the spectra with a Lorentzian function (black dotted line). Going from the original particles at position A along the gradient to position P, two effects are visible: On one hand the extinction rises by 2 orders of magnitude, and on the other hand the LSPR position shifts to higher wavelengths. The higher extinction cross-section can be attributed to the increase in gold particle diameter only since the number of particles per area is constant throughout the whole substrate. In other words, the measurement at position A analyzes nearly the same number of gold particles as the measurement at position P. The increase in extinction with increasing particle size can be attributed to an increase in the volume fraction of gold in the plasmonic coating. The volume fraction of

the plasmonic particles in a hypothetical layer of gold can be calculated using the gold core diameter as the height of the plasmonic layer and the surface coverage, *i.e.*, the number of gold particles per area. The results are presented in SI 5A, where the volume fraction is plotted against the logarithm of the immersion time. The volume fraction increases by 2 orders of magnitude from $7.4 \cdot 10^{-4}$ from the original core diameter at position A to $2.6 \cdot 10^{-2}$ at position P. Apart from an increase in extinction along the gradient, the LSPR peak is red-shifted due to the increasing diameter. The red shift of the LSPR with increasing particle size is well known from literature.[51, 52]

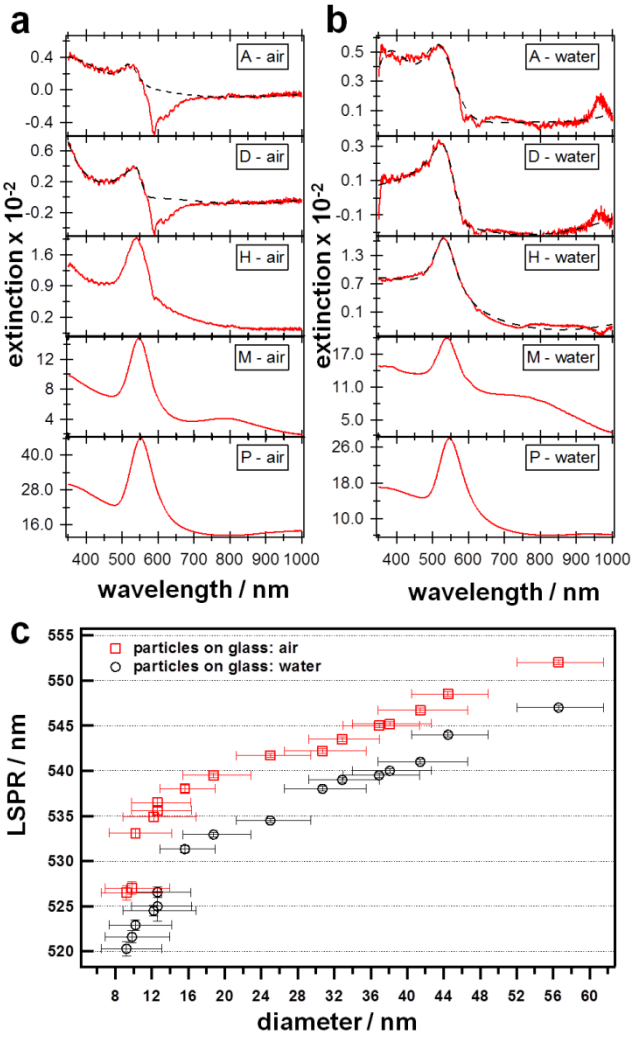

Figure 6-3 Results from UV-Vis extinction spectroscopy of the gradient substrate. Spectra recorded at five different positions measured (a) against air and (b) in water (details for all 16 spots can be found in Figure 5). (c) LSPR positions as a function of core diameter (determined from AFM).

A shoulder at higher wavelength can be observed in the extinction spectra of larger core dimensions shown in Figure 6-3a and b. This shoulder shifts to higher wavelength for increasing particle diameter (see Figure 6-5 going from position I to P). We attribute the

shoulder to particles with nonspherical morphology such as rods, plates, or triangles.[53] These morphologies can evolve during the particle growth due to the polycrystallinity of the used seed gold particles. It is well known that the growth velocity of plasmonic nanoparticles is different on different facets, which can lead to anisotropic particles.[17] For larger growing times, also elongation of the rods is supported, which leads to a red shift of the longitudinal peak of the rods; visible as the shoulder; to the near-infrared.[54] In the graph shown in SI 5B the percentage of nonspherical objects is plotted against the logarithm of the immersion time. For this analysis at least 1400 particles were counted at each position on the substrate. Particles were considered as spherical when the circularity was higher than 0.85. The ratio of nonspherical gold cores is not higher than 12%, and therefore their spectral contribution is not dominating the extinction spectra. The LSPR intensities and positions are mainly influenced by the varying diameter and the refractive index of the surrounding medium.

Since we measured the UV-Vis spectra at similar positions as we determined the particle size, we can plot the LSPR position as a function of the core diameter (Figure 6-3c). With increasing particle diameter the LSPR peak is shifted toward larger wavelengths. An overall LSPR shift of 25.5 nm for measurements against air and 26.7 nm in water is observed when the spectra measured at positions A and P are directly compared. The LSPR could be shifted further toward red upon additional size increases, which was not in our interest. Larger core sizes would inherently result in a broadening of the LSPR extinction peak associated with a loss in absorption and a strong increase in scattering.[27] Surprisingly the LSPR at each sample position measured against air is red-shifted compared to the LSPR in water. This behavior is different from that expected for bare gold particles, where a red shift is observed as the refraction index of the surrounding medium changes from n = 1.00 (air) to 1.33 (water).

The presence of the polymer shell, however, explains these findings.[55, 56] For measurements against air the PNIPAM shell is in a dried state. The local polymer density in close vicinity of the gold nanoparticle cores is expected to be much higher compared to the swollen state (sample immersed in water). Therefore, the local refractive index is rather high, although the substrate-surrounding medium is air. In contrast, if the substrate is immersed in water, the PNIPAM shell swells for temperatures below the volume phase transition temperature. In this case, the polymer density in the vicinity of the gold cores decreases significantly. Thus, the local refractive index at 25 °C will be close to the value of water due to the rather large degree of swelling. Although the

swelling of the polymer shell will not be as high for particles adsorbed on a substrate as compared to a particle dispersed in aqueous solution, the water content in the shell can easily reach 80-90%.[52] Hence, the PNIPAM shell plays a crucial role in the position of the LSPR peak. Recently Tagliazucchi et al. showed in theoretical studies that the LSPR peak always shifts to higher wavelengths when the solvent for a gold-core/PNIPAM-shell particle is changed from good to bad.[57] This observation implies that the red shift expected due to increasing polymer density always overcomes the blue shift expected from decreasing layer thickness.

In our case the increase of the local refractive index is triggered by water evaporation during drying and therefore an increase in the polymer fraction in close proximity around the core. Even if a residual water content of 12% is considered in the PNIPAM network for the dried state, which is known in the literature,[58, 59] the overall polymer fraction in the dried state has to be higher around the core than for the water-immersed particles. Since the refractive index of the polymer PNIPAM (n = 1.52) is higher than that of water, the red shift in our experimental results can be explained.[57, 58] To quantitatively describe the red shift of the plasmon resonance wavelength λ_{LSPR} with increasing gold nanoparticle diameter d, we used the allometric power law as follows:

$$\lambda_{LSPR} = kd^{a} + c$$

with k as amplitude, a as scaling exponent, and c as offset constant (for values, see Supporting Information Table SI 1). To the best of our knowledge, the power law description is a more precise description of the plasmonic red shift compared to an earlier publication, which used an exponential power law with respect to a bulk refractive index change.[60] Figure 6-4a shows the approximation of the allometric power law to the Mie theory modeling at different surrounding refractive indices.[61] The plasmon resonance positions for the used particle diameters and four different refractive indices ranging from air (n = 1.00) to glass (n = 1.52) are determined.

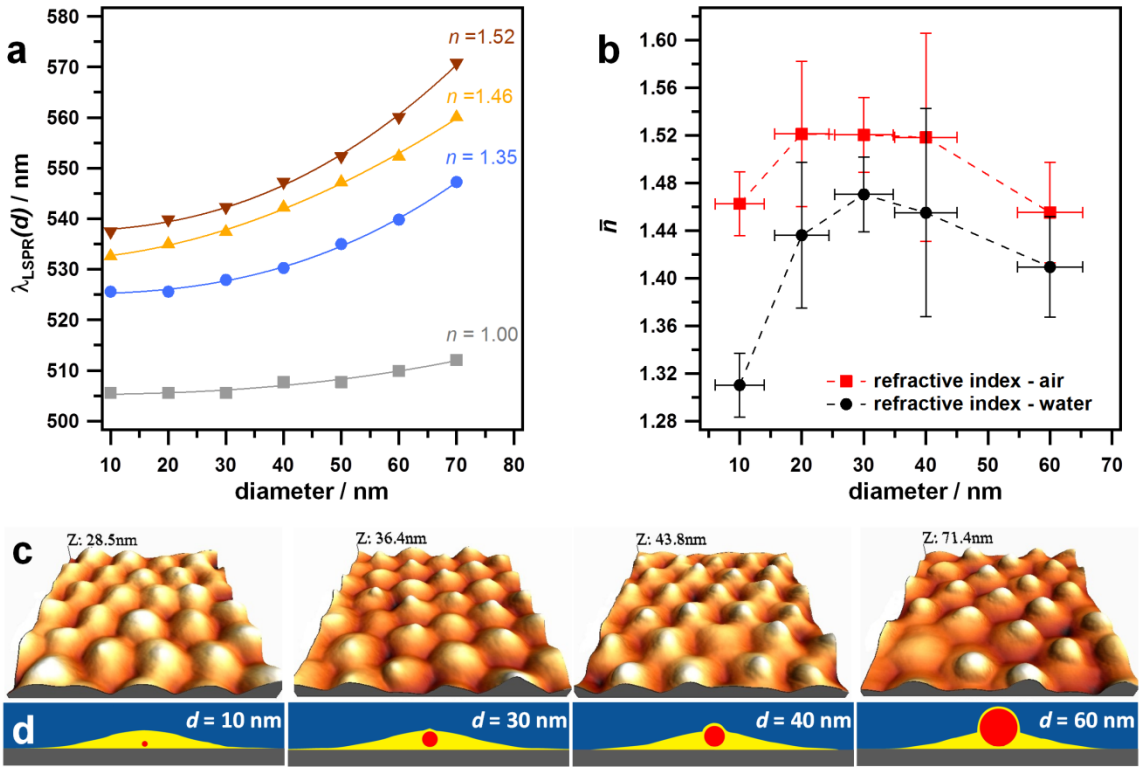

Figure 6-4 (a) Plasmonic resonance (LSPR) modeled by Mie theory for different surroundings and gold-core diameters. (b) Apparent surrounding refractive index as expected from the experimental LSPR position observed against air and in water. (c) 3D representations of AFM height images in air for increasing core diameters of the core/shell particles from left to right. (d) Schematic depictions of the cross sections through gold-core (red)/PNIPAM-shell (yellow) particles for different core diameters deposited on a glass substrate (gray); blue is the surrounding medium.

Consequently, from theoretical modeling we expect a concave shape of the plasmon resonance with increasing diameter (Figure 6-4a), but our experimental observation shows a convex characteristic (Figure 6-3c). To discuss this discrepancy, we derived a so-called average surrounding refractive index $\bar{n}$ from the plasmon resonance position for a specific particle diameter. An intermediate parabola fitting step is necessary to obtain the surrounding refractive index from the plasmon resonance position at a given particle diameter. This intermediate step is described in more detail in the Supporting Information 6.5.7. The results of the performed analysis are shown in Figure 6-4b. In the swollen state the refractive index changes between 1.31±0.03 and 1.47±0.03. In the dried state the refractive index lies between 1.45±0.04 and 1.52±0.06 and therefore 0.08±0.04 higher compared to the swollen state. These findings reveal indeed that the increased polymer density in the dried state leads to a larger refractive index in the nanoparticle vicinity as compared to the water-swollen system. However, the calculation of the average refractive index based on the experimental LSPR positions considers a homogeneous refractive index environment. Due to the finite size of the PNIPAM shell,

potential density inhomogenieties in the shell, and the presence of the glass substrate (n = 1.52) underneath the adsorbed particles, the real refractive index environment is more complex. This complexity can be seen in the AFM height profiles in Figure 6-4c and is also illustrated in the scheme in Figure 6-4d. The AFM images were recorded at four sample positions with different core sizes increasing from left to right. For small-core dimensions (approximately 15 nm) the core is nearly invisible (image on the far left in Figure 6-4c). On growing the gold particle inside the network (approximately to 60 nm), the core becomes more and more pronounced. Finally, the gold particle is clearly visible and the PNIPAM shell is stretched around the core particle (fried egg shape). The scheme in Figure 6-4d depicts cross sections of the system and represents the possible structural morphology of the deposited particles. Despite the complex setup, the plasmonic shift can be described sufficiently enough by an average surrounding refractive index model based on Mie theory.[2, 30] This simple theoretical model makes the plasmonic array a valuable template for versatile applications (post-treatment) such as reversible tuning of the plasmonic resonances over the full visible spectrum,[62] high sensitivity sensing,[63] and precise mapping of the plasmonic hybridization model.[64, 65]

Figure 6-5 summarizes the extremely precise control of both particle size and LSPR that can be achieved by the approach. The large size of the gradient on the centimeter scale together with the very sharp local size distributions allow screening sizes and plasmonic properties in 16 equidistant steps between positions A and P indicated in Figure 6-2c. Thus, the requirements for a plasmonic library are met for the first time.

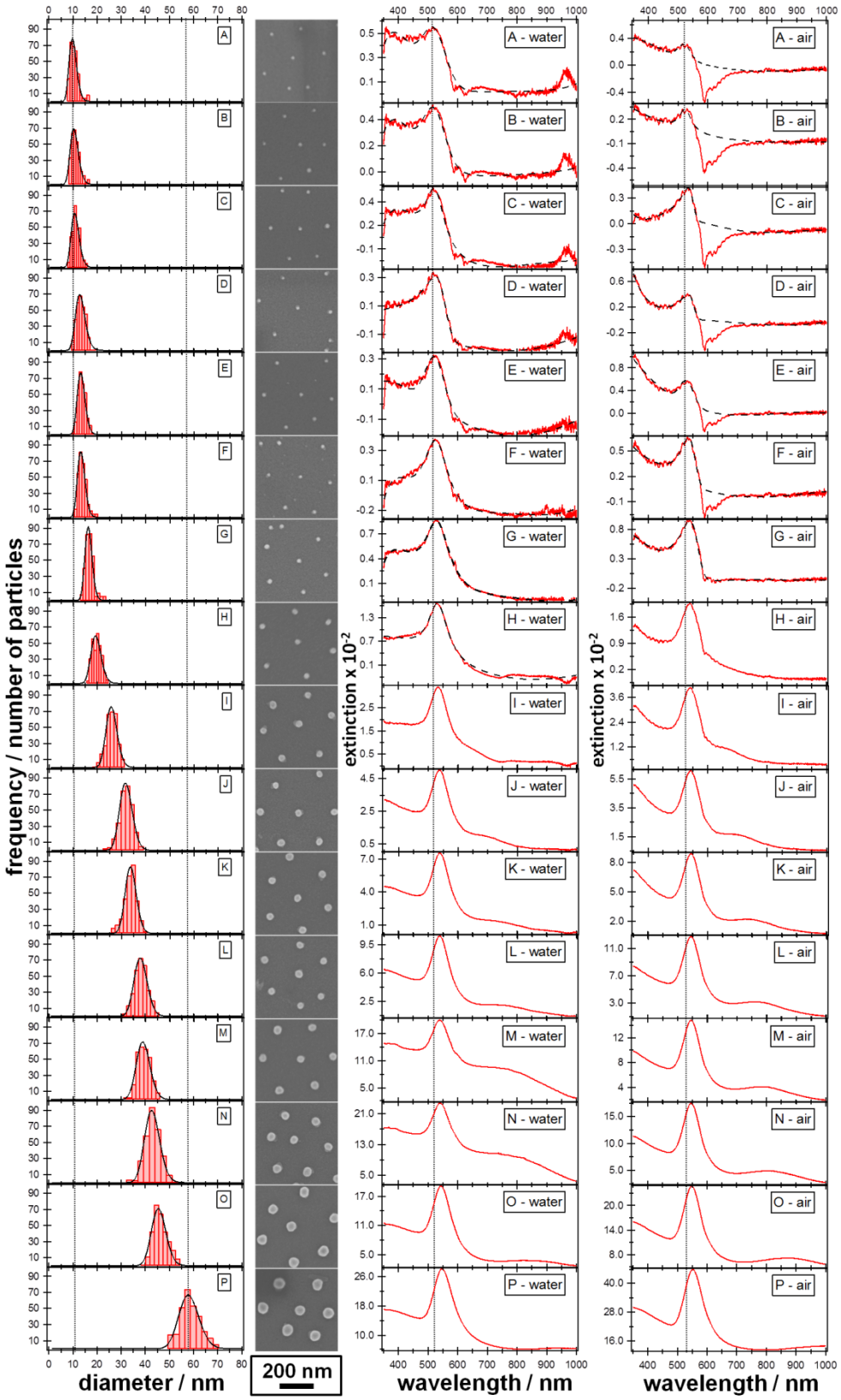

Figure 6-5 The first column depicts histograms of all measured spots of the substrate A to P with increasing particle diameter. The second column shows the corresponding SEM images. Columns 3 and 4 show the related UV-Vis extinction spectra in water and in air.

6.4 Conclusion

We have presented a novel approach for the formation of macroscopic, substrate-supported arrays of plasmonic nanoparticles with well-defined interparticle spacing and a continuous particle size gradient. The core/shell nature of the individual particles allowed for creating monolayers with interparticle distances for which local interparticle coupling effects are negligible. At the same time, post-modification of the substrate-supported arrays allowed for a controlled overgrowth of the plasmonic cores, such that the local particle size could be varied in a gradient fashion between 9.2 and 56.6 nm, which allows for spectroscopic analysis of 16 intermediate sizes. The local particle sizes were determined and the kinetics of core growth could be explained by a diffusion-limited growth model. The hydrogel shell resulted in a reduction of effective diffusion coefficients to to $<D_{eff}> = 6\ 10^{-14}\ m^2s^{-1}$, which allowed for a precise control of particle sizes. Spectroscopic investigations and comparison to generalized Mie theory show that local plasmon resonance frequency and extinction are systematically varying over a broad range, while the single-particle character of the LSPR is maintained. Consequently, the substrates present a "plasmonic library" that can serve as a substrate for screening experiments to find the optimum size for specific applications.

The concept presented here can be generalized in various ways. First, rather than choosing the hydrogel shell such that interparticle coupling is avoided, thinner hydrogel shells will allow for precisely following the onset of interparticle coupling and systematic studies of near-field effects such as hot-spot formation. In this respect the temperature-sensitive character of the PNIPAM shell can also be exploited to achieve temperature-controlled interparticle separations, especially if a cross-linking step and delamination from the substrate are added, as for example realized in 3D superstructures.[66, 67] Second, the overgrowth protocol can be expanded toward probing not only size effects but also compositional effects. First experiments demonstrate successful overgrowth of gold cores with a second metal, opening an additional dimension for combinatorial screening. This will be especially of interest for screening catalytic nanoparticle properties as well as the impact of overgrowth on changes in LSPR characteristics.

6.5 Supporting Information

6.5.1 *SI 1: UV-Vis extinction spectra of gold cores and core/shell particles in aqueous solution*

The optical properties of the gold cores prior to encapsulation and the core/shell hybrid particles were analyzed by UV-Vis extinction spectroscopy (Figure S1). The black spectrum was measured for the gold cores before the polymer encapsulation. The position of the localized surface plasmon resonance is 518 nm. The red spectrum corresponds to the core/shell colloids. In comparison to the spectrum of the gold cores, the extinction for the core/shell particles shows a pronounced increase in extinction toward lower wavelength. This can be attributed to scattering from the rather large PNIPAM shell.1 In addition the LSPR is slightly shifted to higher wavelength due to the increased refractive index, i.e., PNIPAM has a higher refractive index than water.

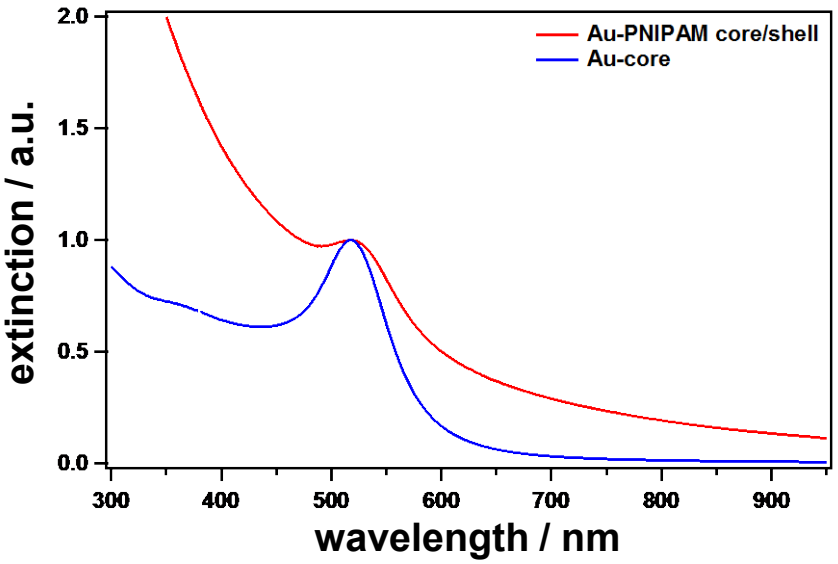

SI 1 UV-Vis extinction spectra of citrate stabilized gold (black line) and goldcore/PNIPAM-shell particles (red line) measured in water at 25 °C.

6.5.2 *SI 2: AFM height profile of particle monolayer*

Representative image of the spin-coated Au-core/PNIPAM-shell monolayer before overgrowth of the gold cores.

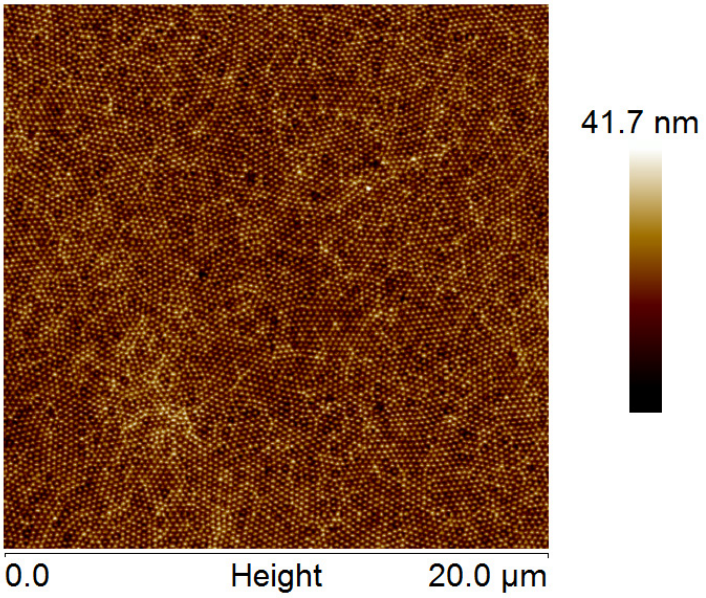

SI 2 AFM height image of a representative Au-core/PNIPAM-shell monolayer after spincoating.

6.5.3 *SI 3: Details on withdrawal process*

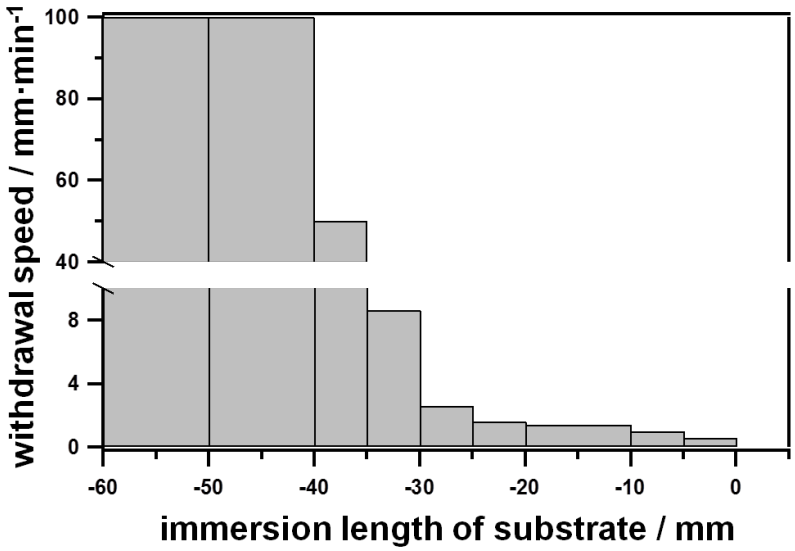

SI 3 Histogram of the used withdrawal ramp. The substrate is immersed 60 mm and afterward pulled out with decreasing speed.

6.5.4 *SI 4: Evaluation of the mean interparticle distance from the radial distribution function*

To calculate the average interparticle distance between the assembled gold cores a radial distribution function was generated using a SEM image with 1633 particles on an area of 80 µm². The average center-to-center distance of the gold cores is 233 nm as determined from the first maximum of the radial distribution function. From the five distinct RDF peaks the high structural quality of the monolayer can be evaluated.

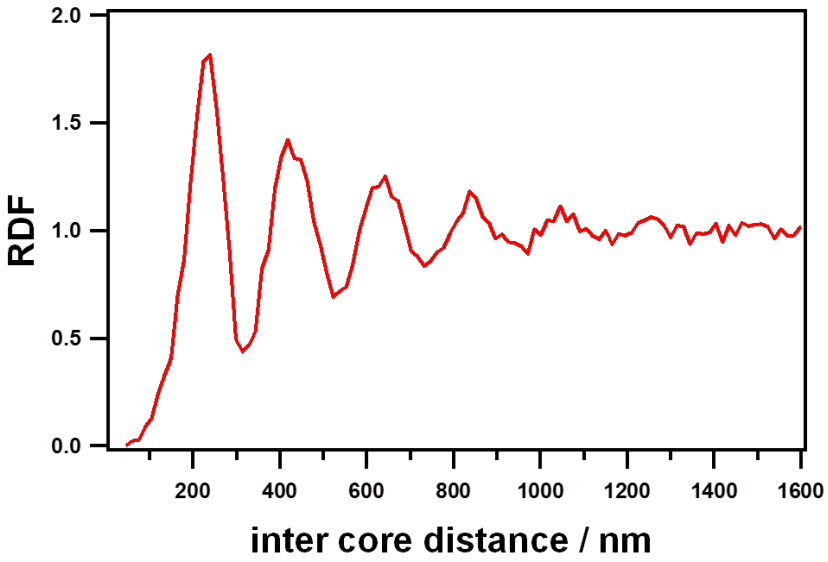

SI 4 Radial distribution function of Au-core/PNIPAM-shell particle monolayer assembled on a glass substrate.

6.5.5 *SI 5: Evaluation of the volume fraction of gold throughout the gradient*

Between position **B** and **G** of Figure SI5A the volume fraction is in the same range and the first position where an increase in the volume fraction is visible is at position **H**. This is related to the detection of a stronger UV-Vis signal and less noisy spectra. Figure S5B shows the amount of non-spherical objects for the positions on the substrate. We assumed particles with a circularity higher than 0.85 as spherical. At least 1400 particles were investigated per sample position. The number of non-spherical particles is increasing along the gradient and is 12% for the longest immersion times at position **P**.

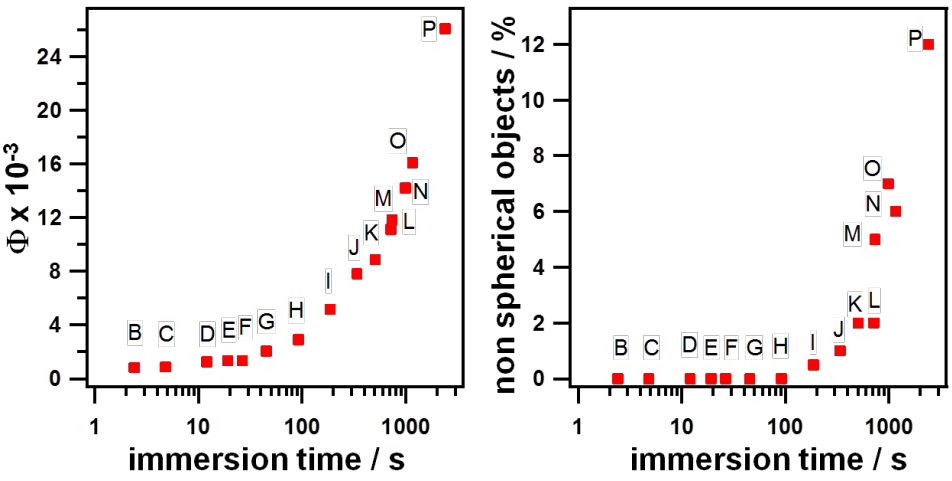

SI 5 A shows the increasing volume fraction of the gold cores in a hypothetical closed gold layer of the same height as the core diameter. B shows the amount of none spherical objects (circularity less than 0.85) for increasing exposure time in the growth solution.

6.5.6 *SI 6: Quantitative description of the red shift of the LSPR for different particle diameter by an allometric power law according to Mie theory*

To describe the shift of the plasmon resonance λ_{LSPR} for increasing particle diameter in different surroundings of refractive index n, we applied the following allometric power law:

$$\lambda_{LSPR} = kd^a + c$$

with k as amplitude, a as scaling exponent, c as offset constant, and R^2 as coefficient of determination. Table S1 summarizes the coefficients used in Figure 6-4.

Table SI 1 Summary of coefficients used to determine the LSPR shifts by Mie theory.

n	$k / nm^{(1-a)}$	a	c / nm	R^2
1.52	0.0019	2.30	537.6	0.998
1.46	0.0115	1.83	531.9	0.998
1.35	0.0005	2.25	525.1	0.998
1.00	0.0001	2.63	505.4	0.995

6.5.7 *SI 7: Determination of the average surrounding refractive index from Mie theory*

To obtain the average surrounding refractive index from the plasmonic resonance position at specific particle diameter, we made a parabolic fit to the LSPR position (equation, errors, and coefficient of determination are given in the inset of Figure SI 6), which we determined from Mie theory at different surrounding refractive indices.

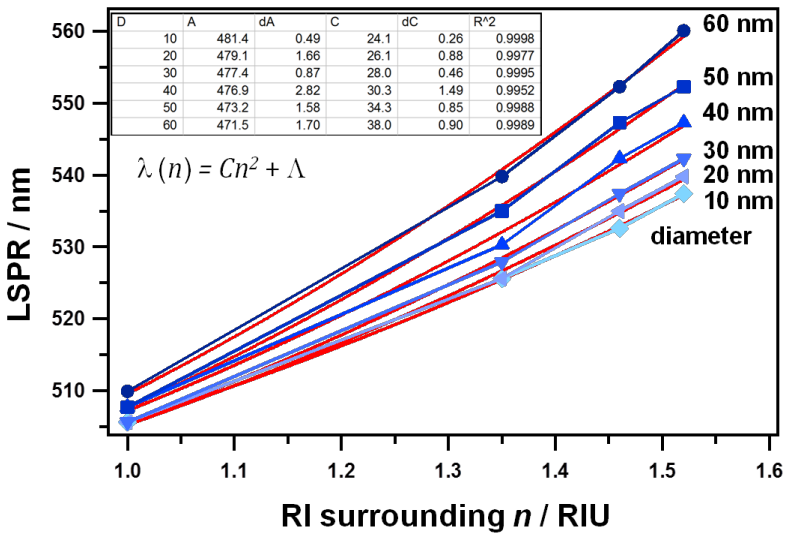

SI 6 LSPR red shift *versus* surrounding refractive index and parabolic fit (solid red lines) at different gold core diameter.

Acknowledgement

The authors thank Maximilian Seuß for help with particle size analysis in Igor Pro and Sebastian Koch and Martin Schieder for assistance with the thermal treatment for the shell removal of the particles. C.K. appreciates fruitful discussions with Wolfgang Häfner. This work was funded by the German Science Foundation within the SFB 840 and by the European Research Council under grant ERC-2012-StG 306686 (METAMECH: Template-assisted assembly of METAmaterials using MECHanical instabilities). M.K. acknowledges financial support from the Funds der Chemischen Industrie (FCI) through the Verband der Chemischen Industrie (VCI). Financial support from U.S. Department of Energy, Office of Basic Energy Sciences, Division of Materials Sciences and Engineering, under award DE-FG02-09ER46604 is gratefully acknowledged by T.A.F.K. and V.V.T.

References

1. Kreibig, U.; Vollmer, M. *Optical Properties of Metal Clusters*. Springer Verlag: Berlin, 1995.
2. Bohren, C., F; Huffmann, D., R. *Absorption and Scattering of Light by Small Particles*. Wiley: New York, 1983.
3. Szunerits, S.; Boukherroub, R. *Chemical Communications*, **2012**, 48, 8999-9010.
4. Willets, K. A.; Van Duyne, R. P. Localized surface plasmon resonance spectroscopy and sensing. In *Annual Review of Physical Chemistry*, 2007; Vol. 58, pp 267-297.
5. Anker, J. N.; Hall, W. P.; Lyandres, O.; Shah, N. C.; Zhao, J.; Van Duyne, R. P. *Nature Materials*, **2008**, 7, 442-453.
6. Rosi, N. L.; Mirkin, C. A. *Chemical Reviews*, **2005**, 105, 1547-1562.
7. Alvarez-Puebla, R. A.; Liz-Marzan, L. M. *Angewandte Chemie-International Edition*, **2012**, 51, 11214-11223.
8. Barnes, W. L.; Dereux, A.; Ebbesen, T. W. *Nature*, **2003**, 424, 824-830.
9. Oulton, R. F.; Sorger, V. J.; Zentgraf, T.; Ma, R.-M.; Gladden, C.; Dai, L.; Bartal, G.; Zhang, X. *Nature*, **2009**, 461, 629-632.
10. Engheta, N. *Science*, **2007**, 317, 1698-1702.
11. Maier, S. A.; Kik, P. G.; Atwater, H. A.; Meltzer, S.; Harel, E.; Koel, B. E.; Requicha, A. A. G. *Nature Materials*, **2003**, 2, 229-232.
12. Pendry, J. B.; Aubry, A.; Smith, D. R.; Maier, S. A. *Science*, **2012**, 337, 549-552.
13. Atwater, H. A.; Polman, A. *Nature Materials*, **2010**, 9, 205-213.
14. Brown, M. D.; Suteewong, T.; Kumar, R. S. S.; D'Innocenzo, V.; Petrozza, A.; Lee, M. M.; Wiesner, U.; Snaith, H. J. *Nano Letters*, **2011**, 11, 438-445.

15. Ding, I. K.; Zhu, J.; Cai, W.; Moon, S.-J.; Cai, N.; Wang, P.; Zakeeruddin, S. M.; Graetzel, M.; Brongersma, M. L.; Cui, Y.; McGehee, M. D. *Advanced Energy Materials*, **2011**, 1, 52-57.
16. Cheng, W. L.; Dong, S. J.; Wang, E. K. *Analytical Chemistry*, **2002**, 74, 3599-3604.
17. Grzelczak, M.; Perez-Juste, J.; Mulvaney, P.; Liz-Marzan, L. M. *Chemical Society Reviews*, **2008**, 37, 1783-1791.
18. Sau, T. K.; Rogach, A. L. *Advanced Materials*, **2010**, 22, 1781-1804.
19. Sardar, R.; Funston, A. M.; Mulvaney, P.; Murray, R. W. *Langmuir*, **2009**, 25, 13840-13851.
20. Enustun, B. V.; Turkevich, J. *Journal of the American Chemical Society*, **1963**, 85, 3317-&.
21. Jana, N. R.; Gearheart, L.; Murphy, C. J. *Langmuir*, **2001**, 17, 6782-6786.
22. Brust, M.; Walker, M.; Bethell, D.; Schiffrin, D. J.; Whyman, R. *Journal of the Chemical Society-Chemical Communications*, **1994**, 801-802.
23. Bastus, N. G.; Comenge, J.; Puntes, V. *Langmuir*, **2011**, 27, 11098-11105.
24. Cheng, W. L.; Dong, S. J.; Wang, E. K. *Langmuir*, **2002**, 18, 9947-9952.
25. Becker, J.; Schubert, O.; Sonnichsen, C. *Nano Letters*, **2007**, 7, 1664-1669.
26. Bullen, C.; Zijlstra, P.; Bakker, E.; Gu, M.; Raston, C. *Crystal Growth & Design*, **2011**, 11, 3375-3380.
27. Pazos-Perez, N.; Garcia de Abajo, F. J.; Fery, A.; Alvarez-Puebla, R. A. *Langmuir*, **2012**, 28, 8909-8914.
28. Mendes, M. J.; Morawiec, S.; Simone, F.; Priolo, F.; Crupi, I. *Nanoscale*, **2014**, 6, 4796-4805.
29. Karg, M.; Jaber, S.; Hellweg, T.; Mulvaney, P. *Langmuir*, **2011**, 27, 820-827.
30. Mie, G. *Annalen der Physik*, **1908**, 330, 377-445.
31. Jaber, S.; Karg, M.; Morfa, A.; Mulvaney, P. *Physical Chemistry Chemical Physics*, **2011**, 13, 5576-5578.
32. Kern, W.; Puotinen, D. A. *Rca Review*, **1970**, 31, 187-&.
33. Mältzer, C. MATLAP Functions for Mie Scattering and Absorbtion. Bern, **2012**; pp 1-20.
34. Johnson, P. B.; Christy, R. W. *Physical Review B*, **1972**, 6, 4370-4379.
35. Halas, N. J.; Lal, S.; Chang, W.-S.; Link, S.; Nordlander, P. *Chemical Reviews*, **2011**, 111, 3913-3961.
36. Ng, K. C.; Udagedara, I. B.; Rukhlenko, I. D.; Chen, Y.; Tang, Y.; Premaratne, M.; Cheng, W. *Acs Nano*, **2012**, 6, 925-934.
37. Klinkova, A.; Choueiri, R. M.; Kumacheva, E. *Chemical Society Reviews*, **2014**, 43, 3976-3991.
38. Cheng, W.; Campolongo, M. J.; Cha, J. J.; Tan, S. J.; Umbach, C. C.; Muller, D. A.; Luo, D. *Nature Materials*, **2009**, 8, 519-525.
39. Tao, A.; Sinsermsuksakul, P.; Yang, P. *Nature Nanotechnology*, **2007**, 2, 435-440.
40. Vogel, N.; Fernandez-Lopez, C.; Perez-Juste, J.; Liz-Marzan, L. M.; Landfester, K.; Weiss, C. K. *Langmuir*, **2012**, 28, 8985-8993.
41. Carregal-Romero, S.; Buurma, N. J.; Perez-Juste, J.; Liz-Marzan, L. M.; Herves, P. *Chemistry of Materials*, **2010**, 22, 3051-3059.

42. Moller, C.; Allen, M.; Elings, V.; Engel, A.; Muller, D. J. *Biophysical Journal*, **1999**, 77, 1150-1158.
43. Ghosh, S. K.; Pal, T. *Chemical Reviews*, **2007**, 107, 4797-4862.
44. Nong-Moon Hwang, J.-S. J. a. D.-K. L. Thermodynamics and Kinetics in the Synthesis of Monodisperse Nanoparticles. In *Thermodynamics - Fundamentals and Its Application in Science*, Morales-Rodriguez, R., Ed. 2012.
45. Aylward, G. H.; Findlay, T. *Datensammlung Chemie in SI Einheiten*. 3rd ed.; Wiley-VCH: 1999.
46. Park, K.; Koerner, H.; Vaia, R. A. *Nano Letters*, **2010**, 10, 1433-1439.
47. Kuttner, C.; Hanisch, A.; Schmalz, H.; Eder, M.; Schlaad, H.; Burgert, I.; Fery, A. *Acs Applied Materials & Interfaces*, **2013**, 5, 2469-2478.
48. Kuttner, C.; Maier, P. C.; Kunert, C.; Schlaad, H.; Fery, A. *Langmuir*, **2013**, 29, 16119-16126.
49. Kuttner, C.; Maier, P. C.; Kunert, C.; Schlaad, H.; Fery, A. *Langmuir*, **2013**, 29, 16119-16126.
50. Link, S.; El-Sayed, M. A. *Journal of Physical Chemistry B*, **1999**, 103, 4212-4217.
51. Liz-Marzan, L. M. *Langmuir*, **2006**, 22, 32-41.
52. Schmidt, S.; Zeiser, M.; Hellweg, T.; Duschl, C.; Fery, A.; Moehwald, H. *Advanced Functional Materials*, **2010**, 20, 3235-3243.
53. Murray, W. A.; Barnes, W. L. *Advanced Materials*, **2007**, 19, 3771-3782.
54. Vigderman, L.; Khanal, B. P.; Zubarev, E. R. *Advanced Materials*, **2012**, 24, 4811-4841.
55. Haes, A. J.; Zou, S. L.; Schatz, G. C.; Van Duyne, R. P. *Journal of Physical Chemistry B*, **2004**, 108, 6961-6968.
56. Miller, M. M.; Lazarides, A. A. *Journal of Physical Chemistry B*, **2005**, 109, 21556-21565.
57. Tagliazucchi, M.; Blaber, M. G.; Schatz, G. C.; Weiss, E. A.; Szleifert, I. *Acs Nano*, **2012**, 6, 8397-8406.
58. Reufer, M.; Dıaz-Leyva, P.; Lynch, I.; Scheffold, F. *Eur. Phys. J. E*, **2009**, 28, 165-171.
59. Pelton, R. *Journal of Colloid and Interface Science*, **2010**, 348, 673-674.
60. Jain, P. K.; El-Sayed, M. A. *Chemical Physics Letters*, **2010**, 487, 153-164.
61. Jain, P. K.; Lee, K. S.; El-Sayed, I. H.; El-Sayed, M. A. *Journal of Physical Chemistry B*, **2006**, 110, 7238-7248.
62. König, T. A. F.; Ledin, P. A.; Kerszulis, J.; Mahmoud, M. A.; El-Sayed, M. A.; Reynolds, J. R.; Tsukruk, V. V. *Acs Nano*, **2014**, 8, 6182-6192.
63. König, T.; Kodiyath, R.; Combs, Z. A.; Mahmoud, M. A.; El-Sayed, M. A.; Tsukruk, V. V. *Particle & Particle Systems Characterization*, **2014**, 31, 274-283.
64. Malak, S. T.; Koenig, T.; Near, R.; Combs, Z. A.; El-Sayed, M. A.; Tsukruk, V. V. *Journal of Physical Chemistry C*, **2014**, 118, 5453-5462.
65. König, T.; Tsukruk, V. V.; Santer, S. *Acs Applied Materials & Interfaces*, **2013**, 5, 6009-6016.
66. Karg, M.; Hellweg, T.; Mulvaney, P. *Advanced Functional Materials*, **2011**, 21, 4668-4676.

67. Chen, M.; Zhou, L.; Guan, Y.; Zhang, Y. *Angewandte Chemie-International Edition*, **2013**, 52, 9961-9965.

7 Perspectives - Producing a Plasmonic library on the single particle level

Unpublished work

7.1 Introduction

Plasmonic building blocks have been used for the construction of bottom up sensing devices, such as SERS or refractive index sensors and are promising candidates for optical wave guiding or efficiency enhancement in photovoltaic devices. The plasmonic building blocks for such devices are conventionally synthesized and characterized in wet chemical procedures. The manifold protocols allow tailoring the size, composition, and shape. However, the usage on a chip changes the environment from homogeneous to heterogeneous and therefore the optical properties. The particles experience the refractive index of the substrate on the one side and a gas or liquid on the other side. Precisely tailored LSPR properties can be lost after the deposition, due to refractive index changes, drying effects, aggregation, oxidation processes and so on. It is more convenient to deposited seed particles first and to apply a post-modification to adjust the plasmonic properties. For such a modification it is crucial to have control over the inter particle spacing. Additionally the position stability of the colloids has to be ensured during such a chemical treatment.

We showed in Chapter 6 how gold-core/PNIPAM-shell particles could be used to generate plasmonic gradient surfaces on a chip. The shell gave control of the inter core spacing, immobilized the particles on the surface and allowed the post-modification due to its permeability. The gradient in plasmonic properties from top to the bottom of one substrate allowed a fast screening of LSPR positions. The post-enlargement of the gold cores was done by immersing a microscopy slide covered with a monolayer of the core/shell particles into a gold growth solution, while the sample was withdrawn. This led to a gradient in gold core size and therefore to a plasmonic gradient. In general this technique enables the fast screening of the optical properties, which are dependent on size, geometry, or composition of the particles as a function of substrate and environment.

Nevertheless, for the development of screening substrates, libraries on a chip, combinatorial investigations, or monitoring catalytic activities[1, 2] a precise characterization of individual particles and/or a special patterning could be necessary. A powerful method for single metal particle investigation is dark field (DF) spectroscopy. The DF microscope enables the detection of metal nanoparticles down to 20 nm in diameter.[3] This is possible, due to the special DF illumination under a very high angle, so that just scattered light reaches the objective. On top, gold or silver colloids show a large scattering cross section.[4] Combining such a microscope with an image monochromator and a CCD camera makes the detection of the Rayleigh scattering spectra possible. This technique allows the plasmonic characterization of single gold or silver particles, due to the fact that their optical response is dominated by the strong LSPR.[5] The practical implementation and data evaluation is described in Ref. 6. Briefly, the microscope is used to illuminate the particles and the scattered light of the colloids is collected in the objective. Following the light is passed through the entrance slit of the spectrometer onto the monochromator and further to the back port of the spectrometer to the CCD. The monocromator can also be used as a mirror to find the region of interest in the image mode. If the monochromator is used as a grating, the light is dispersed horizontally according to its wavelengths. The CCD collects the intensity distribution and the software allows integration over the region of interest - the scattered light of the particle.

To collect the spectra of individual particles some requirements have to be fulfilled: the light that is collected and transferred to the spectrometer has to be just the light from the particle. That means the substrate has to be clean, because dust and other impurities scatter light as well as scratches in the surface. If such objects are close to the particle of interest undesired light is also captured and transferred to the spectrometer, which complicate or hinder the optical investigation. Furthermore, the metal colloids have to be well distributed. It is difficult to determine single particles from small clusters, which show different LSPR peaks due to plasmon coupling. That means the distance between the metal particles should be in the μm regime for a sufficient optical resolution. Often a highly diluted metal particle solution is spin coated on the substrate. To find suitable particles and spots the substrate is investigated with SEM prior to DF. This limits the usable substrate to conductive substrates like indium tin oxide (ITO). The next challenge is the recognition of the area of interest under the DF that can be done by retrieving noticeable landmarks. Another option is the etching of marks into the substrate with

focused ion beam[7] or the use of pre-labeled glass slides.[8] The single particle investigation in this way, is time consuming and unfavorable for any kind of statistic analysis.

A more device-oriented approach is the use of pre-patterned substrate, which allows a controlled deposition of the plasmonic colloids. The group of J. P. Spatz used e-beam lithography to etch holes into a photo resist. Gold salt precursor containing micelles were deposited in the grooves of these templates. The micelles that reside on the sacrificial resist layer were washed away with acetone so that just the ones in the holes remain. After plasma treatment, the gold salt is reduced and nanoparticles are formed.[9] A. P. Alivisatos *et al.* presented the deposition of Au nanoparticles in trenches of a patterned silicon substrate. The substrates were fabricated by lithography and the particles were deposited by capillary force assembly during solvent evaporation.[10] The drawback of these techniques is the recycling of the costly and elaborately fabricated substrates. Another access route to such substrates is replica molding of lithographically produced masters with PDMS. Once the master is designed, it can be reproduced many times. The capillary force assembly process can be adapted to PDMS systems, which was shown by C. Kuemin *et al.*[11] The benefit of such substrates is the transfer option to other surfaces. T. Kraus et al. showed such a transfer of Au particles surfaces[12], where PMMA was used as an adhesion promoter for the gold nanoparticles.

We present in this work the template assisted deposition of gold and silver-core/PNIPAM-shell particles from structured PDMS to glass substrates. The PDMS was replicated from lithographical produced silicon masters with micrometer dimensions. The core-shell particles were deposited into the trenches of the PDMS via spin coating and printed to glass *via* a wet transfer step.[13,14] The benefit of core/shell particles combined which such a template assisted method is the controlled deposition of small plasmonic particles in a patterned fashion individually. We investigated the quality of the transfer process for the Au and Ag-PNIPAM colloids with DF microscopy and compared these results with AFM height images. We recorded scattering spectra from single particles and clusters. The option of post-modification[13] of the core/shell particles on substrates[15] make these colloids interesting for high throughput screening devices, also on the single particle level.

7.2 Experimental

Materials

Gold(III) chloride trihydrate ($HAuCl_4 \times 3H_2O$), trisodium citrate dihydrate (≥99%), *N'N*-isopropylacrylamide (NIPAM; 97%) and butenylamine hydrochloride (BA), cetylmethylammonium bromide (CTAB; ≥99.9%), ascorbic acid (≥99.9), silver nitrate ($AgNO_3$; ≥99.0%) and sodium dodecyl sulfate (SDS; ≥99.0%) were purchased from Aldrich and used as received. Polydimethylsiloxane (PDMS) Sylgard (184) silicon elastomer, curing agent, and precursor were purchased from Dow Corning, USA. *N'N*-Methylenebisacrylamide (BIS ≥99.5%) was obtained from Fluka and 1H,1H,2H,2H-Perfluorodecyltrichlorosilane (96%) from Alfa Aesar. All experiments were carried out with deionized water using a Millipore Milli-Q system.

7.2.1 *Gold-core/PNIPAM-shell particles*

The gold-PNIPAM core shell particles were prepared according to the synthesis presented elsewhere.[16] Shortly first the spherical gold nanoparticles of about 15 nm in diameter were synthesized following the protocol of Turkevich and Enüstün.[17] This citrate stabilized particles were functionalized by the drop wise addition of an aqueous SDS solution ([SDS] = 0.624 mM) and 20 min later by the addition of 0.98 mL of an ethanolic BA solution ([BA] = 2.88 mM). The solution was cleaned and concentrated by centrifugation. The gold stock solution was used for the encapsulation with PNIPAM in a free-radical precipitation polymerization. A 500 mL aqueous solution containing 1.131 g of the monomer NIPAM and 231 mg of the cross-linker BIS were heated to 70 °C in a three-neck round bottom flask and purged with nitrogen. After 20 min, 8.871 mL of the Au-stock solution ([Au_0] = 0.011 mM) was added dropwise. Rapid addition of 10 mg of potassium peroxodisulfate dissolved in 1 mL of water initiated the polymerization. The reaction runs for 2 h under continuous stirring with a magnetic stirrer. The core/shell particles were cleaned by repeated centrifugation and redispersions steps. The cleaned particles were redispersed in approximately 15 mL water and freeze-dried. 100 mg were redispersed in 5 mL water for the seeded growth procedure. The core overgrowth was performed by adding 250 µL of the core/shell particles suspension to 15 mL of a gold growth solution. The growth solution was prepared by adding 75 µL of a 0.1 M $HAuCl_4$ slowly to 14.925 mL CTAB ([CTAB] = 0.05 M) under vigorous stirring. After the addition of the seed particles 717 µL of a freshly prepared solution of the reducing agent ascorbic

acid ([AA] = 10 mM) was added drop wise under vigorous stirring. The solution started to change the color from light pink to a deeper reddish pink. After 20 min, the reaction was finished and the particles cleaned by 5 centrifugation and redispersion steps. The final volume was 1 mL. The hydrodynamic diameter was determined with a zeta sizer (Zetasizer Nano-ZS Melbourne) and is D_h=211 nm. The core diameter was analyzed with TEM and is 35.8±8.8 nm.

7.2.2 *Silver-core/PNIPAM-shell particles*

For the synthesis of the Ag-PNIPAM particles, a multistep synthesis was applied. First 6.00 g of glycine and 3.64 g of CTAB were dissolved in 200 mL of MilliQ water at 35 °C. 1 mL of a concentrated dispersion of Au-PNIPAM with a core diameter of 15-20 nm (see section 7.2.1) was added to this solution after it cooled down to room temperature. Subsequent 16 mL of a 0.1 M NaOH solution was added under stirring. Than 9 mL of the reducing agent ascorbic acid (100 mM) was given to the reaction mixture. 13.1 mL of a freshly prepared solution of $AgNO_3$ (15 mM) was added quickly. The $AgNO_3$ solution was kept in the dark. After 2 min, another 655µL of the silver salt solution was injected. This step was repeated 20 times. The reaction mixture was kept stirring for another 20 min. The growing of the silver layer over the gold core was indicated by a color change from slight purple to a yellowish green. The particles were diluted to 50 mL and washed *via* centrifugation and redispersions steps. The centrifugation was done at 3740 rfc for 1 h. After two redispersion steps with water, two times with ethanol and again two times with water the final residue was diluted in 2 mL of water. The core size was determined by TEM measurements and is 103.9±9.5 nm. The hydrodynamic diameter was evaluated by DLS and is 336 nm.

7.2.3 *Master fabrication*

The masters were fabricated *via* E-beam lithography. First, a 200 nm layer of PMMA was spin cast on a silicon waver. Secondly, the structure was written in the PMMA layer by exposure to E-beam lithography. In the next step 30 nm chromium was evaporated on top. After the lift off of the PMMA a dry etching step using SF_6 (50 sccm) and C_4F_8 (30 sccm) with an etching rate of about 76 nm/min was applied. The chromium film was

removed by using a chromium cleaning solution. The master (1 x 1 cm) was cleaned for 20 min in ultra sound (US) bath in a surfactant (Mucasol) solution than 15 min US in ethanol, rinsed with water and cleaned for 15 min at 80° in RCA solution containing $NH_4OH/H_2O_2/H_2O$ in the ratio 1 : 1 : 5. After air-plasma treatment (Herrick PDC- 32G) for 10 min the master was silanized over the gas phase by placing it in a desiccator with perfluorodecyltrichlorosilane under vacuum over night. Excessive silane was washed by immersing the slide successively in toluenen, tetrahydrofuran, water and backwards to toluene and dried under nitrogen.

7.2.4 *Substrate preparation*

The silanized silicon master was used for replica molding with PDMS. Therefore, the PDMS prepolymer was mixed with the curing agent in a mass ration of 10:1, cast over the master and placed immediately in a desiccator for at least 15 m in to degas the PDMS as complete as possible. The PDMS was cured for 4h at 60 °C.

7.2.5 *Particle deposition*

The PDMS cut stamp (1 x 1 cm) was hydrophilized for 1 min in plasma (Plasma Technology Flecto 10 USB) directly before use and placed on a spin coater (Headway Research Inc. Photo-Resist Spinner). The aqueous particle suspension was placed on top of the stamp so that the whole stamp was covered with particle suspension. The substrate was accelerated with 200 rpm/s to 4000 rpm and kept at this speed for 80 sec. Immediately after particle deposition a second step of spin coating with water for Au-PNIPAM or CTAB (8mM) for Ag-PNIPAM was applied. After water / CTAB deposition on top of particle coated PDMS it was rotated with 500 rpm for 10 sec and subsequent accelerated with 175 rpm/s to 4000 rpm and kept at this speed for 100 sec. The particle deposition was performed *via* spin-release presented in Ref. [13]. The particle covered PDMS stamp was placed on top of a RCA cleaned glass slid wetted with 2 µL water. The stamp stayed in contact with the glass for 2h until the water was fully evaporated.

7.2.6 *Characterization*

The Au- and Ag-PNIPAM were optically analyzed by UV-Vis extinction spectroscopy using a Specord 250 plus (Analytic Jena). The core size was determined by transmission electron spectroscopy (ZEISS CEM 902) using copper grids with a 200 mesh size operating at a voltage of 80 kV. DLS measurements were performed with a standard goniometer setup (ALV, Langen, Germany). Measurements were done at a scattering angle of 60° and kept constant. We used a HeNe laser as light source from JDSU, USA with 632.8 nm and a maximum output power of 35 mW. The sample temperature was regulated and kept constant at 25 °C by a heat-controlled toluene refractive index matching/temperature bath. Multiple intensity time autocorrelation functions were recorded and analyzed by inverse Laplace transformation using the CONTIN algorithm. The PDMS stamps were characterized by atomic force microscopy using a Bruker Incon Dimension in tapping mode with cantilevers form Brucker (OTESPA-R3, 26 N/M). The optical investigation of the master, empty PDMS replicas, filled stamps and the transferred particles on glass were done with the reflectance dark field microscope Nikon Eclipse LV100D-U with a ThorLabs USB camera. For the dark field image of the Au-PNIPAM arrays a Nikon Eclipse TE-2000 microscope, a Nikon dark-field condenser (Dry, 0.95–0.80 NA) with a Plan Fluor ELWD 40/0.60 NA objective was used. The collected light was focused to the entrance slit of a MicroSpec 2150i imaging spectrometer with an attached TE-cooled CCD camera (PIXIS 1024 ACTON Princeton Instruments). For the investigation of the Ag-PNIPAM particles, a Nikon Eclipse Ti-U with a dark field condenser (Nicon Ti-DF, dry 0.95-0.80) and an S Plan Fluor 60x objective with a NA of 0.7 was used. The color images were recorded with a Nikon DS-Fi2 camera. The spectra were recorded with a Princton Instruments PIXIS256 CCD camera attached to a Princton Instruments Aceton SP2150 spectrometer and integrated over 60 seconds. The sample was mounted on an automated stage from Prior (pro SCAN III).

7.3 Results and discussion

The colloidal building blocks used for the array fabrication were gold and silver-core/poly(*N*-isopropylacrylamide)-shell particles. They were synthesized in a multiple step process. First, the gold cores were prepared after the well-known protocol of Turkevich and Enüstün[17] and functionalized with BA. The diameter of the gold cores was measured with TEM and lay between 10 and 15 nm, which is expected from the

Turkevich synthesis route. Secondly the encapsulation of the cores was done *via* a free radical precipitation polymerization of NIPAM in the presence of the cross linker BIS. The gold cores were subsequent enlarged and overgrown with silver to a diameter of 103.9±9.5 nm (see Figure 7-1a). The overall hydrodynamic diameter of this Ag-PNIPAM NPs was determined by DLS and was 336 nm. These particles were well suited for preliminary tests to investigate the feasibility of core/shell particles for DF spectroscopy, which was not shown so far. Silver with such large dimensions ensured high plasmon activity and a good scattering signal for the DF measurements.

We also used Au-PNIPAM particles (Figure 7-1b) with cores of 30 nm in diameter, synthesized using a seed mediated route. This enlargement was necessary, due to the fact, that the optical properties of plasmonic NP are dominated by absorption not by scattering for dimensions smaller than 40 nm.[4] The particles with 35.8±8.8 nm in diameter are a compromise between the detection limit of DF spectroscopy and building block dimensions for the creation of screening substrates following the concept of Ref. [15].

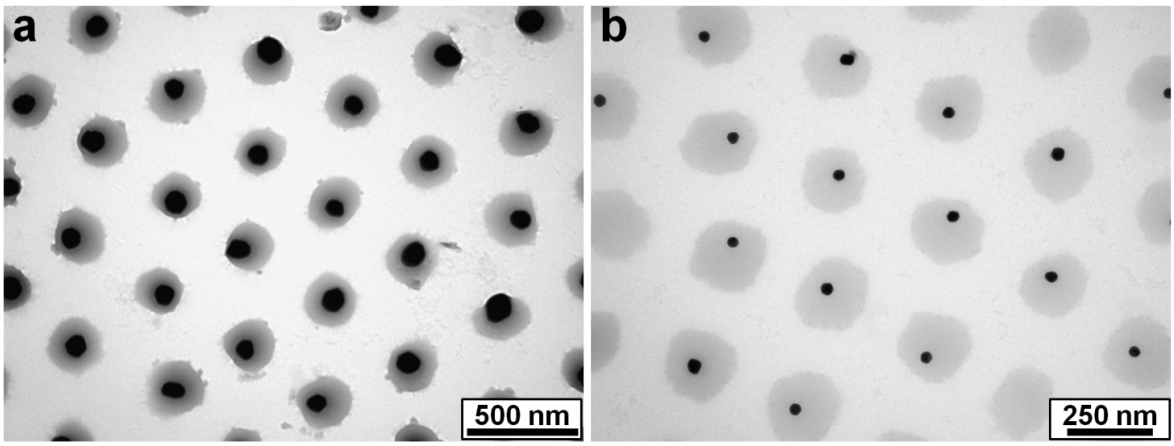

Figure 7-1 TEM characterization of the core/shell particles. (a) shows the dark Ag-PNIPAM cores encapsulated in the grayish PNIPAM shell (D_{core}=103.9±9.5 nm/ D_h=336 nm). In (b) the smaller Au-PNIPAM are shown. The shell is also visible as grey corona around the black cores (D_{core}=35.8±8.8 nm / D_h=211 nm).

For the particle deposition we utilized a template assisted approach, namely replica molding of silicon masters with PDMS. This approach is schematically presented in Figure 7-2a. We used a silicon master with pillars of 350 nm in height and an edge length of 1.0 µm. The spacing between each pillar was 15 µm. The PDMS mixed with the curing agent was poured on the silanized silicon master and immediately degassed in a desiccator. This step is crucial to ensure a high quality replica of the structure. During evacuation, air bubbles are removed and the PDMS is sucked to the pillared structure of the master.

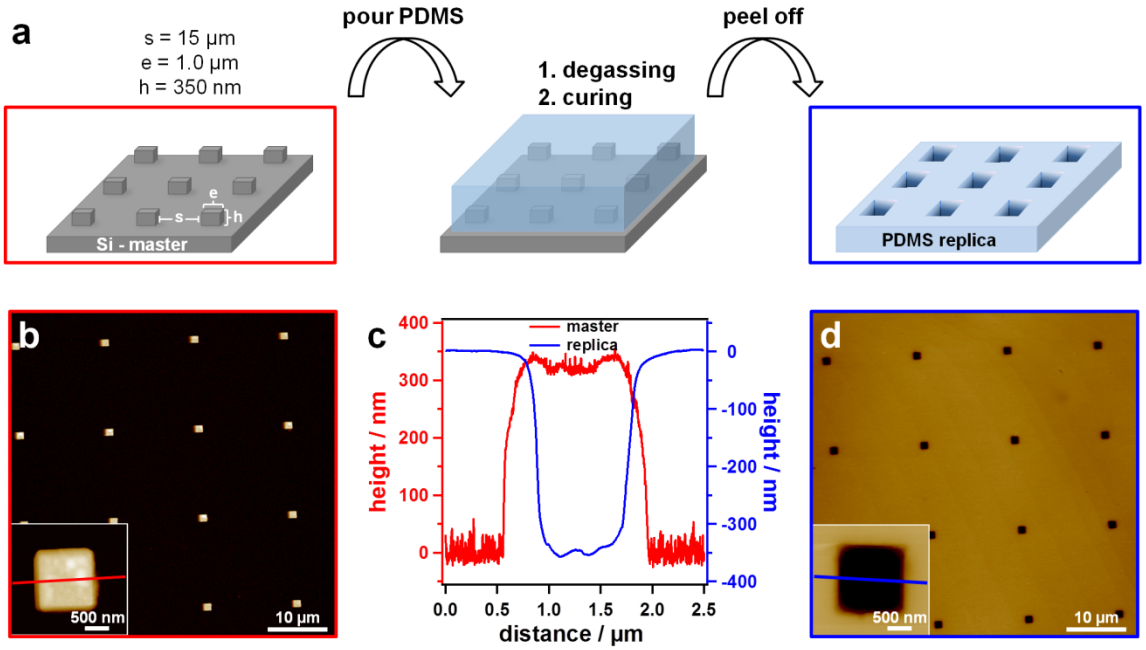

Figure 7-2 depicts the preparation and characterization of the PDMS replica. In scheme (a) is the replica molding presented. Silanized silicon masters with pillars (height =350 nm / edge length = 1.0 µm) and inter pillar spacing of 15 µm were used. The PDMS mixed with the curing agent was poured on top and immediately degassed in a desiccator with subsequent curing in a furnace and peeled off before use. The AFM height images in (b) and (d) show the topography of the master and PDMS. Both surface is even and the edges of the pillars/holes are sharp. The red and blue line of the insets display where the cross sections of (c) were taken. The analysis of this sections shows that the pillars / the grooves are 350 nm height / deep.

The PDMS was cured in contact with the master and peeled off before use. The AFM image of Figure 7-2b shows the surface of the silicon master. The edges of the squared pillars are sharp and the area in between is flat. The red line over the magnified pillar of the inset indicates where the cross section of Figure 7-2c was taken. It reveals that the master was around 350 nm high. The AFM height image of Figure 7-2d depicts the PDMS replica. The quality of the cast is very good, because the edge length of the holes were the same as the ones of the master. Further, the comparison of the cross sections proofed that the holes in the PDMS were as deep as the pillars of the master were high.

The particle deposition into the grooves of the PDMS was done by spin coating. Therefore, the PDMS was hydrophilized with air plasma to guaranty a good wetting of the surface. During spin coating, most of the excessive particles were washed away. To ensure that the areas between the grooves were really particle free a second spin coating step with water or CTAB solution was applied. For the particle transfer to glass the filled PDMS stamp was placed on top of a wetted glass slide and stayed in contact for 2 h to guarantee a complete drying of the water.[14] After the stamp was peeled off, the particles stayed on the glass slide. We investigated the structure and the quality of the substrates

at the different manufacturing steps with reflectance dark field microscopy (see Figure 7-3a to d). The sketches underneath illustrate the DF images. One can see in (a) that the scattering of the pillars was regular with an inter pillar spacing of 15 µm. This was also the case for the PDMS replica in b. The topographical information was inverted from pillars to holes but the spacing and the structure size remained the same. The PDMS with the deposited particles is presented in c. Nearly all particles were deposited into the grooves. Some were left behind on the surface, which was visible as smaller bright spots in between the ordered array, but most of the area is dark, which corresponds with a clean surface. The structured glass is shown in d. The transfer from PDMS to glass worked well, because the scattering pattern was perfectly reproduced with particles.

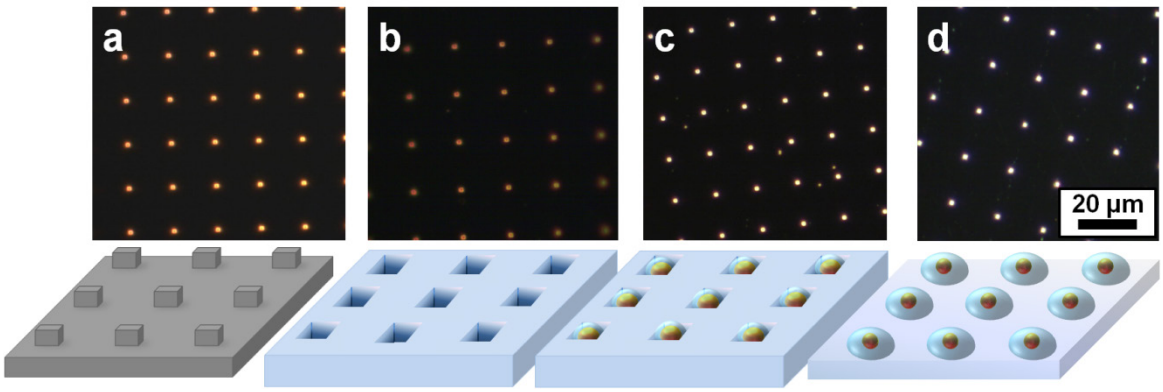

Figure 7-3 presents reflectance dark field images and corresponding sketches. (a) shows the pattern of the silicon master with 1.0 µm edge length, (b) the PDMS replica of the master, (c) the filled PDMS and in d the transferred particles on glass.

This assembly technique worked for the Au-PNIPAM particles (Figure 7-3) as well as for the ones with silver cores. Figure 7-4a presents the AFM height image of such a silver particle array. A transmission DF picture was taken at the same spot and is displayed in Figure 7-4b. The color and the scattering intensity of the DF image correlated very well with the structures determined *via* AMF. The magnification of b1 shows a blue/green spot which belonged to a single particles. The scattering color is as expected for single silver nanoparticles according to literature[18] and was verified with the AFM image of a1. The particle diameter was 290 nm, which lied between the data evaluated *via* TEM and DLS (D_{TEM}=202 nm / D_h=336 nm). The brighter yellowish spot (b2) belonged to an aggregate of two or three particles plus one single particles (a2), which were too close together to be optically resolved in the DF.

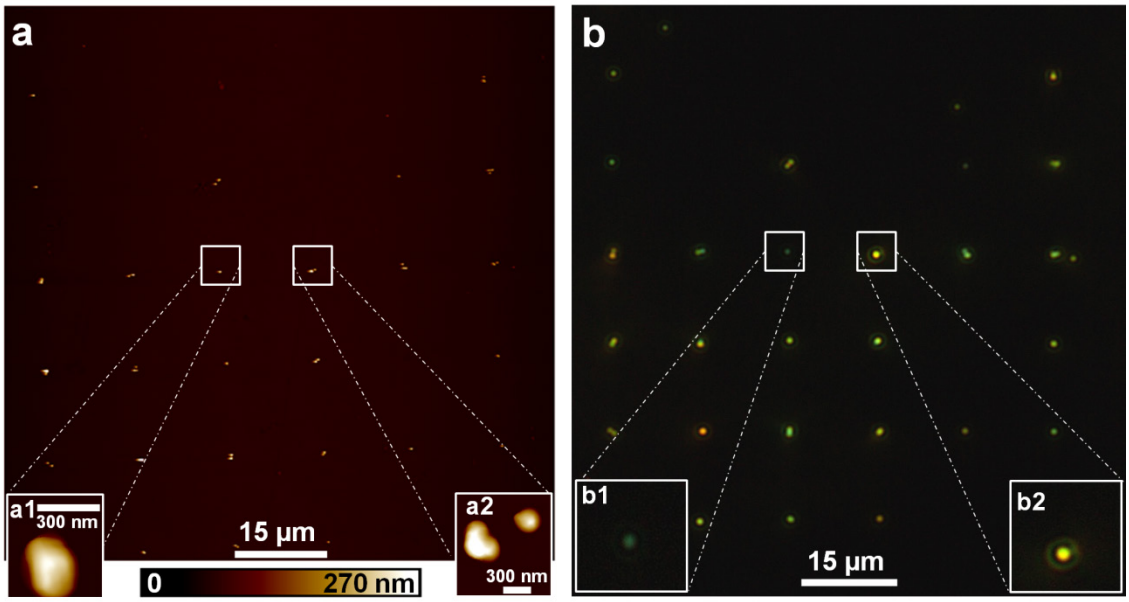

Figure 7-4 Characterization of the same spot of the substrate with AFM and DF. The comparison of the AFM height images of (a) with the dark field image of (b) reveals that a single particle (a1) scatters in blue/green (b1) whereas aggregates (a2) scatter yellow also with higher intensity (b2).

The spectroscopic results are presented in Figure 7-5. The extinction spectra for Ag-PNIPAM are depicted in Figure 7-5a. The spectra for the particles dispersed in water (green line) and a monolayer on glass (red line) were recorded over a macroscopic area with conventional UV-Vis spectroscopy. The LSPR extinction peak for the particles in water lay at 500 nm. This signal was red shifted to 525 nm, if the particles were deposited on glass, due to the refractive index increase from water (1.33) to glass (1.52) where the polymer shell (1.42) is collapsed. The shoulder at lower wavelengths around 420 nm, visible in both measurements, belonged to a quadrupolar mode, because of the large particle dimensions.[19]

The dark field scattering spectra under air are presented in Figure 7-5b. We investigated the single particle of a1/b1 as well as the aggregate of a2/b2. The spectrum of the single blue particle showed its resonance peak at 516 nm. This peak was 9 nm blue/green shifted compared with the extinction measurements from the monolayer. One would expect a similar LSPR position in the extinction spectrum of a 109 nm silver NP compared with its scattering spectrum. The reason for this expectation lay in the large scattering cross section of the particle in respect to its minor absorption cross section. That means that the extinction spectrum obtained by UV-Vis has also to be dominated by the scattering.[4, 19] The discrepancy of 9 nm can be explained by the averaging over a certain core size distribution obtained by UV-Vis measurements.

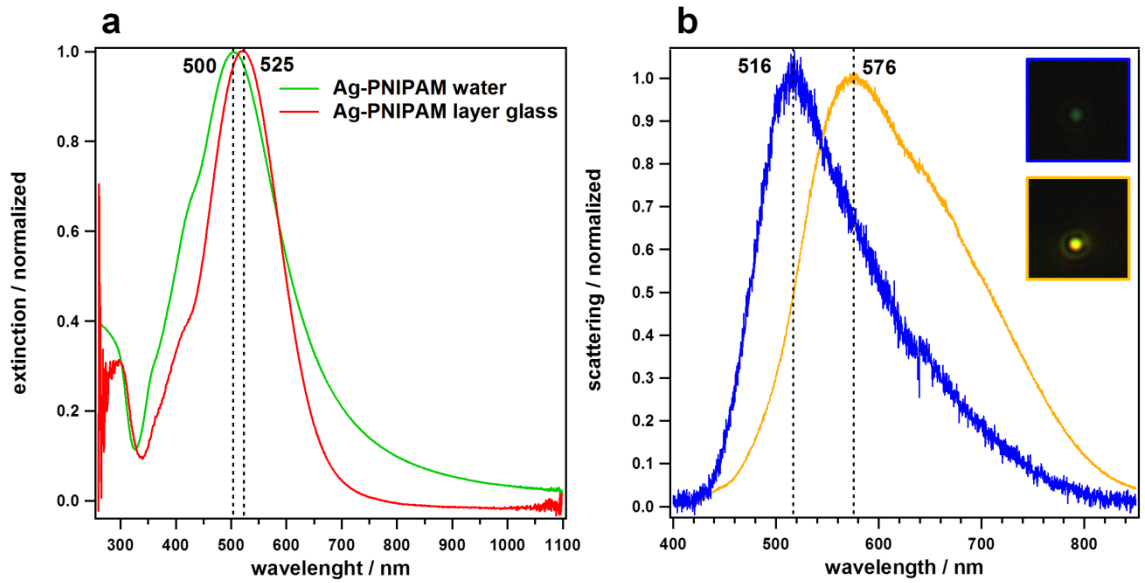

Figure 7-5 Optical characterization of Ag-PNIPAM. The extinction spectra of an Ag-PNIPAM dispersion (green line) and ensembles on glass (green line) are depicted in (a). The spectrum of the particles on glass is red shifted compared to the measurements in water, due to the refractive index increase from water to glass. The scattering spectra recorded with dark field spectroscopy are presented in (b). The blue spectrum corresponds with a single particle presented in the inset framed in blue. The yellow spectrum is 60 nm red shifted and broadened. It corresponds to a cluster of particles that show plasmonic coupling. The corresponding scattering image is shown in the inset framed in yellow.

The scattering peak of the brighter yellow spot is 60 nm red shifted and broadened in respect to the single particle. This shift can be caused by two reasons. On the one hand, cores with other morphologies such as rods, triangles, or platelets can arose during the particle overgrowth. However, one would expect different line shapes with additional peaks due to new modes originated from the anisotropy of the particles.[20, 21] The TEM of Figure 7-1 revealed that the particles are not perfectly round but none of the cores had such an anisotropic shape to explain a plasmon shift of 60 nm. On the other hand plasmon shifts of this magnitude can be caused by inter particle LSPR coupling[22, 23] As shown in the inset a2 of Figure 7-4 the yellow spot belongs to a aggregate which is larger as one single particle. The overall diameter of a dried single particle is 290 nm (AFM) whereas the longest axis of the aggregate is 520 nm. Slightly smaller than two touching particles. This reduced spacing is not unusual for core/shell-PNIPAM particles and was also observed and quantified in Ref. [13]. That means that the surfaces of two Ag cores are separated 156 nm from each other, therefore LSPR coupling is most likely. Because this distance is 104 nm less than 2.5 times the diameter of the particles, which is the threshold for LSPR coupling.[24]

We showed in the previous section that the plasmonic properties of individual PNIPAM core/shell particles can be studied with dark field spectroscopy and the shell is no hindrance for spectra detection. In the next step, we applied the assembly technique to the particle system with the 35 nm gold cores. As mentioned above we wanted to present a technique to fabricate substrates for screening applications on the single particle level. Therefore, the Au-PNIPAM particles were more suitable, because the repertoire of applicable post-modifications is larger for smaller gold cores. For instance, larger size gradients are possible starting just from 35 nm[15] as well as an overgrowth with other metals[25, 27] (without galvanic replacement)[28], or continuous changes in the core morphology.[13, 29]

The transfer process worked also very well for the Au particle system and is presented in Figure 7-6a. The picture shows the particle array which was recorded with the CCD camera of the spectrometer (mirror configuration). The white frame encloses the region of interest, which was placed in the slit of the spectrometer. Every bright spot within the patterning corresponded to particle(s). The intensity profile of Figure 7-6b shows the scattering intensity of the structure. The same scattering intensity per spot was expected for the same particle type. However, the intensity distribution of Figure 7-6b indicates that not just one particle is deposited per spot, but most probably aggregates, which can optically not be resolved and appear as one particle.

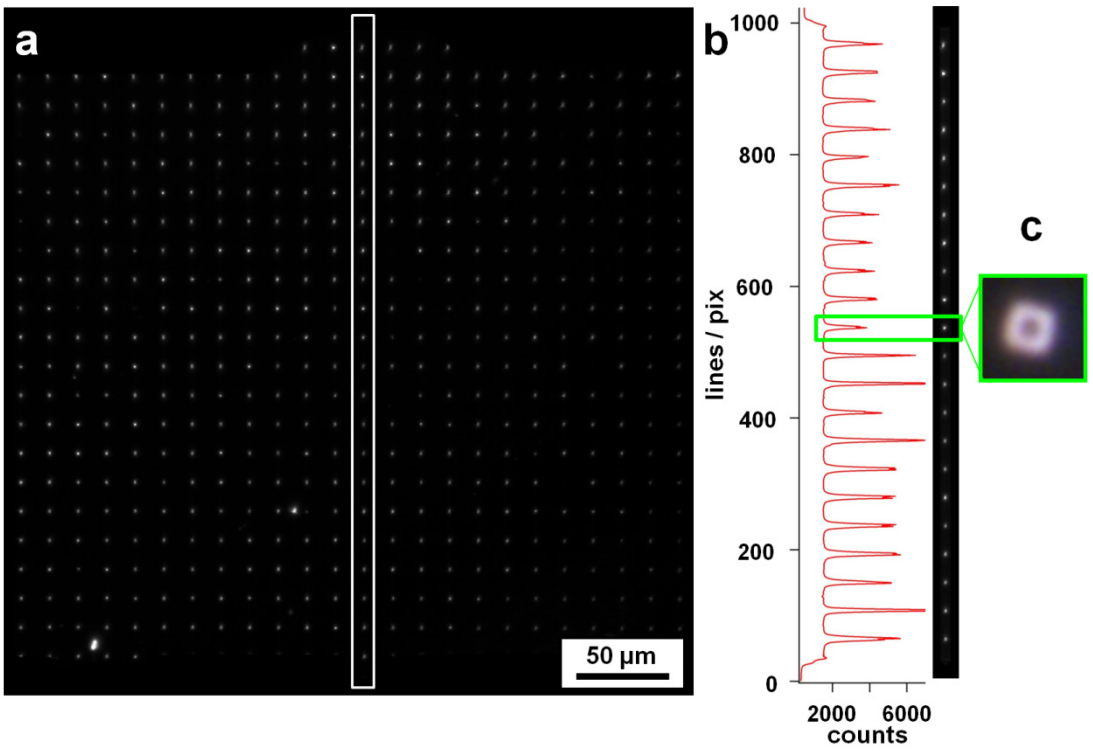

Figure 7-6 Dark field camera image of Au-PNIPAM particles taken with the CCD of the spectrometer used in the image mode. (a) shows the array with the area of interest framed in white. (b) presents the scattering intensity along the array. (c) shows a higher magnification (100x) of one spot taken with a reflectance dark field microscope. This reveals that more than one particle is deposited per square, due to the bright rim with the dark center.

This was verified under larger magnification (100x) using reflectance dark field illumination. Figure 7-6c shows that the particles are arranged in a square like geometry, even for the lowest scattering intensity of the peak framed in green (Figure 7-6b). That means that more than one particle is deposited per hole. This is reasonable, because the squares of the PDMS templates have an edge length of 1000 and a height of 350 nm in contrast to D_h = 211 nm of the particle. Assuming a monolayer of particles within one groove one could deposit 28 touching spheres. This circumstance prohibited a spectral data evaluation. Nevertheless, the authors are confident that this problem can be overcome by adapting the size of the PDMS template to the one of the particles or enlarging the shell of the particles to be in the size regime of the template.

7.4 Conclusion

We presented in this Chapter the fabrication of highly regular arrays of plasmonic-core/PNIPAM-shell particles on glass. We used silver and gold as core materials whereas the silver cores were larger than the gold ones. The particle deposition was

done *via* template assistance of PDMS replica molds with squared holes. The transfer to glass worked for both systems, which was proofed by dark field microscopy and AFM. We investigated the optical properties of the Ag-PNIPAM particles with DF spectroscopy on the single particle level and compared our results with UV-Vis extinction spectroscopy of ensembles. We proved in this way, that the additional scattering contribution of the polymer shell does not hinder the optical DF characterization of the plasmonic cores. The spectroscopic investigation of the Au-system was not possible so far. The reason therefore lies in multiple particle deposition per groove, caused by the miss match of particle diameter and size of the template grooves. Further investigations should concentrate on this issue. The authors are very confident that the adjustment of either the template size or the particle dimensions will solve this miss match. Thereafter the post-modification of the cores has to be applied. This will result in plasmonic screening substrates on the single particle level useful for combinatorial studies or it will help creating plasmonic libraries, which can serve as reference substrates and standards.

References

1. S. Carregal-Romero, J. Pérez-Juste, P. Hervés, L. M. Liz-Marzán and P. Mulvaney, *Langmuir*, 2010, **26**, 1271-1277.
2. C. Novo, A. M. Funston and P. Mulvaney, *Nat Nano*, 2008, **3**, 598-602.
3. C. Sonnichsen, T. Franzl, T. Wilk, G. von Plessen and J. Feldmann, *New Journal of Physics*, 2002, **4**.
4. Y. Sonnefraud, A. Leen Koh, D. W. McComb and S. A. Maier, *Laser & Photonics Reviews*, 2012, **6**, 277-295.
5. M. Hu, C. Novo, A. Funston, H. Wang, H. Staleva, S. Zou, P. Mulvaney, Y. Xia and G. V. Hartland, *Journal of Materials Chemistry*, 2008, **18**, 1949-1960.
6. C. Sönnichsen, Dissertation, Ludwig-Maximilians-University 2001.
7. S. J. Barrow, A. M. Funston, D. E. Gómez, T. J. Davis and P. Mulvaney, *Nano Letters*, 2011, **11**, 4180-4187.
8. N. Pazos-Perez, C. S. Wagner, J. M. Romo-Herrera, L. M. Liz-Marzán, F. J. García de Abajo, A. Wittemann, A. Fery and R. A. Alvarez-Puebla, *Angewandte Chemie International Edition*, 2012, **51**, 12688-12693.
9. R. Glass, M. Moller and J. P. Spatz, *Nanotechnology*, 2003, **14**, 1153-1160.
10. Y. Cui, M. T. Björk, J. A. Liddle, C. Sönnichsen, B. Boussert and A. P. Alivisatos, *Nano Letters*, 2004, **4**, 1093-1098.
11. C. Kuemin, R. Stutz, N. D. Spencer and H. Wolf, *Langmuir*, 2011, **27**, 6305-6310.

12. T. Kraus, L. Malaquin, H. Schmid, W. Riess, N. D. Spencer and H. Wolf, *Nat Nano*, 2007, **2**, 570-576.
13. M. Mueller, M. Tebbe, D. V. Andreeva, M. Karg, R. A. Alvarez Puebla, N. Pazos Perez and A. Fery, *Langmuir*, 2012, **28**, 9168-9173.
14. M. Mueller, M. Karg, A. Fortini, T. Hellweg and A. Fery, *Nanoscale*, 2012, **4**, 2491-2499.
15. M. B. Mueller, C. Kuttner, T. A. F. König, V. V. Tsukruk, S. Förster, M. Karg and A. Fery, *Acs Nano*, 2014, **8**, 9410-9421.
16. M. Karg, S. Jaber, T. Hellweg and P. Mulvaney, *Langmuir*, 2011, **27**, 820-827.
17. B. V. Enustun and J. Turkevich, *Journal of the American Chemical Society*, 1963, **85**, 3317-3328.
18. J. J. Mock, M. Barbic, D. R. Smith, D. A. Schultz and S. Schultz, *The Journal of Chemical Physics*, 2002, **116**, 6755-6759.
19. D. D. Evanoff and G. Chumanov, *ChemPhysChem*, 2005, **6**, 1221-1231.
20. M. J. Mulvihill, X. Y. Ling, J. Henzie and P. Yang, *Journal of the American Chemical Society*, 2010, **132**, 268-274.
21. L. J. Sherry, S.-H. Chang, G. C. Schatz, R. P. Van Duyne, B. J. Wiley and Y. Xia, *Nano Letters*, 2005, **5**, 2034-2038.
22. C. Sonnichsen, B. M. Reinhard, J. Liphardt and A. P. Alivisatos, *Nat Biotech*, 2005, **23**, 741-745.
23. X. Tian, Y. Zhou, S. Thota, S. Zou and J. Zhao, *The Journal of Physical Chemistry C*, 2014, **118**, 13801-13808.
24. S. K. Ghosh and T. Pal, *Chemical Reviews*, 2007, **107**, 4797-4862.
25. A. Steinbruck, O. Stranik, A. Csaki and W. Fritzsche, *Anal. Bioanal. Chem.*, 2011, **401**, 1241-1249.
26. L. Lu, G. Burkey, I. Halaciuga and D. V. Goia, *Journal of Colloid and Interface Science*, 2013, **392**, 90-95.
27. A. Sánchez-Iglesias, M. Grzelczak, B. Rodríguez-González, P. Guardia-Girós, I. Pastoriza-Santos, J. Pérez-Juste, M. Prato and L. M. Liz-Marzán, *ACS Nano*, 2009, **3**, 3184-3190.
28. J. Chen, F. Saeki, B. J. Wiley, H. Cang, M. J. Cobb, Z.-Y. Li, L. Au, H. Zhang, M. B. Kimmey, Li and Y. Xia, *Nano Letters*, 2005, **5**, 473-477.
29. R. Contreras-Caceres, A. Sanchez-Iglesias, M. Karg, I. Pastoriza-Santos, J. Perez-Juste, J. Pacifico, T. Hellweg, A. Fernandez-Barbero and L. M. Liz-Marzan, *Advanced Materials*, 2008, **20**, 1666-+.

8 SUMMARY

The main scope of this thesis was the template assisted surface modification in terms of optical functionalities. The used colloid types for this purpose were hard-core/soft-shell plasmonic nanoparticles. The shell material was always poly(*N*-isopropylacrylamide). As core materials silica, silver and gold were chosen. The advantage of these hybrid particles was on the one hand the encapsulation of core materials with different properties whereas the physical properties of the shell remained the same. This allowed manifold surface modifications for various applications by keeping the assembly conditions similar, due to the same shell chemistry. On the other hand, the shell itself contributed a multitude of benefits. Poly(*N*-isopropylacrylamide) (PNIPAM) is a thermo responsive micro gel. It reacts with shrinking or swelling by exceeding the lower critical solution temperature or cooling down. This stimulus can also be triggered by changing the pH or the ionic strength. Many publications utilize this feature of the PNIPAM. In this work, the attention was drawn to other aspects of the micro gel. The following attributes of PNIPAM were harnessed in this thesis: the role as spacer to control the inter core spacing, the deformability of the soft polymer network and it´s permeability.

For the lithography free surface modification the existing wrinkle-assisted self-assembly technique of confinement assembly was further developed. This evolution was necessary to adapt this lithography free deposition technique to the hard-core/soft-shell particle systems and was presented in Chapter 4.
This so-called spin-release (SR) was suitable for surface structuring with hybrid particles. The particles are pre-assembled into the grooves of polydimethylsiloxane wrinkles using spin coating and placed on top of a wetted glass slide. After drying, the wrinkle was removed and the particles remained on the target surface in a homogeneous anisotropic line pattering.

We investigated first the influence of the wavelength on the achieved structures with particles with silica cores. Using wrinkles with dimensions in the range of the particle diameter led to single particle lines. Wavelengths two times the particle diameter led to zigzag lines. These findings were just dependent on the overall particle diameter and

were independent of the core sizes. In the next step, plasmonic silver-core/PNIPAM-shell particles were used for surface patterning. The shell acted as a spacer between the inorganic cores and prevented them from touching. Anisotropy was not only found in the grid like pattern, due to the wrinkle assembly process, but also on the local structure within the lines. This was caused by the deformability of the soft-shell leading to smaller inter core distances in contrast to assemblies without the confinement of the wrinkles. This was verified by radial distribution functions, which clearly featured the impact of the shell under this deposition conditions. In consequence, a broke symmetry was found between the inorganic cores. The angle between the arranged particles did not follow 60° expected for closed packed layers. Monte Carlo simulations revealed that the observed geometry was an effect of soft shell. Hence, silver colloids show localized surface plasmon resonance (LSPR), UV-Vis extinction spectroscopy was performed on the linear assemblies. This revealed an optical anisotropy as a result of the patterning, due to polarization dependency of the spectra. Even a small inter particle coupling effect could be found revealing a sufficient shell compression. Moreover, the SR is suitable for macroscopic surface structuring, on the cm length scale, which was proven with laser diffraction experiments.

Another aspect of the PNIPAM shell was the stabilization of colloidal suspensions, due to steric and electrostatic forces and introduced in Chapter 5. However, the permeable network allowed post-modification of the cores. This modification was presented by transforming the core of gold-core/PNIPAM-shell particles into a star like shape. This was done by immersing the spherical seed particles in dimethylformamidee containing polyvinylpyrollidon and adding a gold salt solution. The star shape of plasmonic particles has the advantage that hot spots were formed between the spikes. This was useful for surface enhanced Raman spectroscopy (SERS). Therefore, we coated glass slides over large areas with the star shaped gold-core/PNIPAM-shell particles using SR. During the assembly, the shell acted again as a spacer to prevent the touching of the particles that would alter the optical properties of the plasmonic stars drastically. The optical properties of the particles prior modification, after modification and deposited on glass were investigated by UV-Vis extinction spectroscopy. The SR allowed us a homogeneous surface coverage over large areas. It was shown that the stars were good candidates for SERS, because linear arrays of gold stars/PNIPAM shell, particles yielded

in high and homogeneous SERS signals. The substrates were used as chip based SERS sensors to detect the air pollutant pyrene out of the gas phase. The comparison experiments performed with bare gold stars showed that bare gold particles could not be used for gas phase detection. This revealed the importance of the PNIPAM-shell, which trapped the gas molecules close to the gold surface, hence to the hot spots between the spikes, which is essential for this measurement technique.

The works described above dealt with surface modifications with the aid of template assistance. The used building blocks were nanoparticles, which already showed functionality. The properties were adjusted during their synthesis prior to the assembly process. It was shown in this thesis that this order is not necessary. It is also possible to assemble particles first and apply in a second step the particle modification directly on substrate.

We presented such a protocol for the preparation of "plasmonic libraries" in Chapter 6. We assembled Au-core/PNIPAM-shell particles *via* spin coating on microscopy slides and created a continuously size gradient of the Au-cores over the length of the substrate. The functionality of the PNIPAM shell was used to ensure an equidistant core distribution, to avoid LSPR coupling between the gold cores and to bind the particles physically to the substrate. The permeability of the polymer network allowed the post-modification of the cores. The gradient of core sizes was fabricated by dip coating the array in a gold growth solution. This led to a core growth. The overgrowth was controlled with the immersion time by withdrawing the slide continuously. We investigated the growth kinetics for this process quantitatively. We found that the kinetic is diffusion controlled. This allowed us to tune the gradient by the withdrawal speed of the dip coating process, which was set to a decelerating logarithm like ramp. We investigated the optical properties along the gradient by UV-Vis extinction spectroscopy, which showed the expected red shift of the $LSPR_{max}$ position for increased core diameters. Inter particle coupling events were not observed. The core diameter was investigated after calcination of the shell by atomic force microscopy cross section measurements, which matched the scanning electron microscopy analysis. The influence of the surrounding refractive index was also examined by immersing the substrate in water. The $LSPR_{max}$ positions in dried state are red shifted compared to the LSPR positions measured in water, caused by the high refractive index of the collapsed shell.

We compared these results also with predictions from Mie-Theory by calculating the LSPR shifts with the finite-difference-time-domain method.

The last part of this thesis, provided an in Chapter 7 an outlook how the concept of plasmonic gradient materials could be adjusted to the single particle level. Therefore the particles must not deposited in a hexagonal closed packed monolayer but with an inter particle spacing in the micrometer regime - necessary for single particle dark field spectroscopy. Therefore, Ag-PNIPAM colloids were deposited on glass with the help of template assistance. The templates were fabricated by PDMS replica molding of silicon masters. The final pattering of the replicas were holes with a distance of 15 µm in between. The particle deposition was done analog to the spin release process. Large areas have been modified using this assembly technique. It was found that dark field spectroscopy of Ag-PNIPAM core/shell particles was possible and scattering spectra of single particles as well as of coupling aggregates could be recorded. Due to the regular patterning and the large, inter particle spacing the same spot was analyzed by dark field microscopy and compared with AFM height images. Such substrates are the starting point for post-modifications to create chip based screening substrates following the concept of plasmonic gradients, useful for different applications.

Overall, this thesis covered the controlled surface modification with hybrid particles to achieve optical functionality. This particles contained an inorganic, most of the time plasmonic hard-core and a soft micro gel shell. This polymer shell made different surface patterning possible. Further, it was used to tailor the optical properties: either *via* the assembly technique or *via* wet chemical post-modification.

9 ZUSAMMENFASSUNG

Der Schwerpunkt dieser Doktorarbeit lag in der lithographiefreien Oberflächenmodifizierung in Hinblick auf optische Funktionalität. Zu diesem Zweck wurden Hybrid-Nanopartikel verwendet, die aus einem harten Kern und einer weichen Schale aufgebaut waren. Als Kernmaterial wurde sowohl Gold, wie Silber, als auch Silika gewählt. Unabhängig vom Kernmaterial bestand die Schale immer aus Poly(*N*-isopropylacrylamid)-Mikrogel (PNIPAM). Der Vorteil solcher Hybridpartikelsysteme lag zum Einen darin, dass sich physikalische und chemische Funktionalität über die Wahl des eingekapselten Kerns variieren ließen, zum anderen die Wechselwirkung des Partikels mit der Umgebung über die Schale gleich gehalten werden konnten. Des Weiteren birgt PNIPAM selbst eine Fülle von Vorteilen in sich. PNIPAM ist ein thermoresponsives Polymer, welches in Wasser auf Temperaturänderungen mit Schrumpfen oder Quellen reagiert. Diese Responsivität lässt sich auch über pH-, oder Ionenstärkeänderungen auslösen. Diese Eigenschaft wurde in vielen Publikationen untersucht und genutzt. In dieser Arbeit hingegen wurde auf weitere Aspekte des PNIPAMs eigegangen, die gerade in Hybridpartikelsystemen von Nutzen sein können. Besonders folgende Aspekte wurden im Rahmen dieser Doktorarbeit untersucht: Die Rolle als Abstandhalter in Oberflächenbeschichtungen mit plasmonischen Nanopartikeln, die Deformierbarkeit der weichen Schale und deren Permeabilität.

Um Oberflächen lithographiefrei zu modifizieren, wurde die Technik der Templat unterstützen Selbstassemblierung genutzt. Als Template wurden faltenstrukturierte Elastomere gewählt. Die schon existierende Methode des "*confinement assembly*" (eng. Anordnung unter räumlicher Einschränkung) wurde dabei weiterentwickelt. Diese Entwicklung war notwendig, um die Assemblierungsmethode auf die Kern-Schale Systeme zu übertragen.

Es konnte gezeigt werden, dass die weiterentwickelte Variante, der so genannte "*spin-release*" (engl. Kurzfassung, in etwa: Freisetzung nach Rotationsbeschichten) sehr gut geeignet war, um Hybridpartikel auf Oberflächen anzuordnen. Die Kolloide wurden bei diesem Prozess über Rotationsbeschichten in den Falten der

Polydimethylsiloxantemplate (PDMS) abgeschieden und im Anschluss auf einen mit Wasser benetzten Glasträger übertragen. Nach dem Trocken wurde das Faltentemplat abgezogen und die Partikel bleiben in einer linearen anisotropen Gitteranordnung auf dem Zielsubstrat zurück.

Zuerst wurde in Chapter 4 der Einfluss der Templatwellenlänge auf den Anordnungsprozess und die daraus resultierenden Strukturen untersucht. Hierfür wurden Modellpartikel mit Silikakernen mit zwei verschieden Durchmessern verwendet. Es zeigte sich, dass bei Verwendung von Faltenwellenlängen im Bereich der Gesamtpartikeldurchmesser Einzelpartikellinien erzielt werden konnten. Die Verwendung von doppelt so großen Wellenlängen führte zu Zickzack Linien. Welche Strukturen dabei erzielt wurden, war nur vom Gesamtdurchmesser der Partikel abhängig, unterschiedliche Kerngrößen nahmen keinen Einfluss auf die Liniengeometrie. Die Ergebnisse dieser Versuchsreihen zeigten auch, dass PNIPAM als Abstandshalter zwischen den Kernen fungierte und den Direktkontakt der Kerne unterband. Anisotropie wurde nicht nur auf Ebene der Gitterlinien gefunden, sondern auch lokal innerhalb der Partikellinien. Die Verwendung von Partikeln mit weicher deformierbarer Schale, kombiniert mit Anordnung unter räumlicher Einschränkung, verkleinerte den Abstand zum nächsten Nachbarn (Kern) und führte zu einem Symmetriebruch innerhalb der Partikelstruktur. Der Zwischenpartikelwinkel entsprach nicht 60° (typisch für dichte Kugelpackungen), sondern war deutlich größer. Monte Carlo Simulationen bewiesen, dass dieser Effekt eine Auswirkung der deformierbaren Schale ist. Es war notwendig ein weiches Wechselwirkungspotential zu den Berechnungen für harte Kugel hinzuzufügen, um die experimentell gefundenen Strukturen zu erklären. Da Silber Nanopartikel eine "*localized surface plasmon resonance*" (LSPR) (eng. lokalisierte Oberflächen Plasmonen Resonanz) zeigen, wurden UV-Vis Extinktionsspektren von den beschichteten Glasträgern aufgenommen. Es zeigte sich in Polarisationsexperimenten, dass sich die Anisotropie der Anordnung auch auf die optischen Eigenschaften auswirkte. Sogar schwache Plasmonkopplung zwischen den Silberkernen konnte beobachtet werden. Der SR kann für großflächige Oberflächenmodifizierung im Zentimeterbereich genutzt werden, was über Laserdiffraktionsexperimenten bewiesen wurde.

In Chapter 5 wurde die Stabilisatorfunktion der PNIPAM-Schale ausgenutzt, da sie die eingekapselten Kerne in kolloidalen Suspensionen sterisch und elektrostatisch

voneinander abschirmt. Dennoch ermöglichte das permeable Netzwerk eine nachträgliche Veränderung der Kerne. Dies wurde genutzt, um sternförmig Goldkerne in einer PNIPAM Schale zu synthetisieren. Die Synthese geht von PNIPAM Partikel mit einem kleinen sphärischen Goldkern als Saatpartikel aus. Diese wurden in einer Dimethylformamide Polyvinylpyrollidon-Lösung dispergiert. Nachdem eine Goldsalz-Lösung zugegeben wurde, begannen die Kerne in die gewünschte sternförmig Form zu wachsen, erkennbar durch eine Farbumschlag von blass rosa zu einem kräftigen blau. Ein sternförmiges plasmonisches Partikel hat den Vorteil, dass an den Spitzen Felderhöhung auftritt und sich so genannte "*hot spots*" ausbilden. Über SR wurden Glassubstrate mit diesen Partikel beschichtet. Die erzielte Struktur entsprach Gitterlinien, wobei die Schale wieder als Abstandshalter innerhalb der Linien fungierte und die Partikel vor direktem Kontakt schütze. Die optischen Eigenschaften der Partikel vor dem Aufwachsen zu Sternen, die Sterne in Lösung und die Anordnungen wurden mit Hilfe von UV-Vis Extinktionsspektroskopie untersucht. Der SR erlaubte es uns, eine großflächige und homogene Oberflächenbeschichtung zu erzielen. Es wurde zudem gezeigt, dass die Goldstern-PNIPAM Partikel vielversprechende Kandidaten für die "*surface enhanced Raman spectroscopy*" (SERS) (eng. oberflächenverstärkte Raman Spektroskopie) sind. Die linearen Anordnungen zeigten intensive und homogene SERS-Intensitäten. Die Substrate wurden auch als Chip-basierte Sensoren verwendet, um umweltschädliches Pyren aus der Gasphase zu detektieren. Bei Vergleichsexperimente mit reinen Goldsternen ohne Schale, konnte die Anwesenheit von Pyren nicht detektieren werden, da sich die Gasmoleküle nicht in der Nähe der "*hot-spots*" befanden.

Die oben beschriebenen Arbeiten beziehen sich alle auf Oberflächen Modifizierung mittels Templatunterstützung. Die dabei verwendeten kolloidalen Bausteine besitzen schon die gewünschte Funktionalität, da deren Eigenschaften schon vor der eigentlichen Beschichtung eingestellt wurden. Dass dies nicht unbedingt notwendig ist, wurde im Chapter 6 gezeigt. Denn es war möglich Partikel beschichtete Substrate nachträglich zu modifizieren. Wir zeigten, dass ein solches Vorgehen genutzt werden kann, um "plasmonische Bibliotheken" zu erstellen. Dafür wurden sphärischen Au-PNIPAM Partikel über die Länge eines Mikroskopieobjektträgers mittels Rotationsbeschichten abgeschieden. Die Schale wurde auch hier genutzt, um eine äquidistante Partikelabstand zu gewährleisten. Weiterhin konnten die Partikel mit Hilfe der Schale physikalisch auf

dem Glasträger immobilisiert werden. Dies war für den folgenden Modifikationsschritt wichtig, bei dem die Goldkerne mittels autokatalytischer Goldabscheidung vergrößert wurden. Ausreichend Permeabilität der Schale war auch auf Substrat gewährleistet. Das Ziel des Aufwachsens war die Herstellung eines Größengradients der Goldkerne. Dies wurde verwirklich, indem das Substrat komplett in eine Goldwachstumslösung eingetaucht wurde. Das Wachstum wurde über die Immersionszeit kontrolliert, indem das Substrat kontinuierlich herausgezogen wurde. Die Wachstumskinetik wurde quantitativ untersucht und es zeigt sich ein diffusionskontrollierter Prozess. Aufgrund dieser Erkenntnis wurde die Rückzugsgeschwindigkeit des Tauchbeschichters so eigestellt, dass die Rückzugsgeschwindigkeit über die Länge des Objektträgers abnahm, um einen gleichmäßigen Größengradienten zu erreichen. Die optischen Eigenschaften des plasmonsichen Gradienten wurden mittels UV-Vis Extinktionsspektroskopie untersucht und die erwartete Rotverschiebung der $LSPR_{max}$ Positionen für größer werdende Kerne, konnte bestätigt werden. Zwischenpartikuläre plasmonische Kopplung wurde dabei nicht detektiert. Die Kerndurchmesser wurden mit Hilfe von Rasterkraft Mikroskopie bestimmt. Hierbei wurden die Querschnitte der Partikel ausgewertet und mit Rasterelektronenmikroskopieaufnahmen verglichen. Weiterhin wurde der Einfluss des Brechungsindexes untersucht, indem die UV-Vis Messungen nicht nur an Luft sondern auch in Wasser durchgeführt wurden. Es wurde gezeigt, dass die an Luft gemessenen Spektren rot verschoben sind, im Vergleich zu denen, die in Wasser aufgenommenen wurden. Dies wurde durch die Schale verursacht, die an Luft kollabiert vorliegt und einen höheren Brechungsindex als Wasser aufwies. Diese Resultate wurden mit Vorhersagen der Mie-Theorie verglichen. Zudem wurden Spektren über die "Finite-Differenzen-Methode" berechnet und ein gemittelter Brechungsindex individuell für unterschiedliche Kerngrößen erstellt.

Im letzten Teil dieser Doktorarbeit wurden Vorarbeiten präsentiert, die zur Untersuchung plasmonischer Gradienten-Materialien mit Dunkelfeldspektroskopie beitragen werden. Dafür war es notwendig die Abstände zwischen den Kern-Schale Partikeln in den Mikrometerbereich hinein zu vergrößern. Die Abstände zwischen den Kernen einer Hybridpartikelmonolage waren dafür nicht ausreichend. Um dies zu erreichen, wurden die Ag-PNIPAM Kolloide über templatgestütze Selbstassemblierung auf Glasträger abgeschieden. Die Template wurden durch das Abgießen von Silizium-Mastern mit PDMS erzeugt. Die Oberfläche des abgegossenen PDMS enthielt

quadratisch angeordnete Vertiefungen, die 15 µm voneinander entfernt waren. Die Übertragung der Partikel erfolgte analog zur "*spin-release*" Methode. Auf diese Weise konnten große Bereiche mit den Kern-Schale Partikeln strukturiert werden. Es wurden Streuspektren mittels Dunkelfeld Spektroskopie an Ag-PNIPAM Einzelpartikeln und an plasmonisch koppelenden Clustern durchgeführt. Aufgrund des regelmäßigen Musters und den großen Zwischenpartikelabständen konnte dieselbe Stelle sowohl mit dem Dunkelfeld Mikroskop, als auch mit dem Rasterkraftmikroskop untersucht und verglichen werden. Die auf diese Weise beschichteten Glassubstrate sind der Ausgangspunkt für nachfolgende Kernmodifizierungen um Chip-basierte Screening-Substrate herzustellen.

Insgesamt umfasste diese Arbeit also die kontrollierte Oberflächenbeschichtung mit Hybridnanopartikeln in Hinblick auf optische Funktionalität. Diese Partikel bestanden aus einem anorganischem, meist plasmonischem harten Kern und einer weichen Mikrogelschale. Diese Polymerschale machte unterschiedliche Obeflächenstrukturierungen möglich und wurde genutzt um die optischen Eigenschaften einzustellen: entweder über die Art der Beschichtung oder durch nass-chemische Postmodifizierung.

DANKSAGUNG

Mit dieser Danksagung möchte ich meine Doktorarbeit abschließen. Hiermit endet für mich ein ganzer Lebensabschnitt. Ich sehe mit stolz auf die letzten neun Jahre in Bayreuth zurück. Gerade die letzen drei einhalb Jahre, die Zeit meiner Promotion, habe ich als die aufregendsten und spannendsten meines bisherigen Lebens empfunden, wenn auch sicherlich nicht als die Einfachsten. Es gab sehr viele Höhen, und genauso viele Tiefen. Dass ich es bis hier her geschafft habe, verdanke ich sehr vielen Menschen, die mich auf diesem Weg begleitet haben.

An erster Stelle gilt mein Dank meinem Doktorvater Prof. Andreas Fery, der diese Zeit erst ermöglicht hat. Danke Andreas, dass du mir so viel Raum zur Selbstentfaltung und Kreativität gelassen hast. Das habe ich sehr genossen. Verloren oder orientierungslos habe ich mich dabei dennoch nie gefühlt. Du hast es gut verstanden meinen Forscherdrang und Enthusiasmus in die richtigen Bahnen zu lenken, sodass ich das Ziel nie aus den Augen verloren habe. Ich danke dir auch, dass ich so viele Erfahrungen auf nationalen und internationalen Konferenzen sammeln durfte, sei es durch Vorträge oder Poster. Ja sogar transkontinental, bis ans andere Ende der Welt durfte ich dafür reisen! Ich bin definitiv an diesen Erfahrungen sowohl fachlich, als auch persönlich gewachsen. Auch deine Personalführung und dein Umgang mit Konfliktsituationen haben mich sehr beeindruckt und haben mich auf jeden Fall beeinflusst.

Ich danke auch meinen Mentoren Prof. Matthias Schmidt und Prof. Matthias Karg, die mich während meiner Promotionszeit begleitet und beraten haben. Besonders dir Matthias K. gilt mein Dank. Danke, dass du immer ein Ohr für meine Probleme und Ideen hattest. Du hast es sehr gut verstanden, mich immer wieder aufs Neue zu motivieren, wenn es gerade Mal "nicht so lief". Nach einem kurzen Gespräch mit dir, waren die Probleme meist klein und ich hatte wieder Energie um weiter zu machen. Die Zusammenarbeit mit dir war immer geprägt von guter Laune und Tatendrang. Du hast mich auch immer unterstütz und beraten, sei es beim Paper schreiben, Poster gestalten oder Abstract formulieren. Und sind wir einmal ehrlich: Ohne dich und deine super Partikel würde ich wahrscheinlich immer noch im Labor stehen. Die "*awesome inorganic hard-core/soft-PNIPAM shell*"-Partikel leben hoch!

Liebe Sybille! Danke, dass du immer für alle da bist. Ich denke du hast das schon oft gelesen, aber so ist es eben: du bist die beste Lehrstuhl-Mami die man sich nur so wünschen kann. Du hast mich über die Jahre sehr verwöhnt. Dein Leitmotto könnte wirklich sein: "*Unmögliches wird sofort erledigt - Wunder dauern etwas länger!*" (Anonym). Es ist einfach toll, wie du diesen Lehrstuhl zusammen hältst, sei es über Süßigkeiten, dein Lächeln oder dein "mach maaa, is doch gar kein Problem". Dank deiner tollen Lehrstuhl-Deko, wusste ich auch, welche Jahreszeit gerade war und welcher Feiertag als nächstes anstand.

Ich danke all meinen Kooperationspartner und unseren Technikern und wissenschaftlichen Angestellten. Carmen Kunert, Petra Zippelius und Markus Hund, waren immer hilfsbereit und haben diverse Probleme schnell gelöst.
Ich danke auch meinen Praktikanten, Hiwis und Bacheloranten insbesonderm Anja Steiner und Dominike Dietrich. Ihr habt tolle Arbeit geleistet und meine Promotion mit voran getrieben. Danke für euer Engagement!
Liebe PC II vielen Dank für die tolle Zeit: bei Feierabendbierchen oder Spieleabenden im Kaffeezimmer, Kaffepausen auf der Terrasse oder bei zahlreichen Grillevents und natürlich auch wissenschaftlichen Diskussion und Feedback! An dieser Stelle danke ich auch dir Moritz!
Mein Dank gilt auch meinen Bürokollegen, Inna Dewald, Olga Isakin, Anja Steiner, Christoph Hanske und Maximilian Seuß. Danke, dass ihr mich ertragen habt. Ich weiß ich war nicht immer einfach. Ich hatte auf jeden Fall viel Spaß bei euch! Lieber Max und Chris: Danke für die Igorhilfe. Chris und Christoph immer hilfsbereit und immer ein Wissenschaftlicher Tipp im Ärmel: ich habe viel von euch gelernt.

Liebe Maria, Susi, Sophia, Annika, Elli, Philipp, David, Martin und Basti, ich denke ohne euch wäre es hier in Bayreuth sehr trist und langweilig gewesen. Ich werde euch und diese Zeit sehr sehr vermissen. Ihr habt mir Kraft und Halt gegeben. Pavel I will miss the spontanious "sit-ins" at your or my place and your open ear for all my problems.

Liebe Mama, lieber Papa ihr habt immer an mich geglaubt und eure Bewunderung über das was ich mache, hat mich immer wieder angetrieben. Ohne Eure Unterstützung wäre das Ganze nicht möglich gewesen. Auch meinen Großeltern möchte ich Danken, die mir in brenzligen Situationen, ohne zu zögern, ihre Unterstützung haben zukommen lasse.

Mon Cher Samuel. Tu as beaucoup de patience. Tu devrais avoir infiniment de patience avec moi. Merci pour être là pour moi; tout les temps; sans aucun doute. Je sais, ce n'était pas toujours facile avec moi. Bisou mon chum!

(Eidesstattliche) Versicherungen und Erklärungen

(§ 8 S. 2 Nr. 6 PromO)

Hiermit erkläre ich mich damit einverstanden, dass die elektronische Fassung meiner Dissertation unter Wahrung meiner Urheberrechte und des Datenschutzes einer gesonderten Überprüfung hinsichtlich der eigenständigen Anfertigung der Dissertation unterzogen werden kann.

(§ 8 S. 2 Nr. 8 PromO)

Hiermit erkläre ich eidesstattlich, dass ich die Dissertation selbständig verfasst und keine anderen als die von mir angegebenen Quellen und Hilfsmittel benutzt habe.

(§ 8 S. 2 Nr. 9 PromO)

Ich habe die Dissertation nicht bereits zur Erlangung eines akademischen Grades anderweitig eingereicht und habe auch nicht bereits diese oder eine gleichartige Doktorprüfung endgültig nicht bestanden.

(§ 8 S. 2 Nr. 10 PromO)

Hiermit erkläre ich, dass ich keine Hilfe von gewerblichen Promotionsberatern bzw. -vermittlern in Anspruch genommen habe und auch künftig nicht nehmen werde

Bayreuth,

…….

Mareen Beata Müller